Summer 2016

# DFT investigations of hydrogen storage materials

Gang Wang



Department: Physics

# DFT INVESTIGATIONS OF HYDROGEN STORAGE MATERIALS

by

GANG WANG

A DISSERTATION

Presented to the Faculty of the Graduate School of the

MISSOURI UNIVERSITY OF SCIENCE AND TECHNOLOGY

and

UNIVERSITY OF MISSOURI – ST. LOUIS

In Partial Fulfillment of the Requirements for the Degree

DOCTOR OF PHILOSOPHY

in

PHYSICS

2016

Approved by

Eric H. Majzoub, Advisor
Julia E. Medvedeva, Co-Advisor
Yew San Hor
Sonya Bahar
Phillip B. Fraundorf
Stephen M. Holmes

## PUBLICATION DISSERTATION OPTION

Partial content of this dissertation has been prepared in publication format. Paper I has been prepared in publication format for future submission in a scientific journal. Papers II and III have been published in scientific journals. The text format of the papers has been kept as its original publication format. Therefore the citation references in these papers appear at the end of each section and there is exception for figure and captions and they do not follow the general numbering format of this dissertation. The papers are as follows:

Paper I, pages 103-114, "A Study of the Heat and Pressure Induced S105 Phase in $NaAlH_4$", D. Peaslee, G. Wang, D. Zhao, E. G. Sorte, S. Hayes, M. Conradi, B. Bowman, and E. H. Majzoub, *Awaiting Publication,* 2015.

Paper II, pages 115-136, "Effects of NaOH in Solid NaH: Solution/Segregation Phase Transition and Diffusion Acceleration", E. G. Sorte, E. H. Majzoub, T. E. Caleo, B. A. Hammann, G. Wang, D. Zhao, R. C. Bowman Jr. and M. S. Conradi, *J. Phys. Chem. C*, 2013, 117 (45), 23575-23581.

Paper III, pages 137-167, "Density Functional Theory of MH-MOH Solid Solubility (M= alkali) and Experiments in NaH-NaOH", G. Wang, C. L. Carr, D. Zhao, G. Sorte, M. S. Conradi, R. C. Bowman Jr. and E. H. Majzoub, *J. Phys. Chem. C*, 2015, 119 (15), 8062-8069.

## ABSTRACT

Hydrogen serves as a promising new energy source having no pollution and abundant on earth. However the most difficult problem of applying hydrogen is to store it effectively and safely, which is smartly resolved by attempting to keep hydrogen in some metal hydrides to reach a high hydrogen density in a safe way. There are several promising metal hydrides, the thermodynamic and chemical properties of which are to be investigated in this dissertation.

Sodium alanate ($NaAlH_4$) is one of the promising metal hydrides with high hydrogen storage capacity around 7.4 wt. % and relatively low decomposition temperature of around 100 °C with proper catalyst. Sodium hydride is a product of the decomposition of $NaAlH_4$ that may affect the dynamics of $NaAlH_4$. The two materials with oxygen contamination such as $OH^-$ may influence the kinetics of the dehydriding/rehydriding processes. Thus the solid solubility of $OH^-$ groups (NaOH) in $NaAlH_4$ and NaH is studied theoretically by DFT calculations.

Magnesium boride [$Mg(BH_4)_2$] is has higher hydrogen capacity about 14.9 wt. % and the decomposition temparture of around 250 °C. However one flaw restraining its application is that some polyboron compounds like $MgB_{12}H_{12}$ preventing from further release of hydrogen. Adding some transition metals that form magnesium transition metal ternary borohydride [$Mg_aTM_b(BH_4)_c$] may simply the decomposition process to release hydrogen with ternary borides ($Mg_aTM_bB_c$). The search for the probable ternary borides and the corresponding pseudo phase diagrams as well as the decomposition thermodynamics are performed using DFT calculations and GCLP method to present some possible candidates.

# ACKNOWLEDGEMENTS

I would like to thank my advisor Dr. Eric H. Majzoub honestly for not only his dedicated supervision in my research but also his sincere advice in my life during my entire Ph.D. study. His knowledgable teaching in classes, his insightful advice and patient discussion in the research have reformed me and will offer me significant influences in my future.

I would also like to thank all members in Dr. Majouzb's research group ever and present. Working together with them was a fantastic experience in my life. Not only did we make progress together in the study but also they helped me a lot when I encountered problems in my life. I am honored to meet so many nice people from different countries so that I could know different cultures. I hope we could still have cooperations and may help one another in our future life. I hope we can keep our friendship forever.

I am grateful of the Department of Physics and Astronomy for supporting me the whole Ph.D. process financially.

I appreciate Dr. Bruce Wilking for his patient conduction whenever I needed any help.

I would like to thank all faculty and staff members in the Department of Physics and Astronomy for providing me a high quality of professional education and training as well as the administrative kind help.

I thank Dr. William Lemon and Mr. Antony Eckert for their keen work in maintaining reliable and fast computation resources.

I would like to show my respect to my Ph.D. committee members Dr. Eric Majzoub, Dr. Julia E. Medvedeva, Dr. Yew San Hor, Dr. Sonya Bahar, Dr. Phillip B. Fraundorf and Dr. Stephen M. Holmes for their careful proposals in my dissertation work.

At last, I would thank my parents for their support for my study in the United States to be far away from them for these years. Special thanks to my wife for standing me on my back all these years bringing me happiness and encouragement. I also thank my daughter who came in the world to give me a happy complete family.

# TABLE OF CONTENTS

PAPER

# LIST OF FIGURES

Page

PAPER I



PAPER II

PAPER III

# LIST OF TABLES

Page

PAPER I



PAPER II



PAPER III

# SECTION

# 1 INTRODUCTION

## 1.1 ENERGY STORAGE TECHNOLOGY FOR THE FUTURE

The demand for energy is constantly increasing with the development of every country's economy and constant growth of population. More and more families and industries need a great amount of power source. Fossil fuels are not sustainable sources due to the limited total amount [1]. Also, people and governments are willing to reduce the emission of pollution gases all over the world so as to restrain the means of power production. The conflict between the restraint of the power production and the increasing demand of energy gives rise to the fly-high of the cost and impedes the sustainable economy development.

Some clean and powerful energy production methods are being invented such as nuclear fission power that attracts every country's attempt to manufacture it. Some other clean energy production methods like wind power, waterpower, solar power etc. have been widely utilized to satisfy our daily energy consumption. However these new ways of energy generation rely closely on weather, location and/or time. The output of the power is not so stable and adjustable as power from burning fossil fuels. The fluctuation of the instability of the power output may cause drastic disaster. The situation brings about a challenge to convert the fluctuating power to constant output.

Energy storage technology provides a solution to the challenge. The excess energy is stored when no such usage and the stored energy is released when there is a peak demand. The energy storage system can also distribute energy for their different consumption demands and smoothen the voltage in the electricity power network. There are already some state-of-the-art energy storage approaches widely applied to our daily devices, vehicles, apparatuses etc. Here are some examples.

The flywheel system stores electric energy into a rotating mechanical energy. The excessive electric energy accelerates the rotating mass through a motor converting the electric energy into the kinetic energy of the rotating mass. The rotating mass drives an

electric generator to give back electric energy when needed. It is composed of many components as shown in figure 1.1. The power coupling system couples the input electric power into the motor/generator component that accelerates/decelerates the flywheel in the vacuum containment vessel that reduces the friction of the flywheel from air. The shaft under the flywheel supports the whole system on the advanced magnetic bearing that also helps prevent the system from contacting friction of the axis. The low speed flywheel achieves specific energy around 5 Wh/kg and the high-speed flywheel achieves the specific energy of 100 Wh/kg. It only takes minutes to charge and discharge such a battery, which is the main advantage of the flywheel system compared to traditional chemical batteries. The full-cycle lifetimes can go up to $10^5$ to $10^7$ so that the typical lifetime reaches about 20 years. The low friction designs make 90%-ish of energy go back to electricity. However the friction and air drag of the flywheel takes at least 20% of the stored energy loss per hour, which only applies the flywheel system to short-term energy storage in a renewable energy power plant [2] such as solar cell systems, wind turbine systems etc. providing varying power depending on weather and time. The flywheel systems are good to smoothen the fluctuating power output. The flywheel power system is also good to be applied to electric grid that has fluctuation for daily use [3].

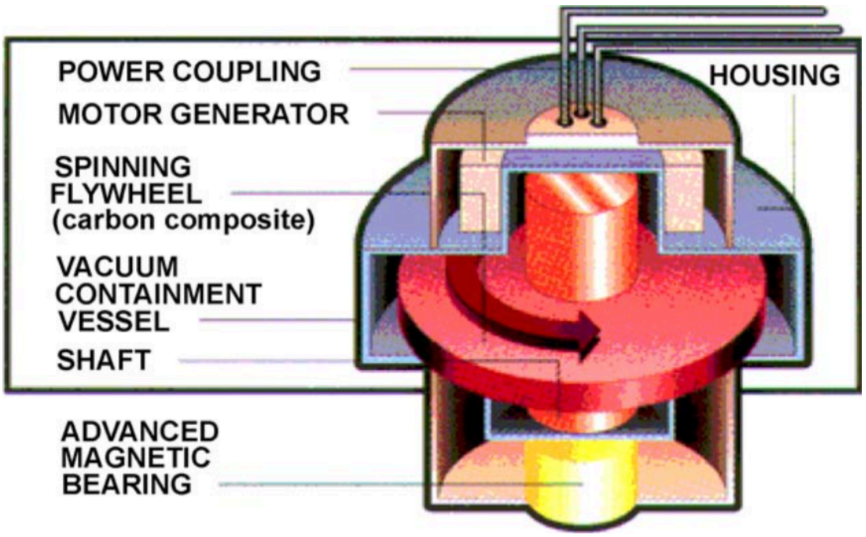


Figure 1.1. Flywheel storage system [3].

Rechargeable batteries convert energy between electricity and chemical energy. A battery contains two electrodes plunged into an electrolyte. The electrons transfer from an electrode through the load/power supply to another electrode as shown in figure 1.2. The discharging process is the electrons leave the anode that is oxidized through the load to the cathode that is reduced in the chemical reaction. The charging process is the opposite. The electrolyte in between the electrodes is the medium to transfer electrons between the electrodes. The three main types of batteries are the lead-acid batteries, the nickel-based batteries and the lithium-based batteries.

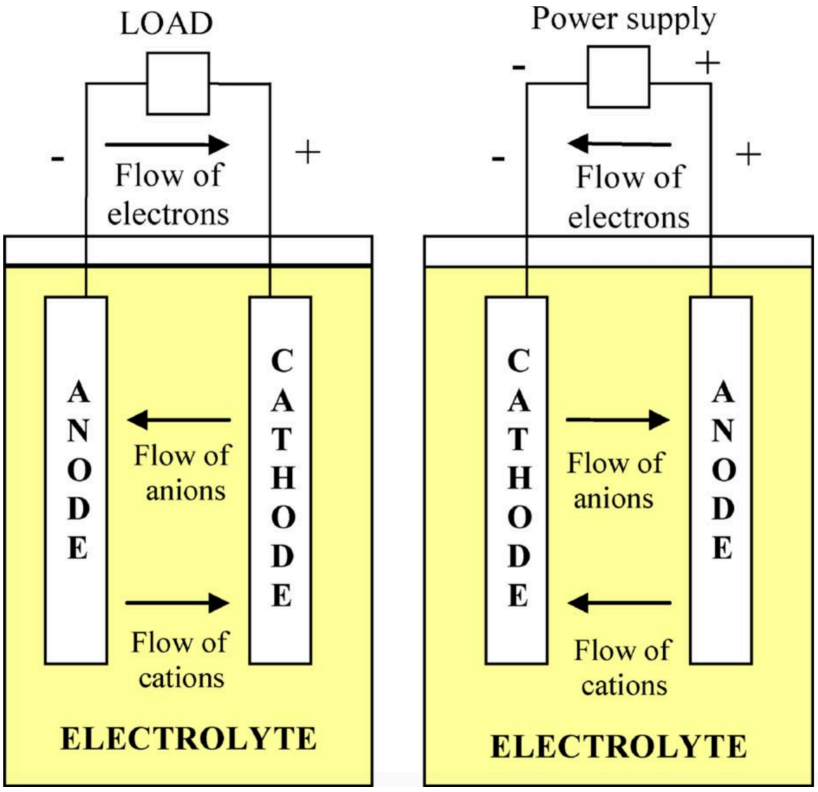


Figure 1.2. Rechargeable battery diagram.

The cathode electrode is $PbO_2$, the anode electrode is Pb and the electrolyte is $H_2SO_4$ for the lead-acid battery. The typical voltage for the lead-acid battery is 2 V. The energy and power densities are 30 Wh/kg and 180 W/kg [4]. The advantages for the lead-acid battery is the high energy efficiency up to 90% similar to the flywheel system, easy to be installed and low level of maintenance and only 2% of energy loss per month.

Therefore the lead-acid battery is ideal for long-term storage rather than the flywheel system suitable for short-term energy storage. The lead-acid battery has 1200-1800 charge/discharge cycles and the typical lifetime is from 5 to 15 years depending the charging/discharging rates.

The nickel-based batteries use $Ni(OH)_2$ as the the cathode and KOH solution as electrolyte, whereas the anode can be NiCd, NiMH or NiZn. The voltage is around 1.2 V and the energy density reached from 50 to 80 Wh/kg with 1500-3000 charging/discharging cycles. The nickel-based batteries can be applied in UPS systems, the cost of which is about 10 times than lead-acid batteries. The energy efficiency is also lower than Lead-acid batteries about 65-80%. The self-discharge rate is also a disadvantage for this type of batteries more than 10% capacity per month.

The lithium-based battery consisting of two types: lithium-ion and lithium polymer batteries is widely used in mobile phones and laptop systems as the most familiar kind of batteries we use today as well as the Tesla cars [5]. Some companies are also developing the technology to apply this kind of batteries into electric vehicles. The voltage for this type of battery is 3.7 V, the energy density is around 80-150 Wh/kg. The energy efficiency is higher than the previous two batteries up to 90-100%. The energy loss is about 5% per month and the lifetime is about 1500 cycles depending on temperature. Another two disadvantages for lithium-ion batteries are the protection circuit needed for charging/discharging processes and the high-cost of the batteries up to $900-$1300/kWh.

Hydrogen storage system is also a promising energy storage method since the burning of hydrogen generates $H_2O$ clean to the atmosphere with the calorific value as high as 3 times that of petrol and 5 times that of coal [7]. The hydrogen storage stores energy in the form of hydrogen in compressed hydrogen or in metal hydrides. Hydrogen can also be contained in nanofibers or as liquid hydrogen.

The steel tanks keep hydrogen under 200-250 bar in pressurized hydrogen technology as shown in figure 1.3. However the ratio of stored hydrogen per unit weight is very low due to the heavy steel material. The advanced material of Al liners and composite carbon fiber stores hydrogen up to 350 bar. Higher pressure for more efficient storage requires stronger materials being under way in investigation [4]. Toyota in Japan

developed a commercial hydrogen-fueled “Mirai” stored hydrogen in the high-pressurized tank in 2014 [8-11].

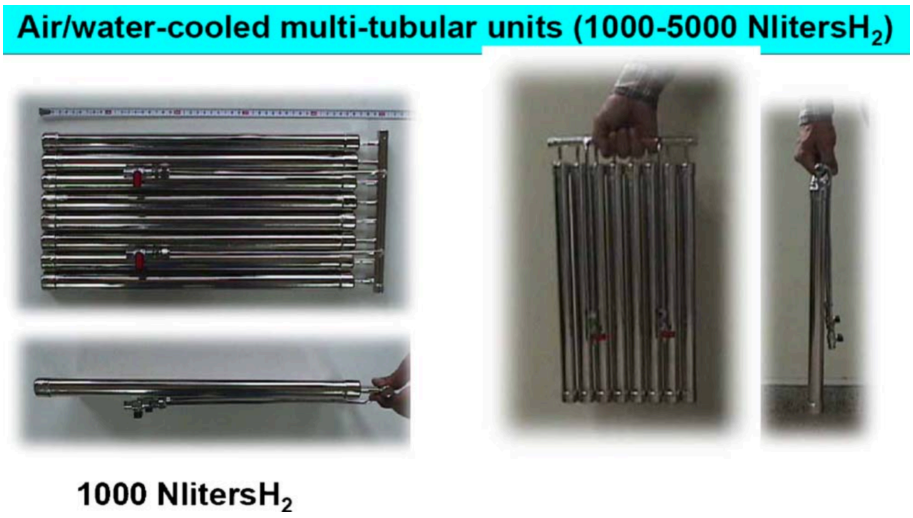


Figure 1.3. Compressed hydrogen tanks [6].

The metal hydrides use certain metal or metal alloys to absorb hydrogen to form a certain metal hydride and then release hydrogen when needed at around atmosphere pressure and room temperature. It is a safe method since the pressure remains low and the ratio of hydrogen is high [12]. Thus hydrogen storage method is going to develop from the high-pressurized tank storage to the safe and cheap hydride storage.

The other approaches are not commonly used. Liquid hydrogen storage is high cost, requires extreme temperatures and extremely inefficient. Carbon nanofibers for hydrogen storage is just beginning.

## 1.2 HYDROGEN AS AN ENERGY CARRIER

Hydrogen, due to its high heat of combustion and clean product ($H_2O$), is promising for future energy carrier [10, 13, 14], which satisfies the clean energy pursuit of people in such a fast developing society that is supported by burning fossil fuels to produce drastic pollution and exhaustion of the fossil fuels needing to be substituted by sustainable and clean new energy sources [1, 7].

**1.2.1 Production and Storage of Hydrogen.** Hydrogen comes from the most abundant liquid in the world – $H_2O$. The ocean occupies three fourths of the surface of the earth providing other numerous free water sources. The electrolysis of water produces hydrogen and oxygen easily. However the efficiency of electrolysis of water is not high enough so that people are focusing on improving the productivity of the decomposition of water. $TiO_2$-based catalysts are used in decomposition of water by sunlight able to decompose fast and efficiently [15-20]. Hydrogen has to be stored in some way to be transportable in vehicles. As mentioned above, the high-pressurized hydrogen can be stored in a steel tank in a gas form or liquefied under extreme low temperatures. But the approaches are too dangerous for daily vehicle use [21]. An applicable storage is to press hydrogen into metal or metal alloys to form some kind of metal hydrides. This way is safe because of the low pressure and stable metal hydrides and the volume percentage is higher than the gas state steel tank method. The complex light metal hydrides have high storage capacity. $NaAlH_4$ and $Mg(BH_4)_2$ are two ideal candidates, which absorb and release hydrogen under relatively low temperatures [22-27]. However it is still slow to hydride and rehydride so that some catalysts can be applied to improve their performance [26,27].

**1.2.2 Complex Metal Hydrides Hydroge Storage Material.** The complex light metal hydrides the complex metal hydrides we refer to are usually in the form of $M(AH_4)_n$, where M is a kind of light metal and A is another light metal or non-metal light element. $AH_4$ group has the charge of -1 where hydrogen has the valence of -1 too. The most promising candidates are $NaAlH_4$ and $Mg(BH_4)_2$ since they have high hydrogen gravimetric and volumetric densities and are common low-cost materials of aluminum, magnesium and boron. Those borohydrides decompositions either occur at different steps at high temperatures or generate quite stable intermediates, which deteriorates the dehydriding/rehydriding performances. Thus some dopants and modifications should be investigated to understand more about the performance of the material.

**1.2.2.1 $Mg(BH_4)_2$.** Magnesium borohydride is a complex light metal borohydride with high hydrogen densities [28-30], which contains 14.8 wt. % equivalent to 112 g/L of $H_2$ making it a very promising candidate for hydrogen storage. The ideal dehydriding of $Mg(BH_4)_2$ decomposes into $MgH_2$, B and $H_2$ at around 350 °C as shown in equation (1.1)

and then $MgH_2$ may decompose into pure metal magnesium and hydrogen as shown in equation (1.2) [31]. However in most cases, $Mg(BH_4)_2$ does not decompose in such a simple pathway but produce some amorphous intermediate $MgB_{12}H_{12}$ and/or $MgB_4$ [31]. Those intermediates prevent further hydrogen release and the rehydriding of such materials.

$$Mg(BH_4)_2 \rightarrow MgH_2 + 2B + 3H_2 \quad (1.1)$$

$$MgH_2 \rightarrow Mg + H_2 \quad (1.2)$$

**1.2.2.2 $NaAlH_4$.** Sodium aluminum hydride has a lower hydrogen percentage of 7.4 wt. % than Mg(BH4)2 but it decomposes at lower temperatures and has no complex intermediates [32]. It takes three steps for NaAlH4 to release hydrogen as shown in equations (1.3), (1.4) and (1.5), the first two of which take place at 150 °C and 200 °C respectively appropriate for commercial use. However the decomposition speed is too slow to be applied to powerful machines, which has been improved by doping catalysts [26, 27] making NaAlH4 an attractive candidate for hydrogen storage applications.

$$3NaAlH_4 \rightarrow Na_3AlH_6 + 2Al + H2 \quad (1.3)$$

$$2Na3AlH6 \rightarrow 6NaH + 2Al + 3H2 \quad (1.4)$$

$$2NaH \rightarrow 2Na + H2 \quad (1.5)$$

## 1.3 OUTLINE OF THE DISSERTATION

This dissertation introduces the density functional study on sodium alanate and the oxygen contamination effects on it, the solubility of alkali metal hydroxides and metal hydrides as well as the investigations of magnesium based transition metal borides and borohydrides.

The density functional theory is introduced in section 2. Its application to phonon calculations of crystals and the probe of crystal structure stability by mode following method are also presented. The simulated annealing method to search probable crystal structures is mentioned in this section. Finally in this section provides the thermodynamic function calculations by phonon results.

The computational method in section 2 is applied to investigating sodium alanate decompositions in section 3. The solid solubility of sodium hydroxide in sodium alanate is also studied to investigate the oxygen contamination effects in this section.

The mixture of alkali metal hydroxides and hydrides is studied theoretically in section 4. The crystal structures of akali metal hydrides and metal hydroxides are also investigated. The phase changes of the solid solutions are simulated using DFT in this section.

The favorable phases of magnesium based transition metal ternary borides are predicted by theoretical simulation of phase diagrams of Mg-TM-B systems in section 5. The corresponding magnesium transition metal borohydries are predicted by Prototype electrostatic ground state approach (PEGS) [33] in this section so as to investigate their direct decompositions.

The experimental and theoretical investigations of sodium aluminum hydride, which is prepared in various environments, especially the S105 phase prepared under heat and pressure, is presented in paper I.

The oxygen cotamination effects in NaH is studied in paper II. NMR, differential scanning calorimetry and X-ray diffraction are applied to the cotaminated samples to show some interesting results. The computational study finally presents some explanations to those results in this paper.

The DFT and experimental study of alkali metal hydrides and hydroxides is presented in paper III, in which the crystal structures of alkalimental hydrides and hydroxides are investigated, their solid solubility is predicted with the critical phase diagrams and the experimental study on NaH-NaOH system is performed to verify the theoretical predictions.

# 2 COMPUTATIONAL METHODS

## 2.1 INTRODUCTION

The first principles approach is to compute the macroscopic and microscopic physical properties of a material using only the atomic geometric configuration in the material. The electronic wave functions of the ground state of the material can be performed purely by quantum mechanism and the other macroscopic properties can be derived from the electronic structures. The calculations refer to the many-body mechanism requiring a powerful computational capability. With the dramatic development of computation devices in the last two decades, the computing capability fulfills the computation using first principles method to achieve required accuracy and precision. The bond length of a hydrogen molecule using the density functional theory (DFT), which was developed from the 1970's having become a dominant approach in current computational material scientific research, is 0.75 Å only about 1% longer than the experimental value of 0.74 Å [34] demonstrating excellent reliability of the approach as an example. With respect to the bulk solid research, all of the thermodynamic properties can be evaluated by phonon mode calculations that are calculated by small displacements of each atom in the crystal. The bulk modulus, for example, reflecting the elastic property of the material can be derived from fitting the total energies at different volumes [35]. The DFT approach succeeding in predicting the properties of so many materials has been the main approach in investigating the hydrogen storage solid crystals worth detailing its basic theory.

## 2.2 DENSITY FUNCTIONAL THEORY

**2.2.1 DFT Beginnings.** Hohenberg-Kohn theorems proved in 1964 [36] are the fundamentals of the density functional theory, which stated that the properties of the ground state of a many-electron system are determined by the electronic density of the system uniquely. The theorem reduces the determination of the properties of a system from 3N degrees of freedom to 3 degrees of freedom for a system with N electrons. The

electronic density is related to the electronic wave functions as:

$$n(r) = 2\sum_i |\psi_i(r)|^2 \quad (2.1)$$

where 2 represents a quantum state can occupy 2 electrons at most with opposite spin states and $\psi_i(r)$ is the wave function of the $i$-th electron at position $r$. This theorem indicates that people need not to explicitly solve electronic wave functions with 3N degrees of freedom but focus on depicting the electronic density in the system with only 3 degrees of freedom, which simplifies the resolution of a many-body electronic system [35]. This reduction also boosts people's ability to investigate complicated many-body systems computationally and predict their physical and chemical properties instead of costly experiments and one can reveal the microscopic quantum mechanism under the physical properties. Then a theorem called Kohn-Sham functional was introduced to substitute the wave functions for electronic density functions in 1965 [37]. The density functional theory was based on such an important equation as shown below.

$$E(\{\psi_i\}) = 2\sum_i -\frac{\hbar^2}{2m}\nabla^2\psi_i d^3r + \int V_{ion}(r)n(r)d^3r + \frac{e^2}{2}\int \frac{n(r)n(r\prime)}{|r-r\prime|} d^3r d^3r' + E_{xc}[n(r)] + E_{ion}(\{R_i\}) \quad (2.2)$$

where the first term is the kinetic energy part of the electronic system, the second term is the interactions between the electrons and the positive ions, the third term is the interactions between electron, the fourth term $E_{xc}$ is called the exchange-correlation functional [35], which includes two parts as the exchange interaction $E_x$ and the correlation part $E_c$. From the above equation is seen that all terms include only the electron density $n(r)$ except the first kinetic energy term consisting of coupling wave functions of electrons, which ruins the attempt to reduce a 3N-many-body system to a 3 degrees of freedom practical computational system. One way of resolving this problem is to substitute the interacting wave functions for the non-interacting independent wave functions as well as modify the external potential $V_{ext}$ to keep the ground state electron density identical to the original interacting one done by Kohn and Sham [38]. Now the effective potential $V_{eff}$ includes not only the external potentials but also the interaction between electrons as shown in equation (2.3).

$$H = \frac{1}{2}\nabla^2 + V_{eff}(r) \quad (2.3)$$

**2.2.2 Exchange-Correlation Functional.** All the terms in the equation (2.2) are explicitly expressed except the exchange-correlation term $E_{xc}$, which including the electron-electron interactions has no explicit known expression such that its form has to be approximated so as to influence the accuracy and precision of the simulation results. The local density approximation (LDA) is one proposal by Kohn-Sham that uses the homogeneous electron gas approximation that has uniform charge density background in the system [38], which well describes the slow-varying electronic environment. In order to describe some sharply varying localized electronic circumstances, the generalized gradient approximation (GGA) is developed form LDA, which takes account into the linear variation part for the electronic density [35]. The exchange-correlation functional is made of the exchange term $E_x$ and the correlation term $E_c$. The exchange term represents the antisymmetric wave functions of electrons manifested as Pauli exclusion principle separating like-spin electrons in space so as to weaken the Coulomb repulsion between electrons, which has an explicit analytical form [38]. The correlation functional contains all other interactions of electrons such as the reduction of the Coulomb repulsion between spatially separating opposite-spin electrons [35], the kinetic energy difference of the non-interacting wave functions etc. The correlation functional has no well-expressed analytical form instead it should be interpolated between the low and high density limits [38].

**2.2.3 DFT in a Periodic Lattice.** Crystals are the most commonly investigated type of materials due to their wide applications in current semiconductor technology such as IC chips that are manufactured based on the silicon crystal, GaAs being used in photovoltaic cells etc. A typical feature of a crystal out of non-crystal materials is its periodicity in the atom arrangement. A crystal made of numerous atoms can be well described by its unit cell by virtue of such repeated periodic arrangement. The potential in a crystal crystal can be formulated as:

$$V(r)=V(r+T_n) \tag{2.4}$$

where $T_n$ represents the period of the potential. The wave function [$\psi_k(r)$] of such a potential with eigenvalue $k$ is in the form of a periodic function $U_k(r)$ [$U_k(r)= U_k(r+T_n)$] multiplied by a phase factor $e^{ikr}$.

$$\psi_k(r)= e^{ikr}U_k(r) \tag{2.5}$$

where the periodic function $U_k(r)$ can be Fourier expanded in the basis of a plane-wave set ($e^{imr}$) as

$$U_k(r) = \sum_G U_G e^{iGr} \tag{2.6}$$

where $U_G$ are the Fourier coefficients. Pull the above expansion into (2.5) gets

$$\psi_k(r) = \sum_G U_G e^{i(G+k)r} \tag{2.7}$$

Now solving the Schrodinger equation for a crystal system with numerous atoms has become solving the Fourier coefficients $U_G$ in equation (2.7) in the basis of a plane wave set analytically. The calculation is converted from an impossible derivative equation to a matrix algebra equation. However the matrix has endless dimensions since there is endless *G*. Therefore there is an upper limit supposed to be set for *G* so that the computation can be performed. The plane wave function represents the kinetic energy ($\frac{\hbar^2 G^2}{2m}$). A cutoff energy can be set up for a maximum *G* for a certain precision for the simulated system.

**2.2.4 Psuedopotentials.** An atom is composed of a nucleus in the center and electrons surrounding the nucleus, which are separated into core electrons and valence electrons. The core electrons are those electrons in the deeper shells of electronic orbits. They are localized in a very small space around the nucleus so that they have very big momentum variation due to the uncertainty principle that $\Delta p \Delta x \sim \hbar$. Besides there is not only one electron crowded around the nucleus, which in turn causes the wave functions of these electrons oscillate sharply due to the orthogonal requirement of the wave functions by Pauli exclusion principle. Thus much energy cutoff of a plane wave set is required to reach a proper convergence for describing the motion of those core electrons that have little variation from element to element. Thus it is unnecessary to consume so much computing resource on those core electrons. The other portion of electrons almost delocalized around the entire crystal due to the core electrons reducing the effective Coulomb attraction of the nucleus to the valence electrons having strong interactions between atoms is called the valence electrons as the main factor that determines the physical and chemical properties of the crystal, which should be accurately concerned and portrayed. Based on the characteristics of the atom, in order to save the computing resources and accelerate the computation, the potentials of the nucleus and core electrons can be combined into an effective potential. The valence electrons perform in the

effective potential. Now it only requires calculating much smoother wave functions for fewer valence electrons at much lower cutoff energy so as to extremely lower the computational demand [35]. The norm-conserving pseudopotential is an implementation of such an idea. A certain core radius is chosen, beyond which there is a smooth wave function without any nodes but within which there are nodes satisfying the orthogonal conditions. The name comes from the total charge of the wave function called norm being preserved so that the bonding properties can be reproduced correctly [39]. The model is able to correctly predict *s*, *p*-elements since those valence electrons are spread over. However for *d*-elements that are partially localized in the core area, the approach needs high cutoff energy to accurately predict the sharp variation of the semi-core *d*-electrons costing expensive computing resource consumption. The ultrasoft pseudopotentials are created to save the computing consumption by Vanderbilt in 1990, which does not require the norm-conservation conditions but add an augmentation charge around the center of the atom to result in a correct wave function scattering [40].

**2.2.5 Projector Augmented Wave Method.** An approach of the GGA pseudopotential is the projector augmented wave (PAW) method that is used in the calculations. The approach overcomes the oscillatory problem of the wave functions near the nucleus by separating the wave functions into the core part that is decomposed into spherical harmonic functions and the interstitial part that is described by plane wave functions. A linear transformation T is used between the real wave functions and the pseudo smoother ones, which is applied to the bonding region and atom by atom.

$$T = 1 + \sum_R \tilde{T}_R \tag{2.8}$$

where $\tilde{T}_R$ is the local transformation operator for atomic site's augmentation region *R*. The real electronic wave functions and the corresponding pseudo wave functions can be decomposed into a partial wave function set as shown below.

$$|\psi\rangle = \sum_n c_n |\phi_n\rangle \tag{2.9}$$

$$|\tilde{\psi}\rangle = \sum_n c_n |\widetilde{\phi_n}\rangle \tag{2.10}$$

The real partial wave set $\phi_n$ and the pseudo partial wave set $\widetilde{\phi_n}$ are coupled with the linear transformation $[|\phi_n\rangle = (1 + \widetilde{T_R})|\widetilde{\phi_n}\rangle]$. Thus by a mathematical trick, the real wave function can be expressed as

$$|\psi\rangle = |\tilde{\psi}\rangle - \sum_n c_n |\widetilde{\phi_n}\rangle + \sum_n c_n |\phi_n\rangle \tag{2.11}$$

The pseudo wave function $\tilde{\psi}$ projected onto the dual of the pseudo partial wave gets the coefficients $c_n = \langle \widetilde{p_n} | \tilde{\psi} \rangle$, in which $\widetilde{p_n}$ is called projector. Therefore the transformation T can be expressed as

$$T = 1 + \sum_n (|\phi_n\rangle - |\widetilde{\phi_n}\rangle)\langle \widetilde{p_n}| \quad (2.12)$$

The transformation operator constitutes partial and the corresponding pseudopartial waves ($\phi_n$ and $\widetilde{\phi_n}$) and the projector operators ($\widetilde{p_n}$). The pseudo wave functions are decomposed in the manner of pseudopartial wave functions and projectors. The real wave functions can be recovered from the decomposition as the coefficients $c_n$ are the same as pseudowave functions [41].

The pseudopartial wave functions ($\phi_n$) can be derived from solving the Schrödinger equation of isolated atoms in the spherical coordinates. The core electrons are approximated with the spherical wave functions since they have little deviation from the isolated single atoms. There is at least such one partial wave at an angular momentum state for each site $R$ [42], which results in a basis set orthogonal to the core states automatically. Then a pseudopartial wave function identical in the bonding region to the real wave function and smooth in the interstitial region is established from the combination of the real electron potential in the core region and a pseudo smooth potential that matches the potential outside the augmentation region without a node, whose corresponding eigenstates are the pseudopartial wave functions.

Then solving the Kohn-Sham equations in such a pseudopotential will find the ground state and its corresponding pseudowave functions. The real wave functions can be transformed from the pseudowave functions using the projectors, which in turn gives the total electronic energy of the system [42]. This method has an advantage that the electron density and potential of an atom do not depend on the chemical environment in the system. This method usually converges much faster than using the norm-conserving pseudopotentials. Compared to ultrasoft pseudopotentials, its calculation is simpler and more efficient [42].

## 2.3 PHONON CALCULATIONS

The ionic vibrations of materials determine a variety of their macroscopic properties such as the optical properties like infrared and Raman diffractions and the thermal properties like the specific heat, sound velocity and chemical favorability that are important for the investigations of hydrogen storage dynamics. The theoretical framework takes advantage of the DFT simulations of the macroscopic properties of materials to save the cost of experimental work and provide an insight into the origin of the properties which provides a prospective way of improving and designing the materials into desired orientation [43]. The Born-Oppenheimer approximation that separates the movements of electrons and ions due to the extremely massive difference of ions from electrons mentions any a slight movement of ions will make electrons find their new ground state instantly, which permits DFT to simulate any near equilibrium state of a material by calculating its near-equilibrium ground state. Phonon calculations are also based on the near-equilibrium simulation of materials.

A global ground state of a material is relaxed by DFT, in which every atom was at each equilibrium position where the total forces on the atom is zero. The phonon vibrational frequencies can be derived by the second derivatives of the total energy with respect to the movements of ions as formulated below.

$$det\left|\frac{1}{\sqrt{M_i M_j}}\frac{\partial^2 E(R)}{\partial R_i \partial R_j} - \omega^2\right| = 0 \tag{2.13}$$

where $M_i$ and $M_j$ are the ion masses, $E(R)$ is the total ground energy with respect to ion positions $R$, $R_i$ and $R_j$ are the positions of ions $i$ and $j$ and $\omega$ is the photon frequency. From the equation above, the phonon calculation is converted to the second derivative calculations of the cell energy with respect to the displacements of ions [43]. There are two major methods calculating the derivatives called direct phonon method (frozen phonon method) and linear response method. The direct phonon method is the approach in the calculations, which is directly calculating the total energy in a slight displacement of each ion using finite elementary method to find out the first and second derivatives of the total energy.

The potential energy $V(R)$ can be expanded in terms of the displacements $U(\ldots; R_i, i; R_j, j; \ldots)$ of atoms as shown below.

$$V(R) = V_0(\dots U(R_i, i) \dots) + \frac{1}{2}\sum \Phi\big(\dots R_i, i; R_j, j \dots\big) U(R_i, i) U(R_j, j) + \cdots \quad (2.14)$$

In the harmonic approximation, the forces acting on an atom *i* with the displacement of $R_i$ for this atom is as follows.

$$F(R_i) = -\frac{\partial V(\dots U(R_i,i) \dots)}{\partial U(R_j,i)} \quad (2.15)$$

Thus the force acting on an atom in terms of the force constants is as follows.

$$F(R_i, i) = -\sum \Phi\big(\dots R_i, i; R_j, j \dots\big) U(R_j, j) \quad (2.16)$$

From the equation above, the force on a particular atom arises from not only the movement of the atom itself but also the displacements of other atoms that affect the potential around the particular atom. The above equation is the key equation for the direct method. The DFT makes a single movement (*U*) of an atom at a time and calculates the corresponding Hellmann-Feynman forces (*F*). Then the linear equation about the force constants can be formulated by the above equation to be solved as a matrix equation.

While the force constants ($\Phi$) are solved, the dynamics matrix can be formulated in terms of the force constants if the phonon of $\Gamma$ point is of the interest. The element of the dynamic matrix is as follows referred to the expansion of the potential.

$$\frac{\partial^2 E(R)}{\partial R_i \partial R_j} = \Phi\big(R_i, i; R_j, j\big) \quad (2.17)$$

Pull the force constants back to equation (2.13) from the fact that the force constants are actually the second derivatives of the total energy. The phonon frequencies can be resolved from finding the eigenvalues of the force constant matrix.

## 2.4 STABILITY OF MATERIALS AND MODE FOLLOWING METHOD

Phonon results reflect the stability of the materials. The stability of a material is very important for the calculations. To investigate a property of a material, the first task is to test its stability, which illustrates the existence of the particular phase. The following are the two examples that show a stable phase and an unstable phase.

**2.4.1 NaH.** NaH is a white byproduct in hydrogen storage materials, which has a face centered cubic structure with a space group of $Fm\bar{3}m$ as shown in figure 2.1 with the golden atoms for Na and white atoms for H. The experimental lattice constant is 4.89

Å [44] with the density about 1.4 g/cm$^3$.

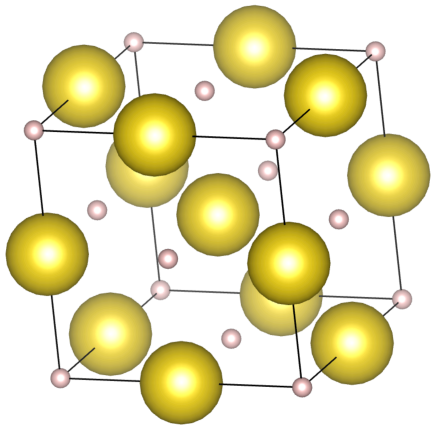

Figure 2.1. Crystal structure of NaH (Na in gold, H in white).

The phonon frequencies are listed in table 2.1 for a variety of units. There are 8 atoms (4 for Na and 4 for H) in the unit cell of NaH so that there are 24 (3x8) degrees of freedom of displacements of the crystal atoms. Therefore there are totally 24 phonon frequency modes, in which the first 21 frequencies are ordinary real phonon vibrations but the last 3 are transitional motions of the crystal with very small values. So the last three are imaginary modes (italic) excluded from the thermal property calculations.

Table 2.1. NaH phonon frequencies at Γ point.

| Mode | Freq. | Mode | Freq. | Mode | Freq. |
|---|---|---|---|---|---|
| 1 | 25.79 | 9 | 20.43 | 17 | 4.15 |
| 2 | 25.79 | 10 | 15.03 | 18 | 4.15 |
| 3 | 25.79 | 11 | 15.03 | 19 | 4.15 |
| 4 | 20.43 | 12 | 15.03 | 20 | 4.15 |
| 5 | 20.43 | 13 | 5.98 | 21 | 4.15 |
| 6 | 20.43 | 14 | 5.98 | 22 | *0.03* |
| 7 | 20.43 | 15 | 5.98 | 23 | *0.03* |
| 8 | 20.43 | 16 | 4.15 | 24 | *0.03* |

In the harmonic approximation, the displacement of an atom in a phonon mode can be expressed as

$$U = Ae^{-i\omega t} \tag{2.18}$$

A real number of phonon frequency indicates the displacement of the atom being a harmonic oscillation. There is always reversed force acting on the atom dragging the atom back to its original position. However while the frequency is an imaginary number like (i|$\omega$|), the displacement becomes $U=Ae^{|\omega|t}$ that implies the atom going far away from its original position indicating the atom having a tendency to leave its original position, which then elucidates that the crystal structure is unstable. Here all the non-transitional modes in the NaH crystal are real numbers indicating that the crystal is stable since all atoms are oscillating around their original position and always have reversed forces dragging the atoms back.

**2.4.2 Monoclinic NaOH.** NaOH has three phases. It is orthorhombic with the space group *Bmmb* from low temperature to 241 °C, monoclinic with the space group $P2_1/m$, and the phase becomes cubic with space group $Fm\bar{3}m$ when the temperature goes over 295 °C. The monoclinic phase can be exemplified to see the unstable phonon results due to its high temperature stability.

Figure 2.2 shows the structure of the crystal. Its optimized lattice constants are $a$ = 3.38 Å, $b$ = 3.36 Å and $c$ = 5.97 Å. The angle between a and b is 106.5°. The OH bond length is 0.97 Å.

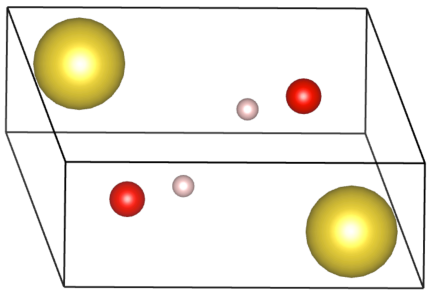

Figure 2.2. Crystal structure of monoclinic NaOH (Na: gold, H in white, O in red).

There are 6 atoms (Na: 2, O: 2 and H: 2) in the conventional cell of monoclinic NaOH crystal. Hence there are totally 18 (3x6) degrees of freedom of the vibrational modes. From the table 2.2 can be seen there are still 15 real modes and the last three are

imaginary modes. In the real modes, the 15$^{th}$ frequency of 0.006 THz is extraordinarily smaller than other ones.

Table 2.2. Monoclinic NaOH phonon frequencies at Γ point (*Frequency in THz).

| Mode | Freq. | Mode | Freq. | Mode | Freq. |
|---|---|---|---|---|---|
| 1 | 113.753 | 7 | 7.965 | 13 | 3.127 |
| 2 | 113.35 | 8 | 7.6 | 14 | 2.808 |
| 3 | 21.729 | 9 | 7.539 | 15 | 0.006 |
| 4 | 16.021 | 10 | 7.413 | 16 | *0.029* |
| 5 | 9.574 | 11 | 6.996 | 17 | *0.041* |
| 6 | 8.952 | 12 | 6.069 | 18 | *5.594* |

Table 2.3 lists the displacements corresponding to the small frequency, where (*x*, *y*, *z*) are the original coordinates of atoms of the crystal and (d*x*, d*y*, d*z*) are the displacements of the atoms, in which (d*x*, d*z*) are 0 except for d*y* that are all similar positive values indicating the whole crystal moves in the y direction. Therefore this is a transitional motion to the y direction implying a fact that this mode is a transitional mode. Thus this mode can be ignored.

Table 2.3. Atomic displacements of mode 15.

| *x* | *y* | *z* | d*x* | d*y* | d*z* |
|---|---|---|---|---|---|
| 0.767 | 0.840 | 2.339 | 0.000 | 0.113 | 0.000 |
| 0.721 | 2.521 | 3.435 | 0.000 | 0.113 | 0.000 |
| 0.799 | 0.840 | 1.367 | 0.000 | 0.446 | 0.000 |
| 0.689 | 2.521 | 4.408 | 0.000 | 0.446 | 0.000 |
| -1.013 | 0.840 | 4.689 | 0.000 | 0.537 | 0.000 |
| 2.501 | 2.521 | 1.085 | 0.000 | 0.537 | 0.000 |

In the last imaginary modes, the first 2 modes are obviously ignorable transitional modes. The last one with about 5.59 THz has a much larger value than the transitional mode.

Table 2.4 lists the displacements of the last imaginary mode, in which ($x$, $y$, $z$) are the original positions of the atoms in the crystal and (d$x$, d$y$, d$z$) are the displacements of the atoms in mode 18. From the table all the atoms move in the y direction. Hydrogen and sodium move to the positive direction of y but oxygen moves to the negative direction of y, which indicates that the mode is a non-transitional mode since all the atoms are moving in different directions. It is actually an optical mode. However this mode is imaginary suggesting that the configuration is unstable since the relaxation usually optimizes the crystal at 0 K. That is reasonable since the monoclinic phase shows up only at very high temperature and it will be transformed into the orthorhombic phase at low temperatures. This example shows the phonon results examine the stability of a particular phase.

Table 2.4. Atomic displacements of mode 18.

| | $x$ | $y$ | $z$ | d$x$ | d$y$ | d$z$ |
|---|---|---|---|---|---|---|
| H | 0.767 | 0.840 | 2.339 | 0.000 | 0.641 | 0.000 |
| H | 0.721 | 2.521 | 3.435 | 0.000 | 0.641 | 0.000 |
| O | 0.799 | 0.840 | 1.367 | 0.000 | -0.282 | 0.000 |
| O | 0.689 | 2.521 | 4.408 | 0.000 | -0.282 | 0.000 |
| Na | -1.013 | 0.840 | 4.689 | 0.000 | 0.100 | 0.000 |
| Na | 2.501 | 2.521 | 1.085 | 0.000 | 0.100 | 0.000 |

**2.4.3 Mode Following Method.** While a given crystal needs to be investigated, the first step is to relax the crystal to find its ground state. After the cell is relaxed, it is to investigate its stability to assure that the relaxed state is its ground state. But sometimes the phonon frequencies show several non-transitional imaginary modes indicating the given crystal is unstable that the given crystal is not the global ground state of the certain material.

Figure 2.3 plots a metastable state that DFT converges shown as the yellow circle where the configuration reaches a local minimum so that certain atoms are positioned in the coordinates (X, Y, Z). While a phonon calculation is performed with a certain displacement (dx, dy, dz) added to the original positions (X, Y, Z) so that the displaced

configuration becomes (X+dx, Y+dy, Z+dz), the configuration moves at a slope and tends to fall to its global minimum as shown with a solid red circle in figure 2.3 where it is not a stable position so that some imaginary modes appear giving the atoms tend to fly away from their original positions. The mode following method is generated from the scheme explained above that it adds the biggest imaginary phonon motion (dx, dy, dz) to the original atom positions (X, Y, Z) to form new atom positions (X+dx, Y+dy, Z+dz) as shown in table 2.5 for NaOH as an example. Then DFT optimizes the new configuration to drive the crystal to its global minimum. Table 2.6 shows the phonon modes for mode-followed NaOH indicating that the mode-followed optimized structure is stable. This method can be applied to the exemplified monoclinic NaOH to find a stable phase close to the metastable configuration.

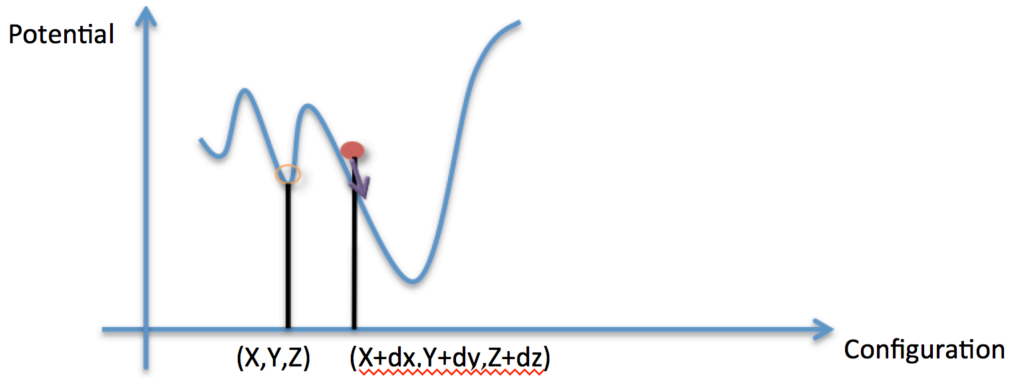


Figure 2.3. Potential surface scheme of an unstable crystal.

The columns (X+dx, Y+dy, Z+dz) are the sums of the original positions of atoms (X, Y, Z) and their displacements (dx, dy, dz). The new configuration brings the crystal in a slope of the potential surface, which can be relaxed by DFT to reach its global minimum. The symmetry of the relaxed mode-followed structure is broken. The lattice constants are $a$ = 3.44 Å, $b$ = 3.33 Å and $c$ = 5.60 Å. The angle between $a$ and $b$ is about 108°. The stability of the new configuration can be seen from the phonon frequency results as follows.

Table 2.5. Adding atomic displacements of mode 18 to atomic coordinates in the monoclinic NaOH crsytal.

| | X | Y | Z | dx | dy | dz | X+dx | Y+dy | Z+dz |
|---|---|---|---|---|---|---|---|---|---|
| H | 0.767 | 0.840 | 2.339 | 0.000 | 0.641 | 0.000 | 0.767 | 1.481 | 2.339 |
| H | 0.721 | 2.521 | 3.435 | 0.000 | 0.641 | 0.000 | 0.767 | 1.481 | 2.339 |
| O | 0.799 | 0.840 | 1.367 | 0.000 | -0.282 | 0.000 | 0.799 | 0.558 | 1.367 |
| O | 0.689 | 2.521 | 4.408 | 0.000 | -0.282 | 0.000 | 0.689 | 2.238 | 4.408 |
| Na | -1.013 | 0.840 | 4.689 | 0.000 | 0.100 | 0.000 | -1.013 | 0.940 | 4.689 |
| Na | 2.501 | 2.521 | 1.085 | 0.000 | 0.100 | 0.000 | 2.501 | 2.621 | 1.085 |

Table 2.6. Mode-followed configuration of $P2_1/m$ NaOH phonon frequencies at Γ point.

| Mode | Frequency [THz] | Mode | Frequency [THz] |
|---|---|---|---|
| 1 | 107.823 | 10 | 7.400 |
| 2 | 106.390 | 11 | 6.993 |
| 3 | 28.835 | 12 | 6.228 |
| 4 | 23.314 | 13 | 6.219 |
| 5 | 17.386 | 14 | 4.254 |
| 6 | 16.513 | 15 | 3.311 |
| 7 | 8.676 | 16 | *0.017* |
| 8 | 7.993 | 17 | *0.067* |
| 9 | 7.495 | 18 | *0.076* |

All the non-transitional phonon frequencies are real numbers except the last 3 transitional phonon frequencies, which indicates that every atom is at its stable position so it is a stable structure. From the above-mentioned example illustrates that the mode following method is an effective way of finding a stable structure near an unstable crystal but it may break the original crystal symmetry sometimes. This method is drastically useful for the investigation of some solid solutions, the structures of which are unknown and created from some known precursor materials.

## 2.5 SIMULATED ANNEALING METHOD

The solid solution is the main topic of discussion in this dissertation. The prediction of the favorability and structure of a particular solid solution is the premises of further discussion of its thermal and chemical properties and applying them to further hydrogen storage reactions. A particular solid solution is usually generated from the substitution of certain number of the atoms of a particular element into an already known structure of solvent crystal supercell such as 2 fluorine atoms are substituted in the conventional cell of cubic NaH to simulate 50%-NaF-NaH solid solution as shown in figure 2.4 below.

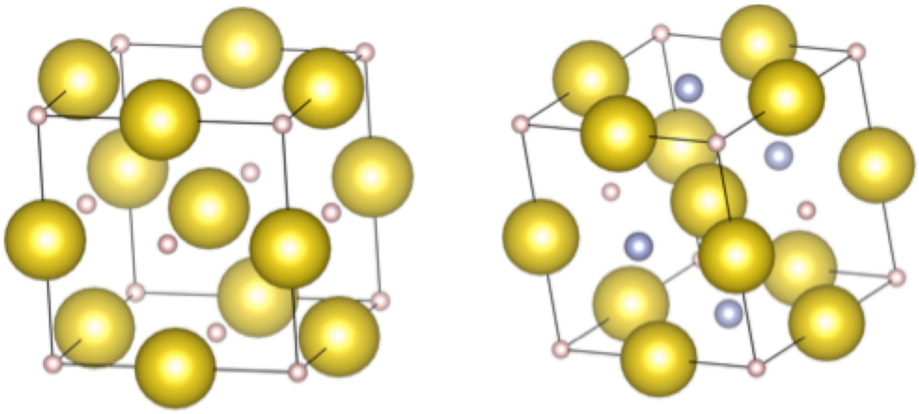

(a) (b)

Figure 2.4. NaH crystal structure (a) and 2 fluorine atoms substituted for F to form $NaH_{0.5}F_{0.5}$ (b) (Na in gold, H in white, F in grey).

It is a good way of building the solid solution crystal but there is another factor worth considering in the substitution that which hydrogen atoms should be replaced with by the fluorine atoms. While two adjacent hydrogen atoms are substituted for fluorine atoms, the repulsive forces between the fluorine atoms should be too big, resulting in high total energy, so as to foster the adjacent fluorine atoms to diffuse far away so that fluorine atoms tend to diffuse uniformly spread over around the crystal, which has relatively lower total energy. Therefore a good solid solution should be reached by distributing the solute atoms in proper positions so that the solid solution has the lowest energy. An energy function should be used to check the reduction of energy for different

configurations. The energy of the Coulomb interactions between ions in the crystal can be used as the energy function as being expressed in equation (2.19) since the Coulomb interactions dominate the interaction in ionic crystals. Then an algorithm should be used to search the minimum of the energy function in the configuration space of the solid solution to find the best configuration for the solid solution. It is impossible to traverse in the configuration space due to the immense number of configurations in the configuration space. The simulated annealing method is the best attempt to reach the global minimum in the search of the configuration space.

$$E = \sum_{i \neq j} \frac{e_i e_j}{r_{ij}} \tag{2.19}$$

where $e_i$ and $e_j$ are the reference charges of elements $i$ and $j$.

Simulated annealing algorithm is such an algorithm that simulates the annealing process to find the global minimum of a system in the configuration space. The very first step of the algorithm is to pick up a configuration randomly in the configuration space and calculate the energy function as $E_0$. Then pick an atom, move this atom randomly to some new possible position and calculate the current energy of the system as $E_1$. Compare the energy $E_0$ and $E_1$ as $\Delta E=E_1-E_0$. The new configuration is accepted when $\Delta E<0$ that the new configuration has lower system energy. However while $\Delta E>0$, there is a probability of accepting the move as $e^{-\Delta E/T}$, where $T$ is the reference temperature that is set as a high value of $T_i$ initially, which simulates the system at a high temperature that all atoms almost freely move in the system to have a high probability of accepting the new configuration. A random number $r$ is picked between 0 and 1. The new configuration is accepted when $r< e^{-\Delta E/T}$ otherwise rejected. After a large number of moves are running, the reference temperature should be reduced a little bit to simulate the cooling process of annealing. The reference temperature is reduced exponentially for every step as $T_n = T_i e^{-[(1/N)ln(T_i/T_f)]n}$, where $N$ is the desired total number of cooling steps, $T_f$ is the final cooled down temperature very close to 0 and $n$ is the current number of step. It becomes harder to accept a higher energy move while the reference temperature goes low, which simulates the atoms are localized at a low temperature solid state. This process of accepting higher energy configuration prevents the search from being trapped in the local minimum. The global minimum may be achieved after a very large number of runs during the cooling system. The pseudocode of the algorithm is listed below.

```
// Simulated annealing pseudocode
Ti=[initial high temperature]
Tf=[final low temperature close to 0]
T=Ti
E_old=[energy of initial configuration]
n=0;
do
{
    m=0;
    do
    {
      [make a move of the configuration]
      E_new=[energy of the new configuration]
      if(E_new<=E_old)  [accept the move]
      else (E_new>E_old)
          {
            r=[pick up a random number between 0 and 1]
            if(r<=exp(-(E_new-E_old)/T)) [accept the move]
            else [reject the move]
            E_old=E_new
            ++m
          }
    } while(m<=[a very large integer])
    ++n;
    T=Ti*exp(-(1/N)*ln(Ti/Tf)*n)
} while (T>=Ti)
```

## 2.6 THERMODYNAMIC FUNCTIONS FROM PHONON RESULTS

All thermodynamic functions can be derived from the phonon results, in which interest us are Gibbs free energy and enthalpy of a chemical reaction. The Gibbs free

energy is used to examine the proceeding of a chemical reaction that a chemical procedure tends to minimize the Gibbs free energy. The enthalpy of a chemical reaction is an important characteristic of such chemical reaction that describes the heat the certain chemical reaction absorbs or releases at a constant pressure, a relatively high value of which represents the reaction is difficult to proceed that requires too much energy. Whereas the enthalpy being too low implies the product may be too unstable. A negative value of the enthalpy represents that the reaction is an exothermic reaction that may explode in some way. The following subsections introduce how some thermodynamic functions and enthalpy change of a reaction are derived from phonon frequencies.

**2.6.1 Thermodynamic Functions.** The Gibbs free energy is defined as a thermodynamic potential that measures the most obtainable work in a thermodynamic system at a constant temperature and pressure (isothermal, isobaric). The Gibbs free energy ($G$) of a system is defined as follows.

$$G = U - TS + pV \tag{2.20}$$

where $U$ is the internal energy of the system, $T$ is the temperature, $S$ is the entropy, $p$ is the pressure and $V$ is the volume of the system. The definition can also be expressed as:

$$G = F + pV \tag{2.21}$$

Where $F$ is the Helmholtz free energy that is a thermodynamic potential that measures the most extractable work in a closed thermodynamic system at a constant temperature.

The partition function that describes the thermal properties of a system is the fundamental function for a thermal system. All other thermodynamic functions are derived from the partition function. The partition function of a solid system in the harmonic approximation is defined as follows.

$$lnZ = -\beta\left(E_0 + \sum_r \frac{1}{2}\hbar\omega_r\right) - \sum_r \ln\left(1 - e^{-\beta\hbar\omega_r}\right) \tag{2.22}$$

where $Z$ is the partition function, $\beta = \frac{1}{k_B T}$ in which $k_B$ is Boltzmann's constant and T is the absolute temperature, $E_0$ is the electronic total energy of the solid system, $\sum_r \frac{1}{2}\hbar\omega_r$ is the zero point energy (ZPE) in which $\omega_r$ is the phonon mode in the solid system and the last term is the temperature related vibrational term.

The total internal energy is derived from the partition function and can be expressed in terms of phonon frequencies in the harmonic approximation from equation

(2.6.3) as follows.

$$U = -\frac{\partial lnZ}{\partial \beta} = E_0 + \sum_r \frac{1}{2}\hbar\omega_r + \sum_r \frac{\hbar\omega_r e^{-\beta\hbar\omega_r}}{1-e^{-\beta\hbar\omega_r}} \quad (2.23)$$

From the equation (2.6.4) can be seen that the internal energy consists of the electronic energy $E_0$ that is the energy from the interaction of nuclear ions and electrons as well as the kinetic energy of electrons, the zero point energy by ion vibrations showed as the second term and the temperature related vibrational part as the third term.

Gibbs free energy is composed of Helmholtz free energy and $pV$ part that is negligible by virtue of the fact that the change of the volume is ignorable in the chemical process of a solid state system. Therefore the Gibbs free energy is about equal to the Helmholtz free energy that $G$=$F$. The free energy can be expressed in terms of the partition function as follows.

$$G = F = -k_B T lnZ = E_0 + \sum_r \frac{1}{2}\hbar\omega_r + k_B T \sum_r \ln\left(1 - e^{-\beta\hbar\omega_r}\right) \quad (2.24)$$

The free energy consists of the electronic energy, the zero point energy and temperature related vibrational energy.

Entropy is a measure of disorder in a thermodynamic system, which is defined in ways of the number of all possible microstates. Entropy will always increase in a spontaneous process for an isolated system according to the second law of thermodynamics. A system will develop to reach an equilibrium state where the entropy reaches the maximum in the system and the system will never develop any longer. It is a very important measure of a thermodynamic system to see the proceeding of the development of the system. Entropy of a solid-state system is expressed as follows.

$$S = k_B(lnZ + \beta U) = \frac{1}{T}\sum_r \frac{\hbar\omega_r e^{-\beta\hbar\omega_r}}{1-e^{-\beta\hbar\omega_r}} - k_B \sum_r \ln\left(1 - e^{-\beta\hbar\omega_r}\right) \quad (2.25)$$

Those thermodynamic functions mentioned above are some important functions that may be used in the study of the properties and chemical processes of hydrogen storage materials, all of which can be derived from the phonon calculations. Those equations allow us to investigate the thermal properties of a solid system from first-principles phonon calculations.

**2.6.2 Chemical Reaction Prediction and Its Reaction Enthalpy.** A chemical reaction proceeds in the direction of decreasing the Gibbs free energy of the system. A system reaches its equilibrium when the Gibbs free energy of the system attains its

minimum in the mathematical form as:

$$\Delta G = G_{products} - G_{reactants} \leq 0 \tag{2.26}$$

The equation above provides a way of predicting the chemical reaction proceeding that a particular chemical reaction is favorable when the free energy of the products is less than or equal to the free energy of the reactants expressed as follows.

$$G_{products} \leq G_{reactants} \tag{2.27}$$

The phase diagram that shows the possible phases in a set of all prospective phase candidates can be predicted by minimizing the free energy in the phase set. The crystals of the set of chemical candidates are relaxed by DFT and the phonon frequencies of each of them are performed on the relaxed crystals. Then the free energy of each is calculated using equation (2.24) at a particular temperature in the phase diagram. The Grand Canonical Linear Programming (GCLP) method is used to minimize the total free energy in the competing candidates at the temperature. The possible phases and their ratios with minimum free energy are picked out in the competition of all possible phases in the candidate set at the temperature. This method is used specifically in examining the favorability of a solid solution in the studies. To examine the favorability of a solid solution ($A_{1-x}B_x$) that is mixed from two separate phases A and B can evaluate the change of the free energy at a particular temperature as follows.

$$\Delta G = G(A_{1-x}B_x) - [(1-x)G(A) + xG(B)] \tag{2.28}$$

The solid solution is favorable when $\Delta G < 0$ otherwise A and B tend to keep phase separate.

A chemical reaction takes place at the phase boundary in the phase diagram where the reactant phases have the same total free energy as that of the product phases.

$$G_{products} = G_{reactants} \tag{2.29}$$

The equation above predicts the temperature that a particular chemical reaction takes place. It also specifies the enthalpy of the chemical reaction. The free energy is defined in terms of enthalpy as follows.

$$G = H - TS \tag{2.30}$$

In the condition that the chemical reaction takes place where equation (2.29) is satisfied gives the following equation.

$$H_{\text{products}} - T_0 S_{\text{products}} = H_{\text{reactants}} - T_0 S_{\text{reactants}} \tag{2.31}$$

where $T_0$ is the temperature of the chemical reaction taking place. Therefore the change of the enthalpy $\Delta H$ is as

$$\Delta H = H_{\text{products}} - H_{\text{reactants}} = T_0(S_{\text{products}} - S_{\text{reactants}}) = T_0 \Delta S \tag{2.32}$$

From the equation above shows that the enthalpy of a chemical reaction is equal to the product of the temperature at which the chemical reaction takes place and the change of the entropy in the chemical reaction. The entropy can be calculated from equation (2.25). Hence the enthalpy of a chemical reaction can be predicted from DFT phonon calculations.

Those equations and theory are the fundamentals for the study of the properties of the hydrides in the applications of hydrogen storage technology.

# 3 DFT STUDY OF PURE AND OXYGEN CONTAMINATED $NaAlH_4$

## 3.1 INTRODUCTION

Sodium alanate ($NaAlH_4$) is a promising hydrogen storage material by virtue of a relatively low dehydriding/rehydriding temperature around 100 °C together with some catalyst in the realm of complex metal hydrides. The experimental studies of solduim alanate have been performed by many dedicated researchers [26, 27, 32, 45, 46], the recently new one of which is the study of the decomposition of a new phase of sodium alanate generated at a high temperature about 180 °C under a pretty high hydrogen pressure of around 200 bars. There is also a highly mobile free aluminum species called S105 phase found in the new phase of sodium alanate via nuclear magnetic resonance (NMR) study [47, 48]. This section of study presents a DFT investigation of the decomposition of pure sodium alanate via phonon calculations. Meanwhile, in the atmospheric environment, oxygen takes up to 21% of air content so that oxygen contamination is sometimes inevitable for those hydrides. Oxygen contamination in sodium alanate may introduce $OH^-$ groups in sodium alanate, which is equivalent to the solid solution of NaOH in $NaAlH_4$ so that the DFT study of the solibility of NaOH in $NaAlH_4$ is also summaried in this section.

## 3.2 COMPUTATIONAL METHOD

Vienna ab initio simulation package (VASP) [49,50] performs all DFT calculations on the $NaAlH_4$ system. The stantdard projector augmented wave (PAW) pseudopotentials were set with the exchange correlation functional of PW91 generalized gradient approximation (GGA) [51,52]. The plane-wave cutoff energy was set as 600 eV together with the electronic convergence criterion of $10^{-6}$ eV for all crystal calculations. Atomic coordinates and lattice shape and constants were relaxed until the forces on each atom were less than 0.005 eV/Å. The harmonic approximation was applied to calculating the phonon frequencies for thermodynamic properties at finite temperatures in the frozen phonon method.

### 3.3 THE DECOMPOSITION OF $NaAlH_4$

$NaAlH_4$ is the white crystal with the density of 54 g/cm$^3$ until the melting temperature of 183 °C. It is a tetragonal crystal with the space group of $I4_1/a$ as well as the optimized lattice constants of $a = b = 4.99$ Å and $c = 11.09$ Å as shown below in figure 3.1.

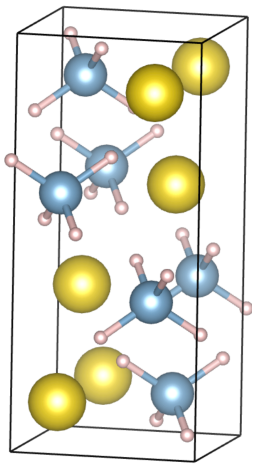

Figure 3.1. Crystal structure of $NaAlH_4$ (Na in yellow, Al in blue, H in white).

The sodium, aluminum and hydrogen are represented by yellow, blue and white balls. Sodium cation is surrounded by $[AlH_4]^-$ anions that are in the tetrahedral shape with aluminum in the center and four hydrogen atoms on the four vertices. The Al-H bond length is 1.64 Å.

In order to investigate the decomposition of sodium alanate, the free energy and some other thermodynamic functions of all possible phases in the Na-Al-H system such as $NaAlH_4$, $Na_3AlH_8$, NaH, Al, Na, $H_2$ etc. are going to be performed at certain temperatures ranging from 0 to 1000 K by using the equation (2.24) in the harmonic approximation.

Table 3.1 shows all the phases that will compete in the invstigation of the $NaAlH_4$ decompositions. The third column in the table is the number of formula units in the crystal DFT calculations; the fourth column lists the Monkhorst−Pack grids used for Brillouin zone integration [53]; the fifth column lists the electronic energy of the

optimized ground states of the crystals; the sixth column lists the zero point energy (ZPE) of the optimized crystals from the phonon results and the final column lists the sum of the energy of the electronic ground state energy plus the zero point energy, which is the total energy of the ground state.

Table 3.1. Competing phases in Na-Al-H system.

| Crystal | Symmetry | f.u.* | k-points | $E_0$ [eV/f.u.] | ZPE [eV/f.u.] | $E=E_0+ZPE$ |
|---|---|---|---|---|---|---|
| $NaAlH_4$ | $I4_1/a$ | 4 | 4x4x2 | -19.63 | 0.80 | -18.83 |
| Al | $Fm\bar{3}m$ | 4 | 12x12x12 | -3.70 | 0.03 | -3.67 |
| $Al_2O_3$ | $R\bar{3}c$ | 6 | 4x4x2 | -37.76 | 0.44 | -37.32 |
| $AlH_3$ | $R\bar{3}c$ | 6 | 4x4x2 | -14.06 | 0.65 | -13.41 |
| $Al(OH)_3$ | $P2_1/c$ | 4 | 6x4x6 | -41.23 | 1.25 | -39.98 |
| Na | $Im\bar{3}m$ | 2 | 12x12x12 | -1.30 | 0.01 | -1.29 |
| $Na_3AlH_6$ | $P2_1/c$ | 2 | 6x6x4 | -30.13 | 1.15 | -28.98 |
| $NaAlO_2$ | $Pna2_1$ | 4 | 6x4x6 | -25.60 | 0.29 | -25.31 |
| NaH | $Fm\bar{3}m$ | 4 | 4x4x4 | -5.15 | 0.15 | -5.00 |
| $Na_2O$ | $Fm\bar{3}m$ | 4 | 6x6x6 | -11.42 | 0.12 | -11.30 |
| $Na_2O_2$ | $P\bar{6}2m$ | 3 | 6x6x8 | -17.07 | 0.10 | -16.97 |
| $NaO_2$ | $Pnnm$ | 2 | 6x6x10 | -13.55 | 0.16 | -13.39 |

*f.u. = formula unit

Those competing phases are all common crystals that may appear in the Na-Al-H system. The free energy of those competing phases are calculated from phonon results in the harmonic approximation at particular temperatures and then the grand canonical linear programming (GCLP) method is used to minimize the total free energy of the system for those competing phases to pick out the phases and calculate their ratios that attain the minimum total free enrgy in the system. Now the phase diagram of the system can be created and the boundaries of the phase regions in the phase diagram represent the decomposition reactions of the system.

All the thermodynamic functions including the free energy of the solid phases can be calculated from the phonon results of the phases. The stability of all phases was

examined via checking the non-transistional phonon frequencies before calculating their thermodynamic functions. The phonon frequencies of sodium alanate is listed below as an example to show its stability.

There are 24 atoms in the 4 f.u. $NaAlH_4$. Therefore there are 72 degrees of freedom (24x3) in the crystal. From table 3.2 shows that all non-transitional phonon frequencies are real numbers except the 3 transitional modes in the last three rows, which indicates that the sodium alanate crystal is stable.

Table 3.2. $NaAlH_4$ phonon frequencies at Γ point (*Frequency in THz).

| Mode | Freq.* | Mode | Freq. | Mode | Freq. | Mode | Freq. |
|---|---|---|---|---|---|---|---|
| 1 | 52.96 | 19 | 25.95 | 37 | 16.98 | 55 | 4.72 |
| 2 | 52.90 | 20 | 25.45 | 38 | 16.88 | 56 | 4.42 |
| 3 | 52.90 | 21 | 25.29 | 39 | 15.12 | 57 | 4.42 |
| 4 | 52.84 | 22 | 24.61 | 40 | 14.69 | 58 | 4.19 |
| 5 | 51.33 | 23 | 24.61 | 41 | 14.69 | 59 | 4.05 |
| 6 | 51.33 | 24 | 24.40 | 42 | 14.13 | 60 | 4.05 |
| 7 | 51.15 | 25 | 24.40 | 43 | 14.13 | 61 | 3.82 |
| 8 | 50.78 | 26 | 24.16 | 44 | 13.73 | 62 | 3.82 |
| 9 | 50.78 | 27 | 24.16 | 45 | 12.68 | 63 | 3.58 |
| 10 | 50.32 | 28 | 23.74 | 46 | 12.68 | 64 | 3.54 |
| 11 | 50.32 | 29 | 22.45 | 47 | 10.88 | 65 | 3.54 |
| 12 | 50.17 | 30 | 22.40 | 48 | 10.88 | 66 | 2.86 |
| 13 | 50.17 | 31 | 22.40 | 49 | 5.76 | 67 | 2.86 |
| 14 | 49.81 | 32 | 21.77 | 50 | 5.76 | 68 | 2.19 |
| 15 | 49.81 | 33 | 21.77 | 51 | 5.60 | 69 | 2.19 |
| 16 | 49.19 | 34 | 20.92 | 52 | 5.60 | 70 | *0.01* |
| 17 | 26.70 | 35 | 20.92 | 53 | 5.54 | 71 | *0.06* |
| 18 | 26.70 | 36 | 16.98 | 54 | 4.72 | 72 | *0.06* |

All the thermodynamic functions can be calculated from the phonon modes of the stable crystals. Figure 3.2 shows the internal energy of soldium alanate from the phonon calculations between 0 and 1000 K. The energy is -18.83 eV/f.u. at 0 K including the electronic ground state energy and the zero point energy. It increases exponentially at low

temperatures obeying Debye approximation and then goes up linearly as the high temperatures approximated as follows.

$$U = 3(6k_B)T \tag{3.1}$$

where the number 6 reprensents there are 6 atoms in the sodium alanate cell.

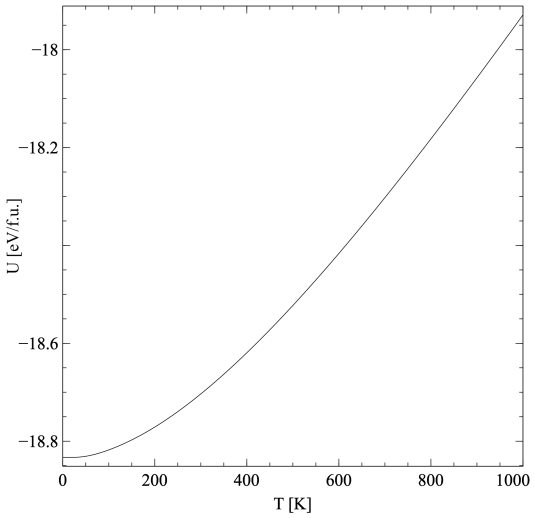


Figure 3.2. Internal energy of $NaAlH_4$ as a function of temperature.

The free energy of sodium alanate from harmonic approximation from 0 to 1000 K is shown in figure 3.3. The free energy goes downhill for the highest value of -18.43 eV/f.u. at 0 K.

Figure 3.4 shows the entropy of sodium alanate from the harmonic approximation at various temperatures. The zero entropy at zero temperature follows the third law of thermodynamics and it goes up with the increase of the temperature.

The thermodynamic functions of a solid phase can be derived from the phonon frequencies by the equations in section 2. However the reactions include the gas phase of hydrogen since all the reactions are regarded to perform in the hydrogen reservoir. The thermodynamic functions of hydrogen should also be evaluated but the gas is a little bit more complicated than the pure solid phases. The chemical potential of hydrogen reprensents the canonical Gibbs free energy of hydrogen gas expressed as follows.

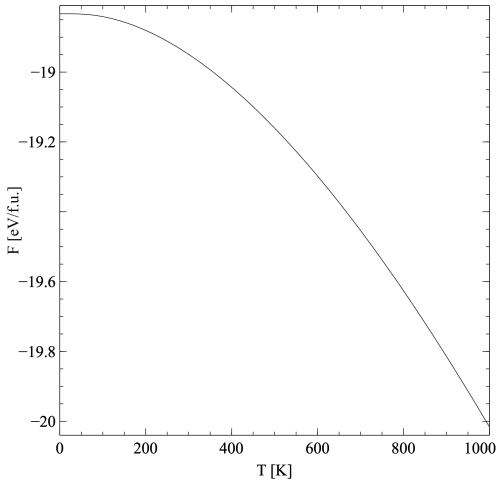


Figure 3.3. Free energy of $NaAlH_4$ as a function of temperature.

$$\mu = U_0 + F_v(T) + F(T, p) \tag{3.2}$$

where $U_0$ is the electronic energy of a hydrogen molecule evaluated by the DFT calculations of a hydrogen molecule in a large volume-conserved cubic cell of 20 Å x 20 Å x 20 Å. $F_v(T)$ is the vibrational free energy that represents the relative elastic oscillations of the both hydrogen atoms at the frequency of 539 meV. $F(T,p)$ contains the translational and rotational motions, along with the interactions between hydrogen molecules. The last term was taken from the experimental entropy of hydrogen of 130.7 J/[mol·K] under standard condition (1 atm and 298 K) [MH/MOH paper: 14]. The entropy of hydrogen can be expressed as follows as a diatomic molecule.

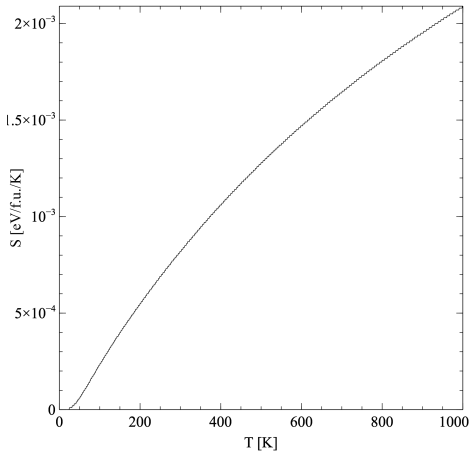


Figure 3.4. Entropy of $NaAlH_4$ as a function of temperature.

$$S = k_B[\left(\frac{7}{2} lnT - lnP\right) + \left(lnP_r - \frac{7}{2} lnT_r\right)] + S_r \quad (3.3)$$

where $k_B$ is the Boltzmann's constant, $T$ and $P$ are the temperature and pressure under which the entropy is calculated and $S_r$ of 130.7 J/[mol·K] is the standard entropy of hydrogen under standard pressure $P_r$ of 1 atm and standard temperature $T_r$ of 298 K.

Figure 3.5 shows the calculated entropy going up from zero between 0 and 1000 K approximated by the theory above.

The internal energy of the gas phase of hydrogen comes mainly from the transitional and rotational parts of the motions of the hydrogen atoms so that the hydrogen energy contains only the electronic part and the transitional and rotational part expressed as follows.

$$U = \frac{5}{2} k_B T + E_0 \quad (3.4)$$

where $E_0$ is the electronic ground state energy of hydrogen molecules.

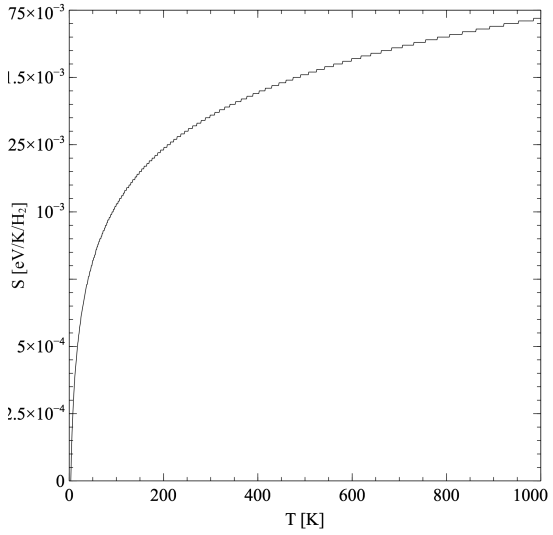


Figure 3.5. Entropy of hydrogen gas as a function of temperature.

Figure 3.6 shows the internal energy of hydrogen gas. The internal energy is linearly proportional to the temperature begginning at the electronic ground state energy of -6.53 eV/$H_2$.

The canonical Gibbs free energy of the gas phase of hydrogen should be evaluated from the internal energy and entropy with the assumption that the hydrogen gas is the ideal gas that satisfies $pV = k_BT$ expressed as follows.

$$G = U - TS + k_BT \tag{3.5}$$

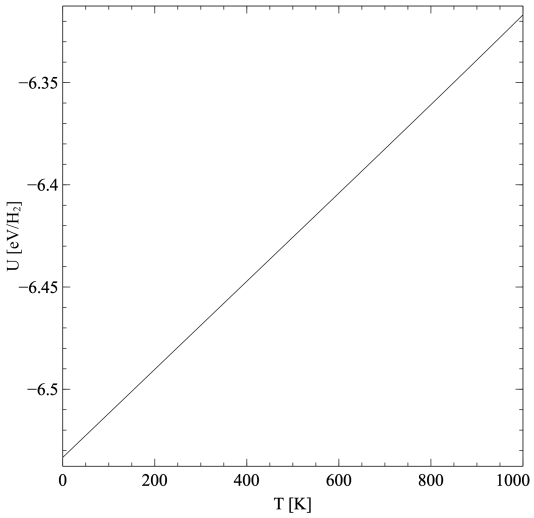


Figure 3.6. Internal energy of hydrogen gas as a function of temperature.

Figure 3.7 shows the Gibbs free energy of hydrogen coming from the internal energy and entropy results of hydrogen, which is also a downhill function with respect to temperature from 0 to 1000 K.

With those thermodynamic functions, the GCLP algorithm is used to probe the decompositions of sodium alanate.

Figure 3.8 shows the theorectical phase diagram of the decompositions of sodium alanate at 1 atm. The y axis represents the temperature of the phase diagram but there is no meaning for x axis. The single phase of sodium alanate was set as the initial phase at a low temperature. The single phase insists until its first decomposition at -50 °C where sodium alante decomposes into sodium hexahydride ($Na_3AlH_6$) and aluminum with the release of hydrogen as follows.

$$3NaAlH_4 \rightarrow Na_3AlH_6 + 2Al + 3H_2 \tag{3.6}$$

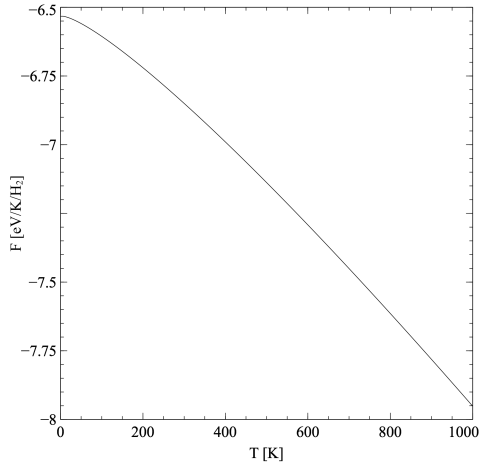


Figure 3.7. Gibbs free energy of hydrogen gas as a function of temperature.

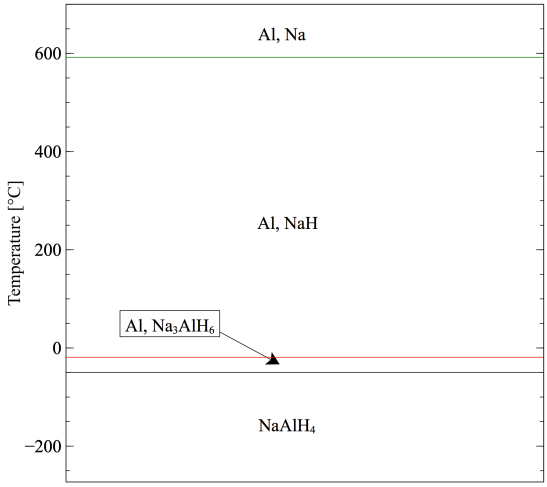


Figure 3.8. Phase diagram of $NaAlH_4$ at 1 atm of $H_2$ reservoir.

The decomposition is predicted by minimizing the total free energy in the competing phases listed in table 3.1 via GCLP algorithm. Figure 3.9 shows the free energy of sodium alanate (black curve) versus the total free enrgy of 1/3 of sodium aluminum hexahydride, 2/3 of aluminum and hydrogen (red curve) that the free energy of $NaAlH_4$ is lower than the total free energy of the decomposition products below the decomposition temperature. The crossing of the free energy is where the decomposition takes place.

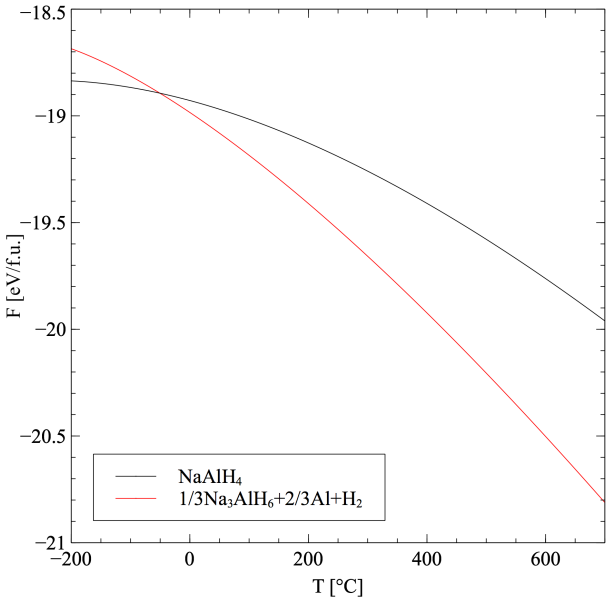


Figure 3.9. Free energy comparison between $NaAlH_4$ and $1/3Na_3AlH_6+2/3Al+H_2$.

After the first decomposition where sodium alanate has decomposed into sodium aluminum hexahydride and aluminum, the phase above the decomposition temperature thus contains $Na_3AlH_6$ and Al as shown in figure 3.8. Then the residue experiences the second decomposition at -19 °C as the red line shows in figure 3.8 where $Na_3AlH_6$ decomposes into NaH and Al with the release of hydrogen as follows.

$$2Na_3AlH_6 \rightarrow 6NaH + 2Al + 3H_2 \quad (3.7)$$

The phase now consists of simple residue crystals of sodium hydride and aluminum. NaH is very stable to decompose at a very high temperature of 592 °C represented as the green line in the phase diagram, which is the last step of the release of hydrogen in the Na-Al-H system as follows.

$$2NaH \rightarrow 2Na + H_2 \quad (3.8)$$

Now all hydrogen stored in sodium alanate has all been released. The only things left behind in the solid residue are pure Na and Al.

The theoretical prediction of the decomposition temperatures and enthalpies is listed in table 3.3 in comparison to the experimental values. The theoretical enthalpies are almost identical to the experimental values whereas the decompositions predicted are far less than the experimental values, which may be partially attributed to the disregard of kinetic barriers in the chemical decompositions and the harmonic approximation.

Table 3.3. Theoretical and experimental enthalpies of the three step decompositions of $NaAlH_4$ at 1 atm of $H_2$ reservoir.

| | $\Delta H$ [54] | | $\Delta H$ (calc.) | |
|---|---|---|---|---|
| | °C | kJ/mol $H_2$ | °C | kJ/mol $H_2$ |
| Reaction 1 | 230 | 25 | -50 | 23 |
| Reaction 2 | 265 | 39 | -19 | 37 |
| Reaction 3 | 660 | 76 | 592 | 78 |

### 3.4 NaOH SOLUBILITY IN $NaAlH_4$

Sodium alanate sometimes undergoes air contamination even in very careful preparation. Oxygen is the most probable contamination to the sodium alanate. Oxydization occurs in many ways, of which the simplest way that forms $OH^-$ groups in substitution for $[AlH_4]^-$ groups in $NaAlH_4$ is considered. $OH^-$ groups may influence the thermal dehydriding/rehydriding properties of sodium alanate. Therefore the solubility of $OH^-$ groups in sodium alanate is a critical care for further investigation of the hydrogen storage properties of sodium alanate. $OH^-$ substituting $[AlH4]^-$ groups in sodium alanate froms sodium hydroxide (NaOH) in sodium alanate. Therefore the solubility of NaOH in $NaAlH_4$ is investigated.

In order to create the solid solution of NaOH in $NaAlH_4$, a 2x2x1 supercell of $NaAlH_4$ is constructed. The conventional cell of sodium alanate contains 4 formula units of $NaAlH_4$. Hence the 2x2x1 supercell contains 16 formula units of $NaAlH_4$. Some of the 16 $[AlH4]^-$ groups were substituted for $OH^-$ randomly to simulate the doping of NaOH in different concentrations such as 1 to 7 $[AlH4]^-$ groups being substitued for $OH^-$ to simulate 6.25%, 12.50%, 18.75%, 25.00%, 31.25%, 37.50% and 43.75% of the solid solution.

Figure 3.10 shows one $OH^-$ group substituted in $NaAlH_4$ supercell to simulate 6.25% $[(NaAlH_4)_{15}NaOH]$ of the solid solution. The lattice constants of the crystal are $a$ = 10.06 Å, $b$ = 9.94 Å and $c$ = 11.19 Å. The cell angles are around 90° ($\alpha$ = 89.75°, $\beta$ = 88.90° and $\gamma$ = 89.67°) due to the $OH^-$ group breaking the symmetry of the crystal of pure sodium alanate. There is one $OH^-$ group in the crystal shown as the red and white end

stick in figure 3.10. The $OH^-$ bond length is calculated as 0.98 Å that is 4.26% longer than the $OH^-$ bond in NaOH (0.94 Å). The direction of the $OH^-$ group is toward the nearest $[AlH_4]^-$ group but $OH^-$ groups in NaOH are toward the sodium cation, which may be caused by the different charge environment for $OH^-$ in $NaAlH_4$ from NaOH.

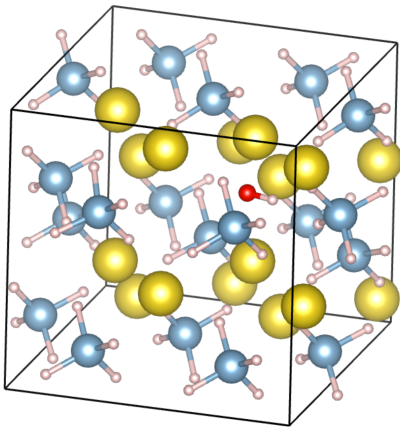

Figure 3.10. Crystal structure of $(NaAlH_4)_{15}NaOH$ (Na in gold, Al in blue, H in white, O in red).

The phonon frequencies of $(NaAlH_4)_{15}NaOH$ totally have 93 atoms in the crystal of the solid solution so that there are 279 degrees of freedom in the crystal. All the 276 phonon frequencies are real numbers except the last three transtional modes shown in table 3.4, which indicates the stability of the solid solution. All the thermodynamic functions of the solid solution can be derived from the phonon frequencies in the harmonic approximation.

Table 3.4. $(NaAlH_4)_{15}NaOH$ transitional phonon frequencies at Γ point (*Frequency in THz).

| Mode | Freq.* | Mode | Freq. | Mode | Freq. | Mode | Freq. |
|---|---|---|---|---|---|---|---|
| 1 | 108.66 | 71 | 26.04 | 141 | 15.82 | 211 | 4.85 |
| 2 | 56.24 | 72 | 26.01 | 142 | 15.76 | 212 | 4.76 |
| 3 | 53.93 | 73 | 25.91 | 143 | 15.56 | 213 | 4.71 |
| 4 | 53.85 | 74 | 25.88 | 144 | 15.48 | 214 | 4.64 |
| 5 | 53.31 | 75 | 25.81 | 145 | 15.19 | 215 | 4.61 |
| 6 | 53.29 | 76 | 25.73 | 146 | 15.17 | 216 | 4.53 |
| 7 | 53.17 | 77 | 25.63 | 147 | 15.14 | 217 | 4.45 |

Table 3.4. $(NaAlH_4)_{15}NaOH$ transitional phonon frequencies at Γ point (*Freq. in THz) (cont.).

| Mode | Freq.* | Mode | Freq. | Mode | Freq. | Mode | Freq. |
|---|---|---|---|---|---|---|---|
| 8 | 53.14 | 78 | 25.58 | 148 | 14.99 | 218 | 4.43 |
| 9 | 53.11 | 79 | 25.43 | 149 | 14.89 | 219 | 4.38 |
| 10 | 53.08 | 80 | 25.4 | 150 | 14.81 | 220 | 4.35 |
| 11 | 53.04 | 81 | 25.29 | 151 | 14.72 | 221 | 4.28 |
| 12 | 52.96 | 82 | 25.25 | 152 | 14.67 | 222 | 4.2 |
| 13 | 52.93 | 83 | 25.2 | 153 | 14.52 | 223 | 4.18 |
| 14 | 52.92 | 84 | 25.07 | 154 | 14.48 | 224 | 4.15 |
| 15 | 52.83 | 85 | 24.94 | 155 | 14.31 | 225 | 4.1 |
| 16 | 52.59 | 86 | 24.91 | 156 | 14.28 | 226 | 4.05 |
| 17 | 52.44 | 87 | 24.87 | 157 | 14.16 | 227 | 4.01 |
| 18 | 52.35 | 88 | 24.77 | 158 | 14.03 | 228 | 3.99 |
| 19 | 52.33 | 89 | 24.73 | 159 | 13.91 | 229 | 3.97 |
| 20 | 52.17 | 90 | 24.64 | 160 | 13.84 | 230 | 3.91 |
| 21 | 52.07 | 91 | 24.61 | 161 | 13.77 | 231 | 3.87 |
| 22 | 51.69 | 92 | 24.55 | 162 | 13.67 | 232 | 3.77 |
| 23 | 51.57 | 93 | 24.47 | 163 | 13.62 | 233 | 3.73 |
| 24 | 51.52 | 94 | 24.42 | 164 | 13.48 | 234 | 3.69 |
| 25 | 51.4 | 95 | 24.32 | 165 | 13.39 | 235 | 3.65 |
| 26 | 51.27 | 96 | 24.24 | 166 | 13.2 | 236 | 3.63 |
| 27 | 51.15 | 97 | 24.13 | 167 | 13.17 | 237 | 3.6 |
| 28 | 51.11 | 98 | 24.12 | 168 | 13.04 | 238 | 3.57 |
| 29 | 50.96 | 99 | 24.03 | 169 | 12.85 | 239 | 3.57 |
| 30 | 50.93 | 100 | 23.94 | 170 | 12.67 | 240 | 3.5 |
| 31 | 50.86 | 101 | 23.89 | 171 | 12.5 | 241 | 3.48 |
| 32 | 50.8 | 102 | 23.8 | 172 | 12.39 | 242 | 3.42 |
| 33 | 50.73 | 103 | 23.69 | 173 | 12 | 243 | 3.39 |
| 34 | 50.7 | 104 | 23.67 | 174 | 11.81 | 244 | 3.35 |
| 35 | 50.66 | 105 | 23.51 | 175 | 11.73 | 245 | 3.32 |
| 36 | 50.56 | 106 | 23.47 | 176 | 11.53 | 246 | 3.27 |
| 37 | 50.53 | 107 | 23.19 | 177 | 11.19 | 247 | 3.22 |
| 38 | 50.5 | 108 | 22.97 | 178 | 11.08 | 248 | 3.17 |
| 39 | 50.42 | 109 | 22.87 | 179 | 10.93 | 249 | 3.14 |
| 40 | 50.33 | 110 | 22.74 | 180 | 10.74 | 250 | 3.09 |
| 41 | 50.3 | 111 | 22.65 | 181 | 10.33 | 251 | 3.06 |
| 42 | 50.24 | 112 | 22.5 | 182 | 10.05 | 252 | 3.01 |

Table 3.4. $(NaAlH_4)_{15}NaOH$ transitional phonon frequencies at Γ point (*Frequency in THz) (cont.).

| Mode | Freq.* | Mode | Freq. | Mode | Freq. | Mode | Freq. |
|---|---|---|---|---|---|---|---|
| 43 | 50.21 | 113 | 22.47 | 183 | 9.72 | 253 | 3 |
| 44 | 50.17 | 114 | 22.42 | 184 | 9.3 | 254 | 2.89 |
| 45 | 50.08 | 115 | 22.24 | 185 | 8.7 | 255 | 2.88 |
| 46 | 50.03 | 116 | 22.12 | 186 | 6.4 | 256 | 2.84 |
| 47 | 49.94 | 117 | 22.08 | 187 | 6.28 | 257 | 2.83 |
| 48 | 49.88 | 118 | 21.85 | 188 | 5.79 | 258 | 2.81 |
| 49 | 49.83 | 119 | 21.81 | 189 | 5.73 | 259 | 2.79 |
| 50 | 49.74 | 120 | 21.7 | 190 | 5.64 | 260 | 2.73 |
| 51 | 49.72 | 121 | 21.68 | 191 | 5.61 | 261 | 2.69 |
| 52 | 49.68 | 122 | 21.53 | 192 | 5.59 | 262 | 2.65 |
| 53 | 49.62 | 123 | 21.43 | 193 | 5.56 | 263 | 2.6 |
| 54 | 49.52 | 124 | 21.29 | 194 | 5.53 | 264 | 2.53 |
| 55 | 49.47 | 125 | 21.12 | 195 | 5.51 | 265 | 2.51 |
| 56 | 49.4 | 126 | 20.78 | 196 | 5.47 | 266 | 2.49 |
| 57 | 49.17 | 127 | 20.73 | 197 | 5.44 | 267 | 2.44 |
| 58 | 49.06 | 128 | 20.65 | 198 | 5.39 | 268 | 2.42 |
| 59 | 48.94 | 129 | 20.55 | 199 | 5.36 | 269 | 2.37 |
| 60 | 48.88 | 130 | 19.95 | 200 | 5.3 | 270 | 2.3 |
| 61 | 48.49 | 131 | 19.8 | 201 | 5.25 | 271 | 2.27 |
| 62 | 27.29 | 132 | 19.72 | 202 | 5.21 | 272 | 2.1 |
| 63 | 26.79 | 133 | 19.53 | 203 | 5.19 | 273 | 1.99 |
| 64 | 26.7 | 134 | 19.4 | 204 | 5.16 | 274 | 1.9 |
| 65 | 26.47 | 135 | 19.2 | 205 | 5.13 | 275 | 1.71 |
| 66 | 26.34 | 136 | 18.93 | 206 | 5.08 | 276 | 1.68 |
| 67 | 26.3 | 137 | 17.73 | 207 | 5.06 | 277 | *0.09* |
| 68 | 26.27 | 138 | 17.09 | 208 | 4.96 | 278 | *0.11* |
| 69 | 26.19 | 139 | 16.65 | 209 | 4.91 | 279 | *0.19* |
| 70 | 26.15 | 140 | 16.21 | 210 | 4.86 | - | - |

Figure 3.11 shows the internal energy of the solid solution $(NaAlH_4)_{15}NaOH$ from phonon frequencies in the harmonic approximation. The energy begins at -18.43 eV/f.u. at absolute zero temperature that includes the electronic ground state energy and the zero point energy. The internal energy increases with the increase of temperature and grows linearly with respect to temperature at high temperatures that obeys the high temperature

solid internal energy rule that all internal energy increase comes from the oscillation of atoms in the solid.

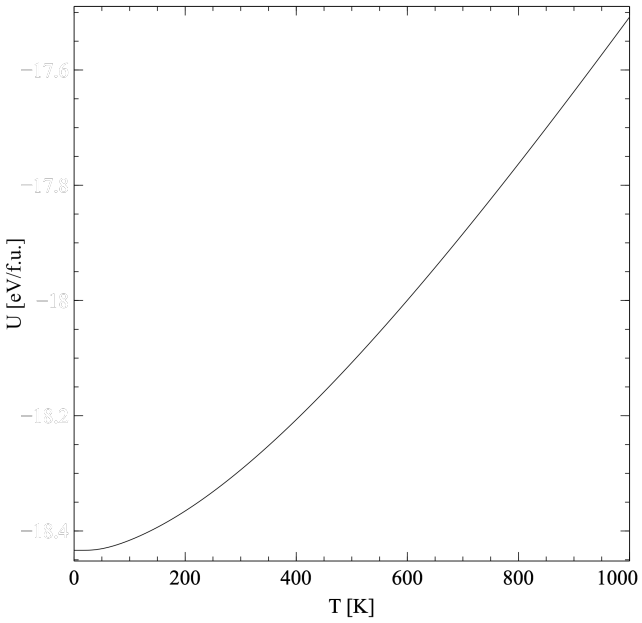


Figure 3.11. Internal energy of $(NaAlH_4)_{15}NaOH$ as a function of temperature.

The entropy of the solid solution is plotted in figure 3.12 derived from the phonon frequencies. The entropy starts at zero for absolute zero temprature and the entropy grows with the increase of temperature.

Figure 3.13 shows the free energy of the solid solution also evaluated from the phonon freqencies in the harmonic approximation. The initial free energy at 0 K is -18.43 eV/f.u. idential to the internal energy including the electronic ground state energy and the zero point energy. The free energy decreases with the increase of temperature due to the increase of entropy.

In order to calculate the solubility of $(NaAlH_4)_{15}NaOH$, the competing phases of $(NaAlH_4)_{15}NaOH$, $NaAlH_4$ and NaOH are performed by GCLP algorithm to find the favorable phases at different temperatures as shown in table 3.5.

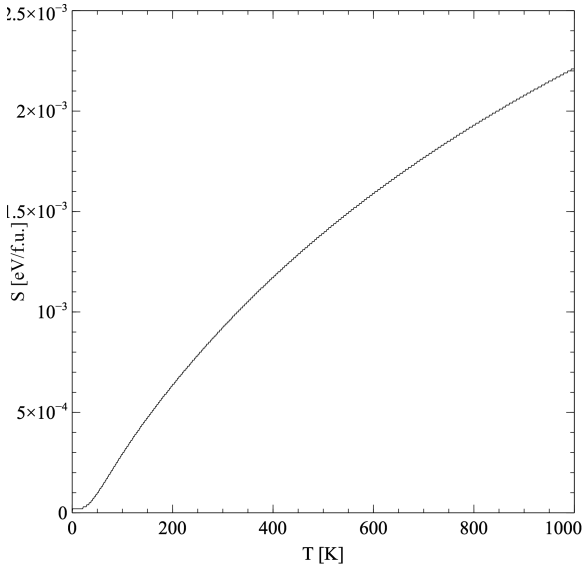


Figure 3.12. Entropy of $(NaAlH_4)_{15}NaOH$ as a function of temperature.

The free energies of all the competing phases are calculated by the phonon frequencies in the harmonic approximation. Then the change of the free energy can be calculated as follows.

$$\Delta F = F[(NaAlH_4)_{15}NaOH] - F(NaAlH_4) - F(NaOH) \quad (3.9)$$

The solid solution $(NaAlH_4)_{15}NaOH$ is favorable when the change of the free energy $\Delta F$ is less than zero. At the critical temperature where $\Delta F = 0$ is the temperature where the solid solution start forming.

Table 3.5. Competing phases for solubility of $(NaAlH_4)_{15}NaOH$.

| Crystal | Symmetry | f.u. | k-points | $E_0$* | ZPE* | $E=E_0+ZPE$* |
|---|---|---|---|---|---|---|
| $NaAlH_4$ | $I4_1/a$ | 4 | 4x4x2 | -19.63 | 0.80 | -18.83 |
| NaOH | $P1$ | 32 | 2x2x2 | -13.79 | 0.39 | -13.40 |
| $(NaAlH_4)_{15}NaOH$ | $P1$ | 1 | 4x4x2 | -306.95 | 12.34 | -294.61 |

*Energy in eV/f.u.

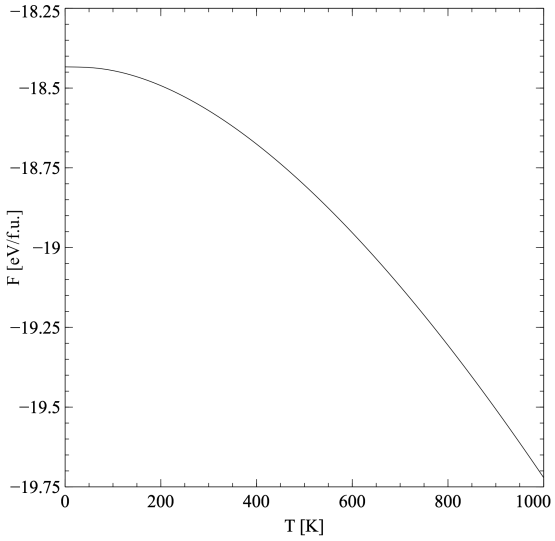


Figure 3.13. Free energy of $(NaAlH_4)_{15}NaOH$ as a function of temperature.

Figure 3.14 shows the comparison between the free energy of the solid solution and the separate phases. The free enrgy of the separate phases is less than that of the solid solution below the critical temperature of about 574 K (301 °C) but the free energy of the solid solution becomes lower than the separate phase above the critical temperature, which inidicates the fact that the solid solution is favorable above the critical temperature. The separate phases mix into the solid solution at the critical temperature as follows.

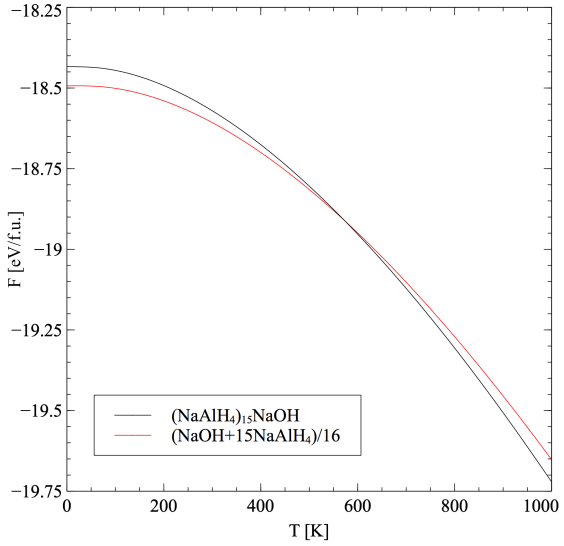


Figure 3.14. Free energy comparison between $(NaAlH_4)_{15}NaOH$ and $NaAlH_4$ + NaOH.

$$15NaAlH_4 + NaOH \rightarrow (NaAlH_4)_{15}NaOH \quad (3.10)$$

The enthalpy of the above reaction is about 8 kJ/mol $(NaAlH_4)_{15}NaOH$ evaluated by GCLP algorithm.

The favorability of all other concentrations of the solid solution can also be evaluated by GCLP algorithm. All the critical temperatures of the solid solution are much higher than the decomposition temperature of sodium alanate, which indicates the fact that the solid solution may form at higher hydrogen pressure where sodium alanate may decompose at higher temperature beyond the critical temperatures of the solid solution.

## 3.5 CONCLUSION

The thermodynamic functions are derived from the phonon calculations in the harmonic approximation by DFT method. The decompositions of sodium alanate are simulated by grand canonical linear programming method that correctly predicts the decompositions of sodium alanate. The solubility of NaOH in sodium alanate was simulated by GCLP algorithm, which implies that $OH^-$ groups may be favorable in $NaAlH_4$ at high temperature and high atmospheric pressure environment. The contamination by oxygen to form $OH^-$ groups in sodium alanate crystal may influence the thermodynamic behavior of the decompositions of sodium alanate. Some future study should be implemented to investigate the further properties of the contaminated sodium alanate to see its effect to the decomposition behavior.

# 4 DFT STUDY OF ALKALI METAL HYDRIDES AND HYDROXIDES SYSTEM

## 4.1 INTRODUCTION

The dehydriding/rehydriding of complex metal hydrides are highly influenced by the diffusion of hydrogen and the mass transport of metals in the complex metal hydrides.

A fast diffusion of those species will accelerate the rate of dehydriding/rehydriding processes. Sodium alanate decomposes in three steps, for example, which decomposes into sodium aluminum hexahydride ($Na_3AlH_6$) and aluminum in the first step. Sodium aluminum hexahydride decomposes again at a slight higher temperature into sodium hydride and aluminum in the second step. The sodium hydride can fully decompose into sodium and release hydrogen at its melting temperature of around 425 °C [55]. The process can be reversed by adding a few transition metal catalyst [56] so that sodium alanate can be a promising candidate for hydrogen storage material. Sodium alanate should be stored airtightly to keep away from oxygen contamination. However the contamination are always inevitable even in the most careful preparation. Therefore the contamination effects in the dehydriding/rehydriding processes become a valuable topic for discussion.

Besides soldium alanate, some other complex metal hydrides also have their own advantages such as lithium aluminum hydride ($LiAlH_4$) with its large hydrogen weight percentage and potassium aluminum hydride ($KAlH_4$) reversible without any help of a catalyst [57]. The reversibility of those complex metal hydrides may be influenced by the impurities generated from the oxygen contamination that influences the diffusion rate of metal transport in the solid solution of MH/MOH phase where M represents metal. The alkali metal hydrides are the intermetiate products/reactants of those coresponding complex medal hydrides in the dehydrding/rehydriding processes. Thus the solubility of $OH^-$ groups in MH is of important interest for understanding the fundamental mechanism of the properties of hydrogen storage in the promising materials.

This section presents a comprehensive study of the density functional theory (DFT) investigation of the solid solubility of MOH in MH where M ={Li, Na, K, Rb and Cs}. The critical temperatures of the onset of mixing of MH and MOH at fixed

MH/MOH ratios were calculated instead of the full pseudo-phase diagram due to the difficulty of the soft modes in MOH structures attributed to the rotations of $OH^-$ groups in those structures. The calculations also ingnore some other complicated considerations like kinetic barriers that require an atom to take more energy when hopping from one site to another. Thus the ignorance lower the predicted critical temperatures.

## 4.2 COMPUTATIONAL METHODS

The Vienna ab initio simulation package (VASP) [49, 50] performs all of the density functional theory (DFT) calculations, which used standard projector augmented wave (PAW) pseudopotentials with the generalized gradient approximation of PW91 [51, 52] for the exchange correlation. The plane wave cutoff energy was set as 600 eV and the electronic convergence criterion was $10^{-6}$ eV. The ionic relaxation terminating forces were set less than 0.005 eV/Å. The phonon calculations were performed using the direct phonon method for thermodynamic functions.

## 4.3 MH CRYSTAL STRUCTURES

MH, where M={Li, Na, K, Rb and Cs}, has cubic $Fm\bar{3}m$ structures as shown in the following figure 4.1 [58].

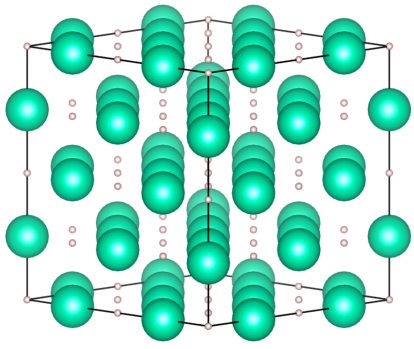

Figure 4.1. Crystal structure of MH (M in green, H in white).

The crystal shows a 2x2x2 supercell of MH structure. There are totally 64 atoms (32 of M and 32 of H). The green balls represent the alkali metal atoms and the white small dots represent the hydrogen atoms. It is a face centered crystal. The lattice constants are growing from lithium to ceseium as 8.02 Å, 9.64 Å, 11.37 Å, 12.07 Å and 12.85 Å for Li, Na, K, Rb and Cs respectively. The relaxation calculations were performed using 2x2x2 Monkhorst−Pack grids for Brillouin zone integration [53] due to such a high number of atoms.

## 4.4 MOH CRYSTAL STRUCTURES

MOH have complicated crystal structures and the phases are changing over temperature. LiOH is always tetragonal (space group *P*4/*nmm*) with $a$ = 3.549 Å and $c$ = 4.334 Å up to its metling temperature of 473 °C [59]. NaOH exhibits polymorphism whose low temperature structure is orthorhombic (space group: *Bmmb*) with $a$ = 3.401 Å, $b$ = 3.398 Å and $c$ = 11.378 Å [59] until 241 °C. The phase reduces its symmetry from orthorhombic to monoclinic (space group: $P2_1/m$) with $a$ = 3.435 Å, $b$ = 3.445 Å, $c$ = 6.080 Å and a distortion of $\beta$ = 109.9° up to 295 °C [59]. The crystal becomes a cubic structure with space group of $Fm\bar{3}m$ for the lattice constant of 5.10 Å over 295 °C [59]. KOH has the monoclinic structure with space group of $P2_1/m$ for $a$ = 5.903 Å, $b$ = 3.942 Å, $c$ = 7.722 Å and $\beta$ = 110.4° until 22 °C and transforms to another monoclinic structure of $P2_1/m$ for $a$ = 3.955 Å, $b$ = 3.998 Å, $c$ = 5.731 Å and $\beta$ = 103.8° between 22 °C and 244 °C. Then it eventually transforms to the cubic crystal of $Fm\bar{3}m$ with the lattice constant of 5.752 Å at high temperatures [59]. At very low temperature until −8 °C, RbOH exhibits orhorhombic structure with the space group of $Cmc2_1$ for $a$ = 4.124 Å, $b$ = 11.176 Å, $c$ = 4.211 Å [59], which reduces its symmetry into monoclinic of $P2_1/m$ up to 235 °C for $a$ = 4.151 Å, $b$ = 4.245 Å, $c$ = 6.030 Å and $\beta$ = 104.5° [59].The cubic structure appears over 235 °C with the lattice constant of 6.080 Å [59]. There is an orhorhombic struture of *Pmnb* of $a$ = 4.328 Å, $b$ = 4.478 Å, $c$ = 11.586 Å for CsOH at low temperatures below -39 °C, over which becomes *Bmmb* for $a$ = 4.358 Å, $b$ = 4.524 Å, $c$ = 12.018 Å until 225 °C. Over 225 °C, the structure also transforms to the cubic $Fm\bar{3}m$ with the lattice constant of 6.427 Å [59]. All MOH structures transform to the cubic

structure at very high temperatures except LiOH, which may be attributed to the free rotation of $OH^-$ groups in MOH structures.

Despite the complicated situation of MOH phases, the literature phases are always generating soft modes due to the harmonic treatment of the phonon calculations. The anharmonic effects at finite temperatures may stabilize the soft modes. The calculations relaxed the 2x2x2 supercells of totally 32 atoms of MOH that all generate soft modes. The mode following method was used to find the stable structures at 0 K in the harmonic approximation, which will break the symmetries of MOH. The mode-followed crystals will be used for the theoretical investigation of the solid solubility of MH/MOH systems.

Table 4.1. shows the soft modes of NaOH supercell. There are 10 soft modes, the first two of which (279 and 280) are transitional modes. Therefore there are 8 non-transitional soft modes indicating the instability of the supercell. The mode following method was used to add the displacements of the last soft mode (288) to the original coordinates to get a new structure that is stable containing only 3 transitional soft modes as shown in table 4.2.

Table 4.1. 2x2x2 NaOH supercell soft modes.

| Mode | Freq. [THz] |
|---|---|
| 279 | 0.024 |
| 280 | 0.065 |
| 281 | 6.351 |
| 282 | 6.608 |
| 283 | 6.608 |
| 284 | 6.717 |
| 285 | 6.849 |
| 286 | 6.889 |
| 287 | 6.889 |
| 288 | 6.986 |
| 279 | 2.503 |
| 280 | 2.503 |

Table 4.2. Last 10 phonon modes of mode-followed 2x2x2 NaOH supercell.

| Mode | Freq. [THz] |
|---|---|
| 281 | 2.324 |
| 282 | 2.324 |
| 283 | 1.934 |
| 284 | 1.934 |
| 285 | 0.896 |
| 286 | *0.020* |
| 287 | *0.067* |
| 288 | *0.101* |

The mode following method was also applied to the remaining alkali metal hydroxides to reach their stable structures that may be used to the following thermal property calculations.

## 4.5 $MH_{1-x}(OH)_x$ SOLID SOLUTION CRYSTAL STRUCTURES

The study focuses on the MH-rich side of the solid solutions so as to investigate the oxygen contamination in MH. The solid solutions were construncted from adding oxygen atoms around the hydrogen atoms in one of six octahedral positions in the 2x2x2 supercells of the cubic MH structure to form the OH groups along the coordinate axis. The 2x2x2 supercell contains 32 hydrogen atoms and can be added up to 16 oxygen atoms to form $x$ = 3.125%, 6.250%, 9.375%, 12.500%, 15.625%, 18.750%, 21.875%, 25.000%, 28.125%, 31.250%, 34.375%, 37.500%, 40.625%, 43.750%, 46.875% and 50.000% of solid solutions of $MH_{1-x}(OH)_x$. The OH bond length was set as 0.88 Å initially a little bit shorter than the traditional OH bond length of 0.94 Å in NaOH, which may be optimized to a good length after the relaxation. The simulated annealing algorithm (SA) was applied to placing the oxygen atom postions randomly to try to spread over the OH groups in the crystal cell uniformly using the cost function of equation (2.19), where $e_i$ and $e_j$ are the reference charges for different atoms in the crytal cell for M, O and H, set as +1, +1 and -2 respectively. We do not really have to take care

of the actual charges on those atoms. Only the reference charges that emphasize the repulsion and attraction between atoms should be set in order to minimize the energy function later. In the equation, $r_{ij}$ is the distance between two atoms. The simulated annealed crystals may have a uniform distribution of OH groups in the crystal so that all the OH groups keep as far as possible. Then the crystal was relaxed by DFT calculations to reach their correct structures. In the simulated annealing method, all crystals should have a periodic boundary condition. Therefore the Coulomb interaction was calculated within a radius of one unit cell dimension centered on every atom. The simulated annealing method tried to reduce the energy function (2.5.1) for MH/MOH crystal structures. The new energy of a random move of any atom in the crystal ($E_2$) was compared with the energy of the previous configuration ($E_1$). Any move that leads to the redcution of the energy ($E_2 < E_1$) was accepted and the uphill moves ($E_2 > E_1$) were accepted with a probabiliy of $e^{-(E_2-E_1)/T}$ to prevent the configuration from staying in a local minimum forever in the configuration space. Here the reference annealing temperature $T$ started from a relatively high number $T_i = 100$ and went down exponentially following $T_n = T_i e^{-[(1/N)ln(T_i/T_f)]n}$ to a very low temperature close to zero like $T_f = 1 \times 10^{-3}$, where $N$ is the total temperature steps set as 30 and $n$ represents the $n$-th step.

Figure 4.2 illustrates the crytal structure of $MH_{1-x}(OH)_x$, where OH groups are randomly distributed in the crystal. The OH groups were optimized toward the diagonal direction. The bond length was optimized about 0.97 Å.

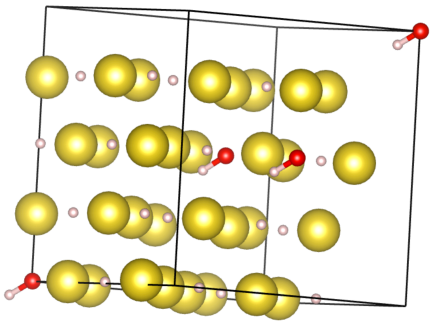

Figure 4.2. Crystal structure of a sample of $MH_{1-x}(OH)_x$ (M in gold, H in white, O in red).

## 4.6 MH, MOH AND SOLID SOLUTION THERMODYNAMIC FUNCTIONS

Thermodynamic functions like internal energy, free energy, entropy etc. can be evaluated from the phonon modes of the phases after the relaxation of the phases as shown in table 4.3.

Table 4.3. K-point meshes, total energies and zero point energies of competing structures.

| Material | k-point | $U_E$ (eV) | ZPE (eV) |
|---|---|---|---|
| $H_2$ | 2x2x2 | -6.80 | 0.27 |
| LiH | 2x2x2 | -197.66 | 7.16 |
| LiOH | 2x2x2 | -240.41 | 6.91 |
| $Li_2O$ | 4x4x4 | -57.75 | 0.89 |
| Na | 4x4x4 | -20.89 | 0.25 |
| NaH | 2x2x2 | -164.94 | 5.09 |
| NaOH | 2x2x2 | -441.13 | 12.56 |
| $Na_2O$ | 6x6x6 | -45.66 | 0.49 |
| K | 4x4x4 | -16.67 | 0.19 |
| KH | 2x2x2 | -156.25 | 4.04 |
| KOH | 2x2x2 | -431.45 | 11.98 |
| Rb | 2x2x2 | -14.87 | 0.11 |
| RbH | 2x2x2 | -150.16 | 3.49 |
| RbOH | 2x2x2 | -424.17 | 11.52 |
| Cs | 2x2x2 | -13.79 | 0.08 |
| CsH | 2x2x2 | -147.85 | 3.06 |
| $Li_{32}H_{31}OH$ | 2x2x2 | -205.86 | 7.28 |
| $Na_{32}H_{31}OH$ | 2x2x2 | -173.35 | 5.25 |
| $Na_{32}H_{30}(OH)_2$ | 2x2x2 | -181.77 | 5.46 |
| $Na_{32}H_{29}(OH)_3$ | 2x2x2 | -190.20 | 5.65 |
| $Na_{32}H_{28}(OH)_4$ | 2x2x2 | -198.66 | 5.86 |
| $Na_{32}H_{27}(OH)_5$ | 2x2x2 | -207.01 | 6.05 |
| $Na_{32}H_{26}(OH)_6$ | 2x2x2 | -215.71 | 6.29 |
| $Na_{32}H_{25}(OH)_7$ | 2x2x2 | -224.27 | 6.50 |
| $Na_{32}H_{24}(OH)_8$ | 2x2x2 | -232.44 | 6.65 |
| $Na_{32}H_{23}(OH)_9$ | 2x2x2 | -241.33 | 6.97 |
| $Na_{32}H_{22}(OH)_{10}$ | 2x2x2 | -249.98 | 7.22 |
| $Na_{32}H_{21}(OH)_{11}$ | 2x2x2 | -258.43 | 7.47 |
| $Na_{32}H_{20}(OH)_{12}$ | 2x2x2 | -266.99 | 7.70 |

Table 4.3. K-point meshes, total energies and zero point energies of competing structures (cont.).

| Material | k-point | $U_E$ (eV) | ZPE (eV) |
|---|---|---|---|
| $Na_{32}H_{19}(OH)_{13}$ | 2x2x2 | -275.55 | 7.89 |
| $K_{32}H_{31}OH$ | 2x2x2 | -164.70 | 4.19 |
| $K_{32}H_{30}(OH)_2$ | 2x2x2 | -173.16 | 4.41 |
| $K_{32}H_{28}(OH)_4$ | 2x2x2 | -190.13 | 4.82 |
| $K_{32}H_{27}(OH)_5$ | 2x2x2 | -198.64 | 5.05 |
| $K_{32}H_{26}(OH)_6$ | 2x2x2 | -207.20 | 5.27 |
| $K_{32}H_{25}(OH)_7$ | 2x2x2 | -215.77 | 5.50 |
| $K_{32}H_{24}(OH)_8$ | 2x2x2 | -224.14 | 5.66 |
| $K_{32}H_{23}(OH)_9$ | 2x2x2 | -232.78 | 5.95 |
| $K_{32}H_{22}(OH)_{10}$ | 2x2x2 | -241.35 | 6.24 |
| $K_{32}H_{21}(OH)_{11}$ | 2x2x2 | -249.77 | 6.41 |
| $K_{32}H_{20}(OH)_{12}$ | 2x2x2 | -258.31 | 6.69 |
| $K_{32}H_{19}(OH)_{15}$ | 2x2x2 | -284.11 | 7.43 |
| $Rb_{32}H_{31}OH$ | 2x2x2 | -158.16 | 3.67 |
| $Rb_{32}H_{30}(OH)_2$ | 2x2x2 | -167.05 | 3.88 |
| $Rb_{32}H_{29}(OH)_3$ | 2x2x2 | -175.54 | 4.07 |
| $Rb_{32}H_{28}(OH)_4$ | 2x2x2 | -184.01 | 4.28 |
| $Rb_{32}H_{27}(OH)_5$ | 2x2x2 | -192.50 | 4.50 |
| $Rb_{32}H_{24}(OH)_8$ | 2x2x2 | -217.98 | 5.10 |

Table 4.3 shows all the structures taking part in the calculations together with their k-point mesh settings, the optimized total electronic energy and the zero point energy from the phonon modes.

The internal energy of MH as a function of temperature was plotted in figure 4.3. The internal energy was calculated from the 2x2x2 supercell of cubic MH crystal structures. They are growing functions with the increase of temperature and the slopes of the functions are almost identical at high temperatures obeying the law of the internal energy at high temperatures. The interanl energy at 0 K includes the electronic ground state energy and zero point energy are -5.95, -5.00, -4.76, -4.58 and -4.52 eV/f.u. for LiH, NaH, KH, RbH and CsH respectively, which are increasing with the increase of the atomic number attributed mainly to the lossening of the electronic bonding attraction.

The free enrgies of the alkali metal hydrides were able to be calculated also from the phonon modes by equation (2.24). They are downhill functions as a function of temperature as shown in figure 4.4. The values at 0 K are identical to the internal energies including the electronic ground state energy and zero point energy. All the functions have similar downhill slopes except CsH that goes down much faster than other metal hydrides crossing over RbH and KH due to the lower phonon frequencies of CsH.

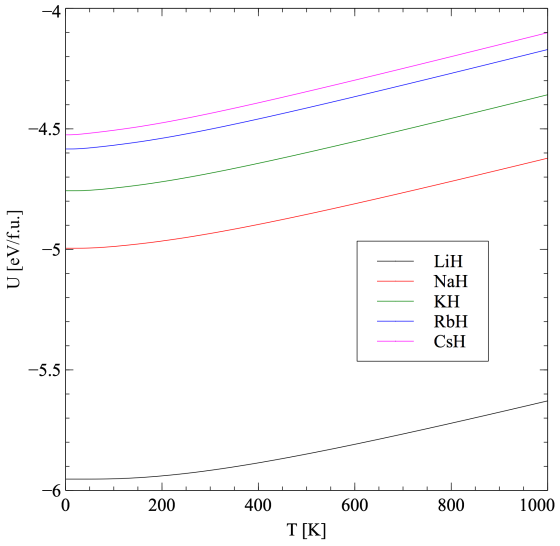


Figure 4.3. Internal energy of MOH as a function of temperature.

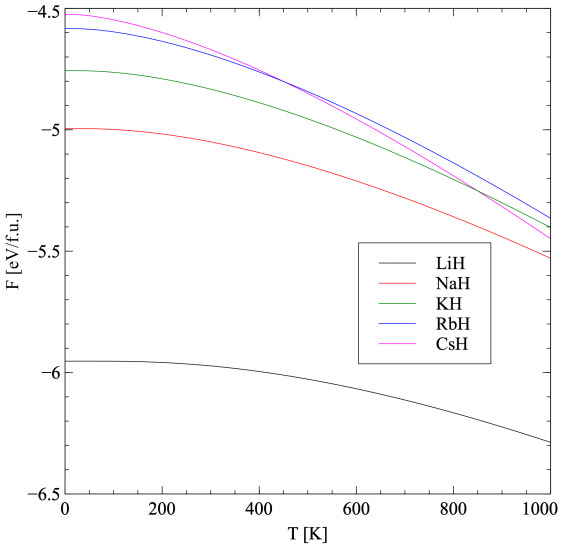


Figure 4.4. Free energy of MH as a function of temperature.

The entropies of MH are plotted in figure 4.5 from the equation (2.25) in the harmonic approximation, all of which start from 0 and increase as a function of temperature. The entropies of heavier alkali metal hydrides are greater than the entropies of lighter alkali metal hydrides.

Figure 4.6 shows the internal energy of mode followed MOH. The structures contain 32 formula units of MOH. The internal energies are also uphill functions starting from -14.59, -13.39, -13.11, -12.90 and -12.81 eV/f.u. for LiOH, NaOH, KOH, RbOH and CsOH respectively. Heavier alkali metal hydroxide has higher internal energy for the same trend as that of MH.

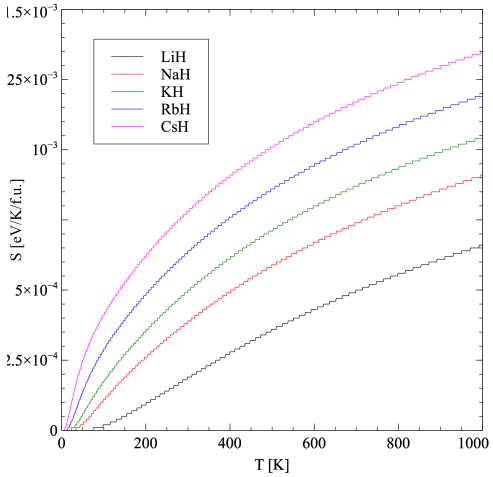


Figure 4.5. Entropy of MOH as a function of temperature.

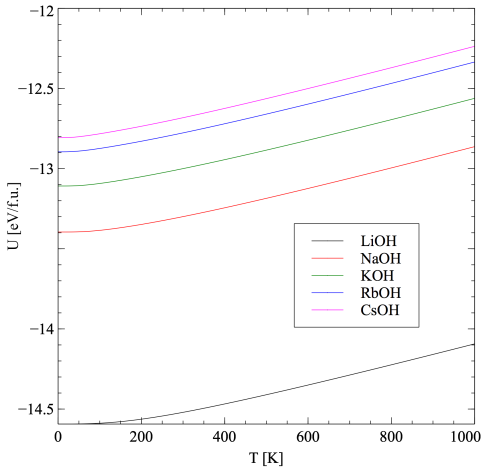


Figure 4.6. Internal energy of MOH as a function of temperature.

The free energy from the phonon modes in harmonic approximation was plotted in figure 4.7. The free energy is always a decreasing function of temperature. They include the electronic ground state energy as well as the zero point energy at the absolute zero temperature. CsOH goes down faster than other metal hydroxides crossing over RbOH above 800 K due to the lower phonon frequencies of CsOH.

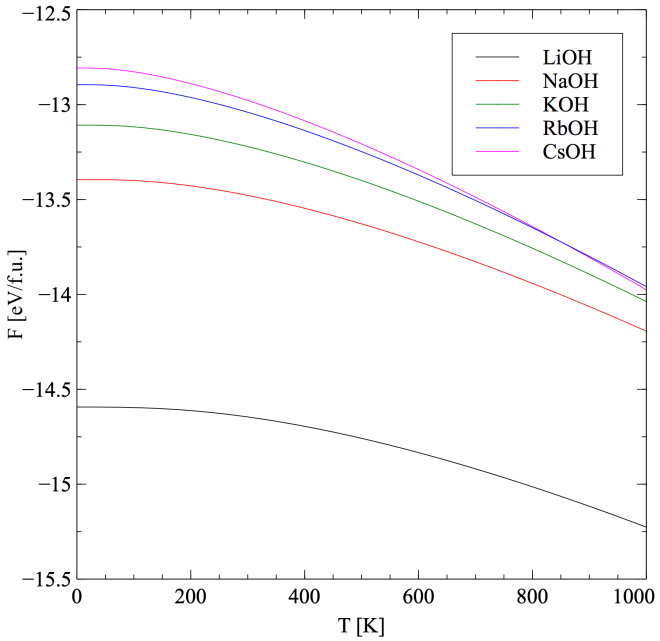


Figure 4.7. Free energy of MOH as a function of temperature.

The calculated entropy of MOH was plotted in figure 4.8. They are growing with the increase of temperature, in which LiOH goes up over NaOH and KOH. The entropy of LiOH crosses RbOH around 400 K.

The thermodynamic functions of the solid solutions can also be calculated from the phonon modes. The internal energies of 3.125% solid solution of Na, K and Rb are shown in figure 4.9, which are uphill functions starting from -5.25, -5.02, -4.84 eV/f.u. for $NaH_{31}OH$, $KH_{31}OH$ and $RbH_{31}OH$ respectively including the electronic ground state energy and the zero point energy. They also have parallel uphill slopes at high temperatures and the heavier alkali metals have heavier internal energy for the solid solution.

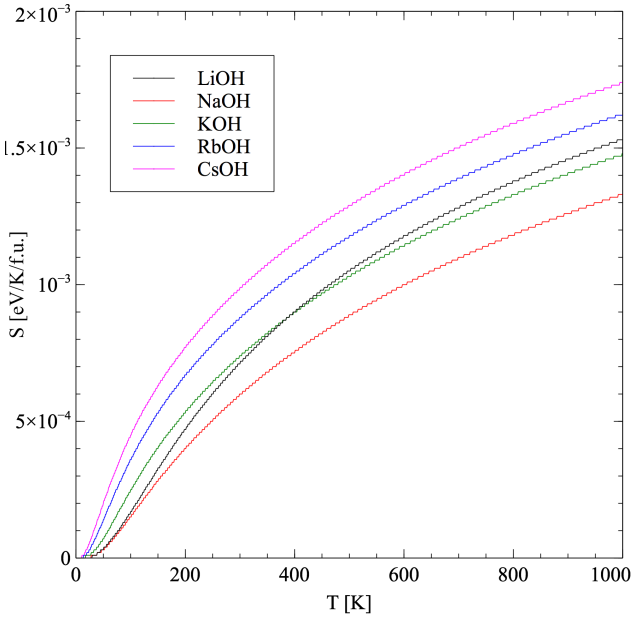


Figure 4.8. Entropy of MOH as a function of temperature.

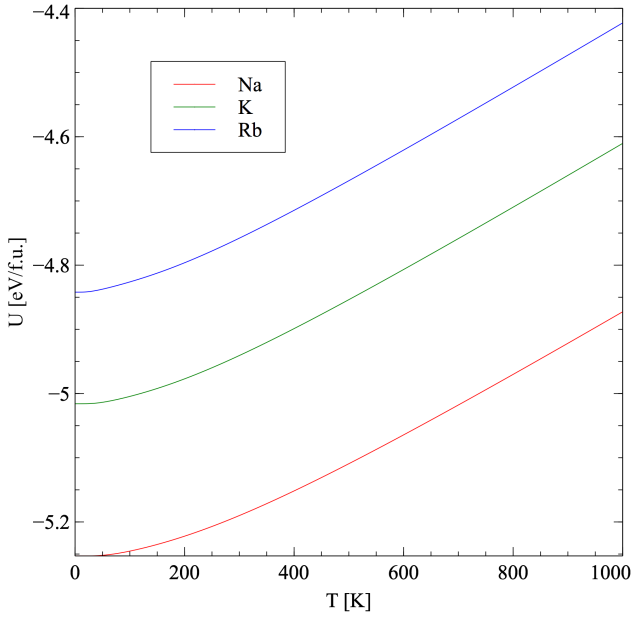


Figure 4.9. Internal energy of $MH_{31}OH$ for M = {Na, K and Rb}

The free energy of the solid solution is important to investigate the solid solubility of $OH^-$ in MH. Figure 4.10 shows the downhill functions of the free energy. The functions also start from the electronic ground state energy and the zero point energy and the heavier metals have higher free energy.

The entropy of 3.125% solid solution is shown in figure 4.11. The uphill functions with the increase of temperature go up from 0 at 0 K, which have higher values for heavier metals. Those thermodynamic functions for the solid solutions, metal hydrides and metal hydroxides can be applied to calculating the favorability of the solid solutions and investigating the further thermodynamic properties of the solid solutions.

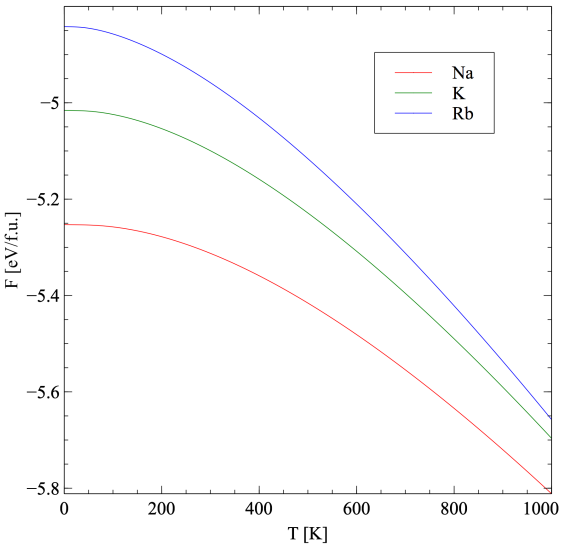


Figure 4.10. Free energy of $MH_{31}OH$ for M = {Na, K and Rb}.

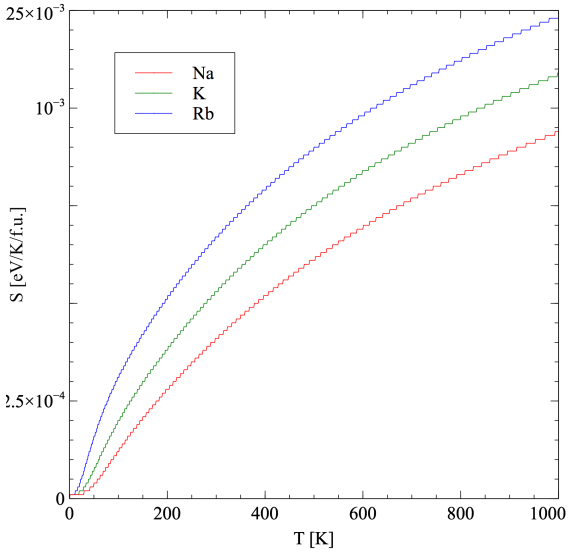


Figure 4.11. Entropy of $MH_{31}OH$ for M = {Na, K and Rb}.

## 4.7 SOLID SOLUTION FAVORABILITY

The solid solubility of $OH^-$ groups in MH is studied by the reaction as follows.

$$(1-x)\mathrm{MH} + x\mathrm{MOH} \rightarrow \mathrm{MH}_{(1-x)}(\mathrm{OH})_x \quad (4.1)$$

where $0 < x < 1$. The compound $\mathrm{MH}_{(1-x)}(\mathrm{OH})_x$ is favorable when the free energy, $F$, of the compound is less than the sum of the free energies of MOH and MH:

$$\Delta F = F\,[\mathrm{MH}_{(1-x)}(\mathrm{OH})_x] - x\,F(\mathrm{MOH}) - (1-x)\,F(\mathrm{MH}) < 0 \quad (4.2)$$

Figure 4.12 shows the free energy of 3.125% solid solution ($Li_{32}H_{31}OH$, red) and the free energy of the sum of the corresponding mixture of the separate LiH and LiOH phases (black). The separate phase curve is lower than the solid solution curve below 981 K (708 °C) indicating the separate phase is favorable below the critical temperature. The curves cross at 981 K. Therefore the solid solution becomes favorable above the temperature. However the separate phase decomposes into $Li_2O$ and $H_2$ predicted at 0 K regardless of the kinetic barrier to prevent the formation of the solid solution.

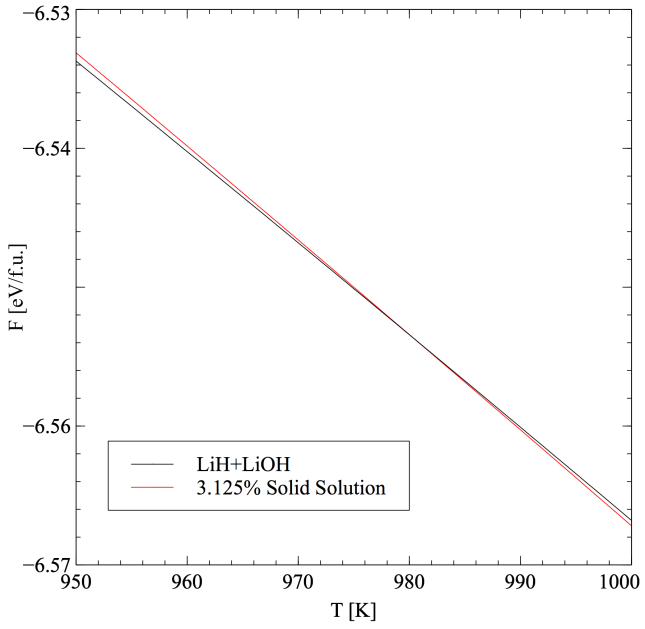


Figure 4.12. Free energy comparison between $Li_{32}H_{31}OH$ and 31LiH+LiOH.

The case of Na is plotted in figure 4.13. The curves cross at the critical temperature of 342 K (69 °C), below which the separate phase is favorable whereas

above which the solid solution $Na_{32}H_{31}OH$ becomes favorable. The solid solution indicates that the $OH^-$ groups are favorable in NaH structure, which may influence the thermodynamic properties of NaH or the relevant complex metal hydrides like $NaAlH_4$, such as the fact that the solid solution will decompose over 637 K (364 °C) to release hydrogen gas as follows instead of the decomposition of pure NaH into Na to release hydrogen gas at roughly the same temperature of 360 °C as predicted.

$$Na_{32}H_{31}OH \rightarrow Na_2O + 30Na + 16H_2 \quad (4.3)$$

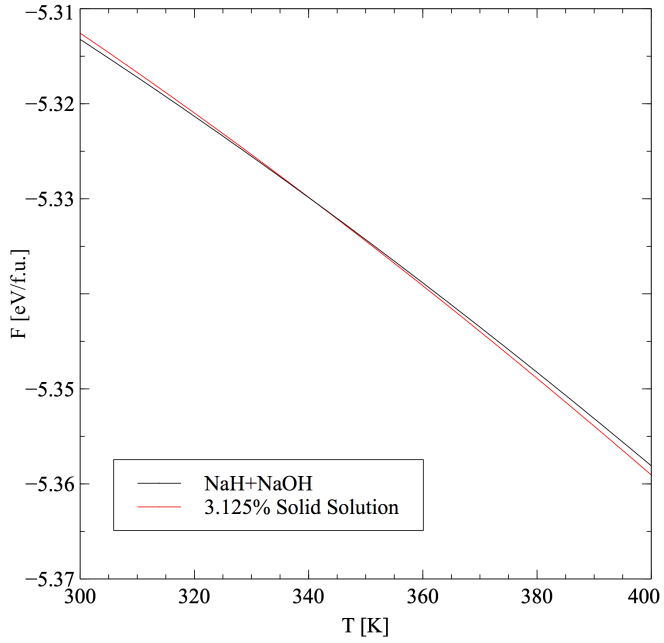


Figure 4.13. Free energy comparison between $Na_{32}H_{31}OH$ and 31NaH+NaOH.

Figure 4.14 shows the free energy of 3.125% of potassium solid solution ($K_{32}H_{31}OH$) and the corresponding sum of KH and KOH. The crossover takes place at 105 K (-168 °C), below which the separate phase is favorable whereas above which the solid solution begins to be favorable. The predicted temperature does not include the kinetic barrier so that the true critical temperature may be higher than the calculated temperature. The solid solution stabilizes KH from decomposition at the predicted decomposition temperature of the pure KH of 712 K (439 °C) to decompose at 738 K (465 °C) as follows.

$$2K_{32}H_{31}OH \rightarrow 2KOH + 62K + 31H_2 \quad (4.4)$$

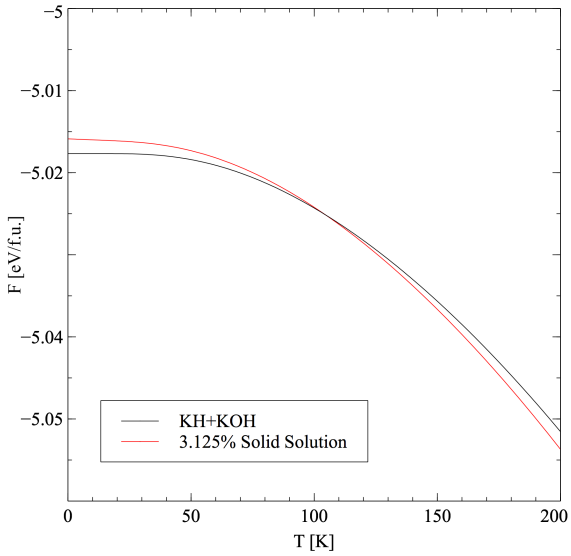


Figure 4.14. Free energy comparison between $K_{32}H_{31}OH$ and 31KH+KOH.

The case of Rb is similar to the case of K as shown in figure 4.15. The critical temperature is 166 K (-209 °C) lower than that of K. The $OH^-$ groups still stabilizes RbH from decomposition at the predicted temperature of 612 K (339 °C), whose decomposition temperature increases up to 634 K (361 °C) as follows.

$$2Rb_{32}H_{31}OH \rightarrow 2RbOH + 62\ Rb + 31H_2 \qquad (4.5)$$

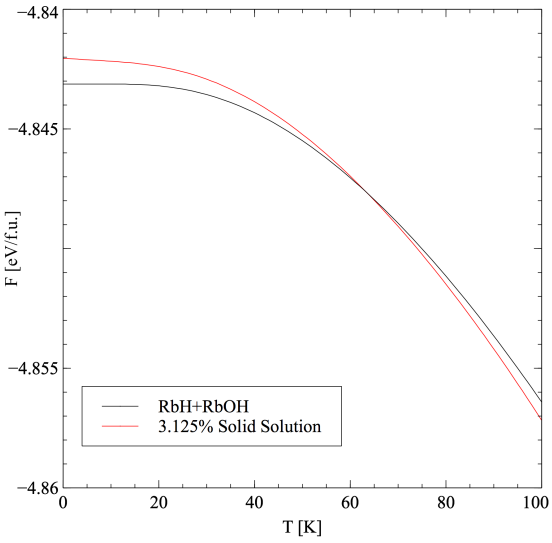


Figure 4.15. Free energy comparison between $Rb_{32}H_{31}OH$ and 31RbH+RbOH.

Figure 4.16 shows the free energy of 3.125% of Cs solid solution ($Cs_{32}H_{31}OH$) and the corresponding sum of CsH and CsOH. The downhill free energy of the separate phase is always lower than that of the solid solution and it goes down faster than the solid solution phase. Therefore the solid solution is always unfavorable.

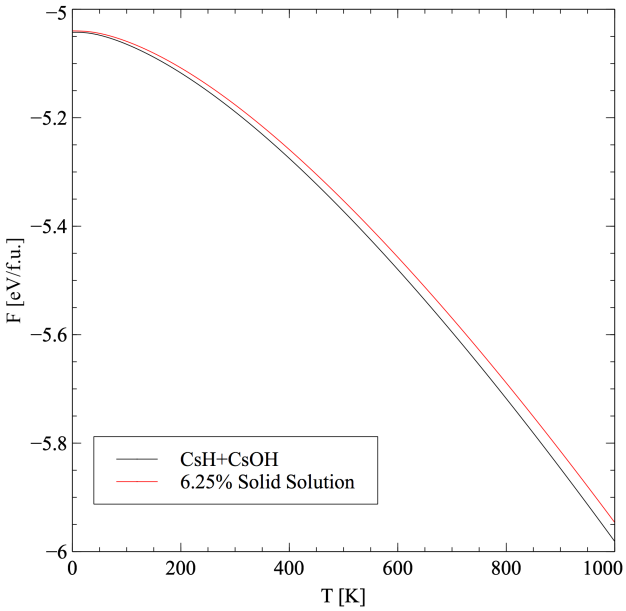


Figure 4.16. Free energy comparison between $Cs_{32}H_{31}OH$ and 31CsH+CsOH.

## 4.8 CONCLUSION

The comprehensive study of the solid solubility of MOH in MH reveals that LiH and CsH do not accommodate $OH^-$ groups in their crystals. Whereas NaH, KH and RbH are capable of mixing the corresponding metal hydroxides and the solubility increases with the increase of the atomic number, which is governed by the available volume difference for $H^-$ and $OH^-$ anions in the phases. MOH is able to be dissolved into MH when the volume difference is less than about 15%. $OH^-$ groups in NaH destabilize the crystal. However the groups stabilize RbH and CsH by increasing the decomposition temperatures. The predicted mixing critical temperatures are lower than the factual numbers partially due to failure to consider the kinetic barriers of the diffusion of $OH^-$ groups in MH crstals. The phase mismatch of MOH and MH may also be a factor that

can influence the mixing of MOH and MH but not be considered. The harmonic approximation does not consider the anharmonic terms that may cause some other complicated phenomena like crystal expansion, melting, phase transformation etc. Those complicated phenomena may also affect the real process of mixing, which should be investigated in future in order to understand more about the dynamics of the effects of the mixing so as to provide further guidance to the application of hydrogen storage materials.

# 5 DFT STUDY OF Mg TRANSITION METAL BORIDES/BOROHYDRIDES

## 5.1 INTRODUCTION

Magnesium borohydride [$Mg(BH_4)_2$] is one member of the light metal hydrides that are the candidates for the reversible hydrogen storage systems due to the high volumetric and gravimetric hydrogen capacities. The gravimetric hydrogen capacity of $Mg(BH_4)_2$ is about 14.9 wt%, starting to release hydrogen from 250 °C [61]. The ideal decomposition should generate $MgB_2$ and $H_2$. However it ususally produces some polyboron compounds like $MgB_{12}H_{12}$ that are too stable to release hydrogen further. Furthermore, $Mg(BH_4)_2$ has been obtained directly from $MgB_2$, which however requires high hydrogen pressure of 70 – 90 MPa. It has been shown that some transition metal borohydrides dehydride directly without the formation of some stable polyboron compounds [62]. Therefore it is suggested to add some transition metals (TM) to form $Mg_aTM_b(BH_4)_c$ so that it decomposes directly into the corresponding borides ($Mg_aTM_bB_c$) and releases hydrogen. The transion metals should be as light as possible so as to have the borohydrides retain high hydrogen capacity. Therefore the lighest transition metals from Sc to Ni were best considered. The first assignment is to try to find appropriate ternary borides ($Mg_aTM_bB_c$) where TM = {Sc, Ti, V, Cr, Mn, Fe, Co and Ni}, which have favorable stable structures.

## 5.2 SEARCH OF TERNARY BORIDES

The possible structures of magnesium ternary borides come out from the structures of a variety of teranry borides ($M_xM'_yB_z$). The magnesium ternary borides ($Mg_aTM_bB_c$) should be related to the corresponding magnesium transition metal borohydrides [$Mg_aTM_b(BH_4)_c$], in which Mg has the valence of +2 and the $[BH_4]^-$ ion contains the charge of -1. Therefore *a*, *b* and *c* satisfy $\frac{c-2a}{b} \in \{1, 2, 3, \dots\}$. From the rule, the *Pbam* structures of ternary borides of $MM'B_4$ and $M_2M'B_6$ were chosen to model the structures of magnesium ternary borides to form $MgTMB_4$ and $Mg_2TMB_6$ as shown in figure 5.1.

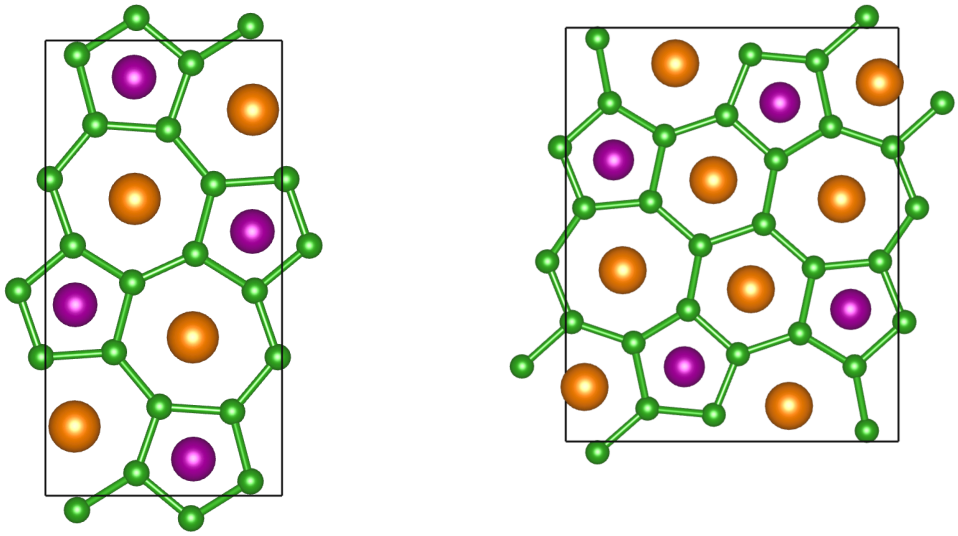

(a) (b)

Figure 5.1. Crystal structures of $MgTMB_4$ (a) and $Mg_2TMB_6$ (b) (Mg in yellow, TM in purple, B in green).

The corresponding borohydrides are $MgTM(BH_4)_4$ and $Mg_2TM(BH_4)_6$, where the valence of Mg and TM is +2.

## 5.3 COMPUTATIONAL METHODS

The next step is to check if the *Pbam* ternary borides are favorable in Mg-TM-B systems. In the Mg-TM-B system, all stable compounds such as Mg, $MgB_2$, TM, $TMB_x$, B, etc. are chosen to put together with $MgTMB_4$ and $MgTMB_6$ to compete by minimizing the total Gibbs free energy using GCLP algorithm to create the phase diagram of the system so as to check the favorable phases in the phase diagram.

## 5.4 Mg-Sc-B SYSTEM

The competing phases in Mg-Sc-B system are listed in table 5.1. Except the simple elements of Mg, B and Sc, the binary stable compounds are $MgB_2$, $ScB_2$, $ScB_6$ and $ScB_{12}$. $MgB_2$ and $ScB_2$ have the same structure of *P6/mmm* shown in the following figure 5.2.

Table 5.1. Competing phases in Mg-Sc-B system.

| Material | Symmetry | f.u. | *k*-points | E [eV/f.u.] | ZPE [eV/f.u.] |
|---|---|---|---|---|---|
| $MgB_2$ | *P6/mmm* | 1 | 16x16x16 | -15.38 | 0.18 |
| B | *R-3m* | 36 | 4x4x2 | -6.69 | 0.13 |
| Mg | *P-3m1* | 2 | 16x16x16 | -1.52 | 0.02 |
| Sc | $P6_3/mmc$ | 2 | 16x16x16 | -6.18 | 0.02 |
| $ScB_{12}$ | *Fm-3m* | 4 | 8x8x8 | -89.25 | 1.50 |
| $ScB_6$ | *P1* | 1 | 14x14x16 | -48.06 | 0.74 |
| $ScB_2$ | *P6/mmm* | 1 | 10x10x10 | -22.13 | 0.21 |
| $Mg_{26}ScB_{54}$ | *P1* | 1 | 2x2x2 | -422.11 | 7.28 |
| $Mg_{25}Sc_2B_{54}$ | *P1* | 1 | 2x2x2 | -428.81 | 7.26 |
| $Mg_{24}Sc_3B_{54}$ | *P1* | 1 | 2x2x2 | -435.45 | 7.20 |
| $Mg_{23}Sc_4B_{54}$ | *P1* | 1 | 2x2x2 | -442.29 | 7.21 |
| $Mg_{22}Sc_5B_{54}$ | *P1* | 1 | 2x2x2 | -449.18 | 7.23 |
| $MgScB_4$ | *Pbam* | 4 | 6x2x10 | -35.62 | 0.48 |
| $Mg_2ScB_6$ | *P1* | 4 | 4x2x10 | -51.08 | 0.74 |

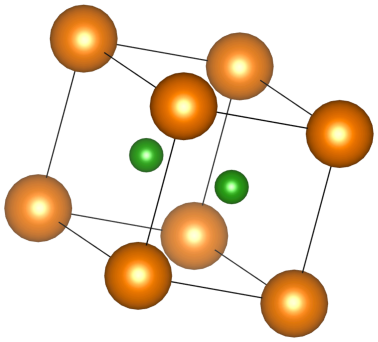

Figure 5.2. Crystal structure of $MB_2$ for M = {Mg, Sc} (M in gold, B in green).

The lattice constants of $MgB_2$ are 3.07 Å for **a** and **b** and 3.51 Å for **c**. The lattice constants of $ScB_2$ are 3.14 Å for **a** and **b** and 3.52 Å for **c**. The volume difference is only 4.5%. Therefore there might be solid solubility between $MgB_2$ and $ScB_2$. Hence a 3x3x3 supercell of $MgB_2$ is constructed to be $Mg_{27}B_{54}$ and substitute some Mg atoms for Sc atoms to form the solid solution crystal ($Mg_{26-n}Sc_nB_{54}$) as shown in figure 5.3.

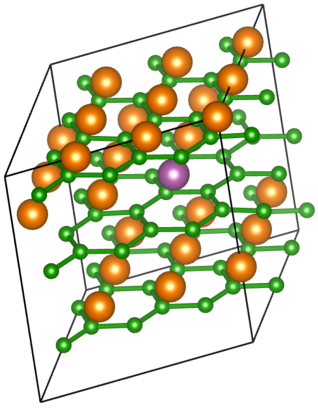

Figure 5.3. Crystal structure of $Mg_{26}ScB_{54}$ (Mg in gold, Sc in purple, B in green).

The solid solution structures at the Mg-rich side (n={1, 2, 3, 4, 5}) are also put into competition to see if the mixing will be favorable.

$ScB_6$ is also a stable structure for Sc-B system. The original structure of $ScB_6$ is a cubic crystal in the space group of $Pm\bar{3}m$. However the phonon results show that it contains 3 non-transitional imaginary modes of 4.11 THz indicating that the structure is unstable. The mode following method is applied to eliminate the non-transitional imaginary modes to find a symmetry-broken stable crytal structure as shown in figure 5.4.

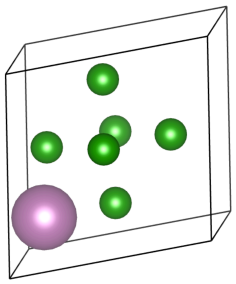

Figure 5.4. Crystal structure of $ScB_6$ (Sc in purple, B in green).

The cubic structure breaks its symmetry into $\boldsymbol{a} = \boldsymbol{b} = 4.12$ Å, $\boldsymbol{c} = 4.0$ Å and the angle $\gamma$ breaks into 79.6°. Sc-B system also has a boron rich structure of $ScB_{12}$, which is also a cubic structure with boron cage frames embedding Sc cations for the lattice constant of 7.4 Å as shown in figure 5.5.

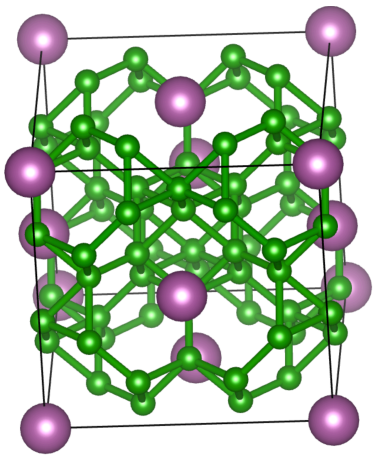

Figure 5.5. Crystal structure of $ScB_{12}$ (Sc in purple, B in green).

The crystal structures of all the phases listed in table 5.1 were optimized using VASP to obtain the electronic energies of the ground states as listed. The phonon frequencies were then calculated on the optimized crystals, from which the zero point energies (ZPE) could be acquired as listed in the table. The free energy of each crystal at a particular temperature was also achieved so as to put together to minimize the system's free energy to find the favorable phases by GCLP.

The calculated phase diagram for the competition phases were plotted in figure 5.6. The favorable phases are $MgB_2$ and $ScB_2$ below the phase transition temperature of 263 °C (solid black). The separate phases of $MgB_2$ and $ScB_2$ will mix into an 18.5 % solid solution of $Mg_{22}Sc_5B_{54}$ above the phase transition temperature. There is some residue $MgB_2$ for Sc < 18.5 %. All the separate phases were fully mixed at Sc = 18.5 % and there is some residue $ScB_2$ for Sc > 18.5 %. In the region where Sc < 18.5 %, the rest $MgB_2$ mixes the solid solution of $Mg_{22}Sc_5B_{54}$ to form 3.7 % of solid solution of $Mg_{26}ScB_{54}$ at 350 °C (solid red) so that the phases are 18.5% and 3.7% of solid solutions at high temperatures above 350 °C. In the region where Sc = 18.5 %, the 18.5 % solid solution is the only favorable phase above the phase transition temperature of 263 °C and there are some rest $ScB_2$ beside 18.5 % solid solution above the phase transition temperature of 263 °C in the region where Sc > 18.5 %.

From the phase diagram shows that there is no favorable ternary borides at low temperatures for Mg-Sc-B system.

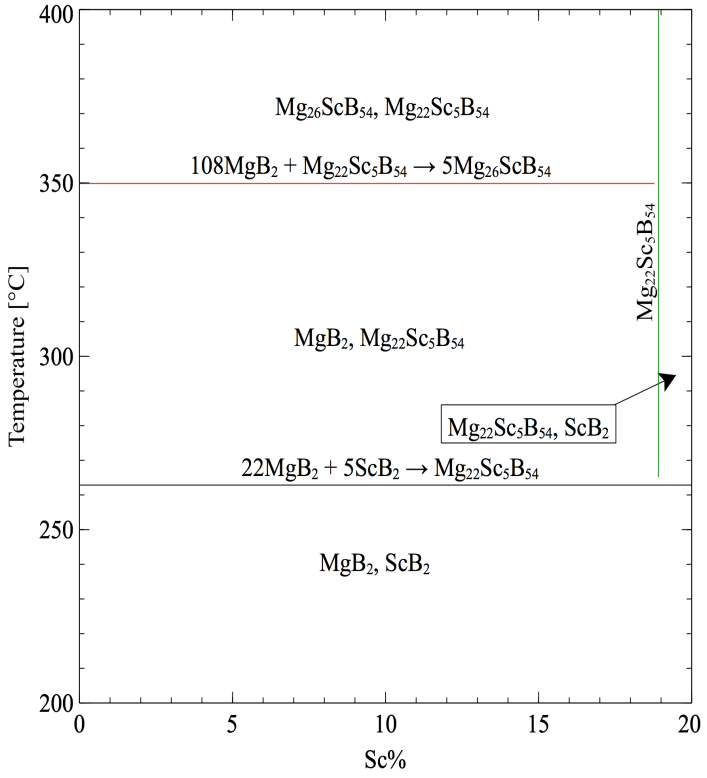


Figure 5.6. Phase diagram at Mg-rich side in Mg-Sc-B system.

## 5.5 Mg-Ti-B SYSTEM

Table 5.2 shows the competing phases in Mg-Ti-B system, in which the optimized symmetry, relaxation settings and the energy results are listed. The zero point energy (ZPE) is from the phonon results of the optimized structures. Besides the single elements, the diborides ($MgB_2$ and $TiB_2$) in *P6/mmm* structure as well as the derivative solid solutions of $Mg_{27-n}Ti_nB_{54}$ for $n \leq 5$, there are two special stable titanium borides of $Ti_3B_4$ and TiB. The *Pbam* ternary boride candidates are definitely put in competition.

The crystal structure of $Ti_3B_4$ is shown in figure 5.7 with the space group of *Immm* in orthorhombic crystal structure. The boron in the crystal forms 6-ring chains embedding titanium atoms. The optimized lattice constants are $\boldsymbol{a}$ = 3.26 Å, $\boldsymbol{b}$ = 13.73 Å, and $\boldsymbol{c}$ = 3.04 Å.

Table 5.2. Competing phases in Mg-Ti-B system.

| Material | Symmetry | f.u. | *k*-points | E [eV/f.u.] | ZPE [eV/f.u.] |
|---|---|---|---|---|---|
| $MgB_2$ | *P6/mmm* | 1 | 16x16x16 | -15.38 | 0.18 |
| B | *R-3m* | 36 | 4x4x2 | -6.69 | 0.13 |
| Mg | *P-3m1* | 2 | 16x16x16 | -1.52 | 0.02 |
| Ti | $P6_3/mmc$ | 2 | 16x16x10 | -7.74 | 0.01 |
| $TiB_2$ | *P6/mmm* | 1 | 10x10x10 | -24.23 | 0.24 |
| $Ti_3B_4$ | *Immm* | 2 | 14x2x16 | -56.38 | 0.57 |
| TiB | *Cmcm* | 4 | 12x4x14 | -16.05 | 0.14 |
| $Mg_{26}TiB_{54}$ | *P1* | 1 | 2x2x2 | -423.73 | 7.31 |
| $Mg_{25}Ti_2B_{54}$ | *P1* | 1 | 2x2x2 | -432.10 | 7.32 |
| $Mg_{24}Ti_3B_{54}$ | *P1* | 1 | 2x2x2 | -440.67 | 7.34 |
| $Mg_{23}Ti_4B_{54}$ | *P1* | 1 | 2x2x2 | -449.06 | 7.37 |
| $Mg_{22}Ti_5B_{54}$ | *P1* | 1 | 2x2x2 | -457.72 | 7.42 |
| $MgTiB_4$ | *Pbam* | 4 | 6x2x10 | -37.76 | 0.50 |
| $Mg_2TiB_6$ | *Pbam* | 4 | 4x2x12 | -53.24 | 0.78 |

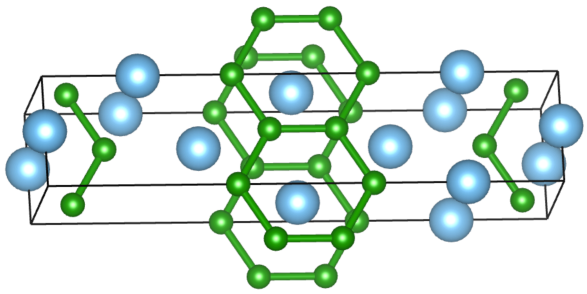

Figure 5.7. Crystal structure of $Ti_3B_4$ (Ti in blue, B in green).

Another stable titanium boride crystal structure is TiB of space group *Cmcm* also in orthorhombic crystal structure as shown in figure 5.8. The optimized lattice constants are ***a*** = 3.28 Å, ***b*** = 8.48 Å, and ***c*** = 3.05 Å. The boron atoms form boron chains with boron-boron bond length of 1.81 Å.

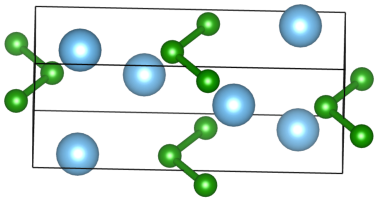

Figure 5.8. Crystal structure of TiB (Ti in blue, B in green).

The phonon calculation was performed on the relaxed crystal structures of all the phases listed in table 5.2. The electronic ground state energy and zero point energy (ZPE) derived from the phonon results were listed in table 5.2 also. The free energy could also be evaluated from the phonon frequencies in the harmonic approximation, which then could be applied to finding the favorable phases at a particular temperature to form the phase diagram as shown in figure 5.9.

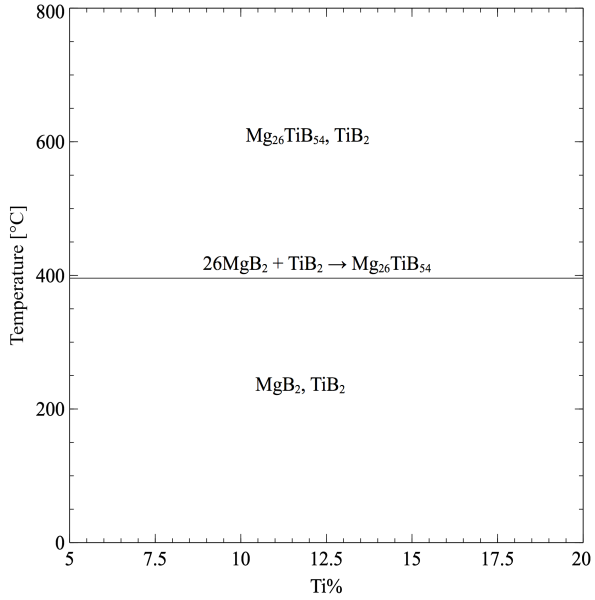


Figure 5.9. Phase diagram at Mg-rich side in Mg-Ti-B system.

$MgB_2$ and $TiB_2$ are separate favorable phases below the phase transition temperature of 396 °C (solid black), above which the separate phases are mixing into a 3.7 % of solid solution in the form of $Mg_{26}TiB_{54}$. All $MgB_2$ was consumed by $TiB_2$ to form the solid solution and there is some residue $TiB_2$ along with the solid solution. The

two phases constitute the high temperature phases in the phase diagram of Mg-Ti-B system.

From the phase diagram shows that there is no favorable ternary boride at low temperatures for Mg-Ti-B system.

## 5.6 Mg-V-B SYSTEM

The competing phases of Mg-V-B system are listed in table 5.3. There are many stable compounds in the vanadium boride system including $V_2B_3$, $V_3B_2$, $V_3B_4$ and VB besides *P*6/*mmm* $VB_2$. The solid solutions are created by substituting V atoms for some of Mg atoms in *P*6/*mmm* $VB_2$. The *Pbam* ternary borides will be put in competition with the stable compounds and single elements to check if they are favorable in the system by GCLP.

Table 5.3. Competing phases in Mg-V-B system.

| Material | Symmetry | f.u. | *k*-points | E [eV/f.u.] | ZPE [eV/f.u.] |
|---|---|---|---|---|---|
| $MgB_2$ | *P*6/*mmm* | 1 | 16x16x16 | -15.38 | 0.18 |
| B | *R*-3*m* | 36 | 4x4x2 | -6.69 | 0.13 |
| Mg | *P*-3*m*1 | 2 | 16x16x16 | -1.52 | 0.02 |
| $Mg_{26}VB_{54}$ | *P*1 | 1 | 2x2x2 | -424.06 | 7.36 |
| $Mg_{25}V_2B_{54}$ | *P*1 | 1 | 2x2x2 | -432.50 | 7.33 |
| $Mg_{24}V_3B_{54}$ | *P*1 | 1 | 2x2x2 | -441.19 | 7.35 |
| $Mg_{23}V_4B_{54}$ | *P*1 | 1 | 2x2x2 | -450.13 | 7.42 |
| $Mg_{22}V_5B_{54}$ | *P*1 | 1 | 2x2x2 | -459.32 | 7.52 |
| $Mg_2VB_6$ | *Pbam* | 4 | 4x2x12 | -54.22 | 0.80 |
| $MgVB_4$ | *Pbam* | 4 | 6x2x10 | -38.94 | 0.53 |
| V | *Im*-3*m* | 2 | 14x14x14 | -8.92 | 0.02 |
| $VB_2$ | *P*6/*mmm* | 1 | 10x10x10 | -24.44 | 0.23 |
| $V_2B_3$ | *Cmcm* | 4 | 18x2x18 | -41.77 | 0.44 |
| $V_3B_2$ | *P*4/*mbm* | 2 | 8x8x14 | -43.64 | 0.36 |

Table 5.3. Competing phases in Mg-V-B system (cont.).

| Material | Symmetry | f.u. | *k*-points | E [eV/f.u.] | ZPE [eV/f.u.] |
|---|---|---|---|---|---|
| $V_3B_4$ | *Immm* | 2 | 16x2x16 | -59.06 | 0.59 |
| VB | *Cmcm* | 4 | 12x4x14 | -17.24 | 0.15 |

The crystal of $V_2B_3$ is the space group of *Cmcm* in orthorhombic crystal structure with the constants of $\boldsymbol{a}$ = 3.04 Å, $\boldsymbol{b}$ = 18.40 Å, and $\boldsymbol{c}$ = 2.98 Å as shown in figure 5.10. Vanadium ions are embedded in the 6-ring chains of boron.

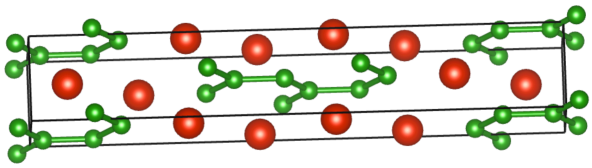

Figure 5.10. Crystal structure of $V_2B_3$ (V in red, B in green).

The crystal structure of $V_3B_2$ is shown in figure 5.11, which has the tetragonal structure with lattice constants of $\boldsymbol{a}$ = $\boldsymbol{b}$ = 5.71 Å and $\boldsymbol{c}$ =3.01 Å. The boron atoms in the crystal form boron-boron bond with the bond length of 1.78 Å.

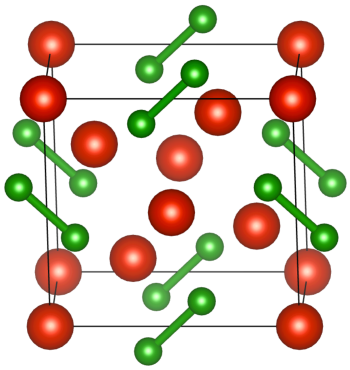

Figure 5.11. Crystal structure of $V_3B_2$ (V in red, B in green).

The crystal of $V_3B_4$ has the same crystal structure of $Ti_3B_4$ with space group of *Immm* as shown in figure 5.12. The lattice constants of the structure is $\boldsymbol{a}$ = 3.04 Å, $\boldsymbol{b}$ = 13.21 Å, and $\boldsymbol{c}$ = 2.97 Å, also similar to its partner $Ti_3B_4$. Boron atoms form the boron 6-ring chains.

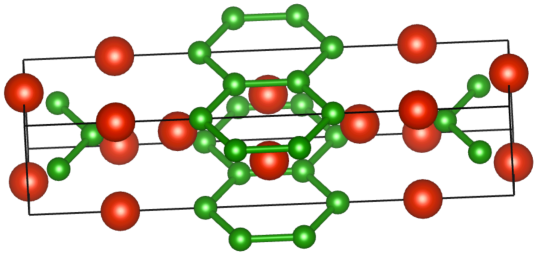

Figure 5.12. Crystal structure of $V_3B_4$ (V in red, B in green).

The last vanadium boride is VB as shown in figure 5.13, which has the identical crystal structure to TiB of *Cmcm* structure. It also has boron chains with a slightly shorter born length of 1.79 Å. The lattice constants are ***a*** = 3.05 Å, ***b*** = 8.03 Å and ***c*** = 2.96 Å.

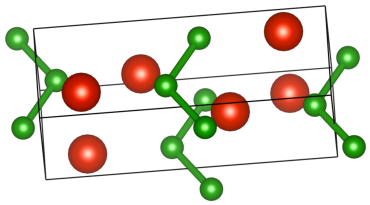

Figure 5.13. Crystal structure of VB (V in red, B in green).

The phonon calculation performed on the relaxed crystal structures of all the phases listed in table 5.3 could be applied to obtain the electronic ground state energy and zero point energy (ZPE). The free energies evaluated from the phonon frequencies in the harmonic approximation were applied to find the favorable phases at a particular temperature to form the phase diagram as shown in figure 5.14.

The phase diagram is similar to the Mg-Ti-B system, which shows $MgB_2$ and $VB_2$ are phase separate below the phase transition temperature of 390 °C (solid black), only 6 °C lower than that of Ti, above which the separate phases are mixing into a 3.7 % of solid solution of $Mg_{26}VB_{54}$ so that the two phases of the solid solution and the rest $MgB_2$ form the high temperature phases in the phase diagram of Mg-V-B system.

From the phase diagram shows that there is no favorable ternary borides at low temperatures for Mg-V-B system.

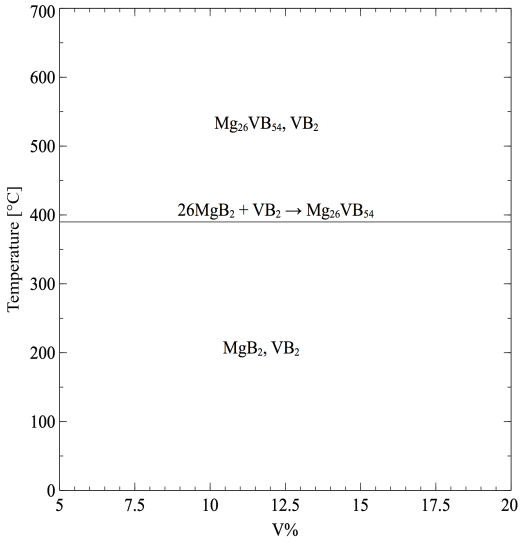


Figure 5.14. Phase diagram at Mg-rich side in Mg-V-B system.

## 5.7 Mg-Cr-B SYSTEM

The competing phases of Mg-Cr-B system with the symmetry of the crystals, the crystal formula units, the k-points, the relaxed electronic ground state energy and the zero point energy evaluated from the phonon results of the relaxed structures are listed in table 5.4. Beside those single elements, solid solutions, $MgB_2$ and $CrB_2$, there are some other chromium borides of $Cr_2B$, $Cr_3B_4$, $Cr_5B_3$, CrB, $CrB_4$ and $CrB_6$. In those chromium borides, $Cr_3B_4$ and CrB have the similar crystal structures to their corresponding vanadium borides of $V_3B_4$ and VB. The favorable phases are picked out from those competing phases by GCLP.

Table 5.4. Competing phases in Mg-Cr-B system.

| Material | Symmetry | f.u. | *k*-points | E [eV/f.u.] | ZPE [eV/f.u.] |
|---|---|---|---|---|---|
| $MgB_2$ | *P*6/*mmm* | 1 | 16x16x16 | -15.38 | 0.18 |
| Mg | *P*6$_3$/*mmc* | 2 | 16x16x16 | -1.52 | 0.02 |
| B | *R*-3*m* | 36 | 6x6x2 | -6.69 | 0.13 |
| $Mg_{26}CrB_{54}$ | *P*1 | 1 | 2x2x2 | -423.69 | 7.37 |
| $Mg_{25}Cr_2B_{54}$ | *P*1 | 1 | 2x2x2 | -431.66 | 7.36 |

Table 5.4. Competing phases in Mg-Cr-B system (cont.).

| Material | Symmetry | f.u. | *k*-points | E [eV/f.u.] | ZPE [eV/f.u.] |
|---|---|---|---|---|---|
| $Mg_{24}Cr_3B_{54}$ | *P*1 | 1 | 2x2x2 | -411.30 | 6.64 |
| $Mg_{23}Cr_4B_{54}$ | *P*1 | 1 | 2x2x2 | -448.69 | 7.49 |
| $Mg_{22}Cr_5B_{54}$ | *P*1 | 1 | 2x2x2 | -457.56 | 7.58 |
| $Mg_2CrB_6$ | *Pbam* | 4 | 4x2x12 | -54.3 | 0.81 |
| $MgCrB_4$ | *Pbam* | 4 | 6x2x10 | -39.26 | 0.55 |
| Cr | *Im*-3*m* | 2 | 16x16x16 | -9.46 | 0.02 |
| $CrB_2$ | *P*6/*mmm* | 1 | 10x10x10 | -23.75 | 0.22 |
| $Cr_2B$ | *Pm* | 4 | 8x8x10 | -26.68 | 0.19 |
| $Cr_3B_4$ | *Immm* | 2 | 16x2x16 | -58.22 | 0.57 |
| $Cr_5B_3$ | *I*4/*mcm* | 4 | 12x12x6 | -70.6 | 0.56 |
| CrB | *Cmcm* | 4 | 12x4x12 | -17.15 | 0.15 |
| $CrB_4$ | *Pm* | 2 | 4x4x8 | -37.7 | 0.48 |
| $CrB_6$ | *P*1 | 1 | 8x10x8 | -47.6 | 0.68 |

The crystal structure of $Cr_2B$ is monoclinic for the space group of *Pm* as shown in figure 5.15, where the boron atoms form boron-boron bond with the bond length of 1.97 Å. The boron-boron bonds are along ***c*** direction. The lattice constants are ***a*** = ***b*** = 5.12 Å and ***c*** = 4.28 Å, which indicates the crystal symmetry is very similar to tetragonal but the angle $\gamma$ has a tiny deviation from the right angle.

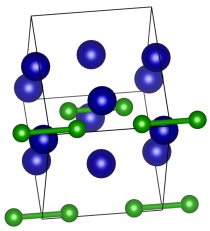

Figure 5.15. Crystal structure of $Cr_2B$ (Cr in blue, B in green).

The crystal of $Cr_5B_3$ is shown in figure 5.16 in the space group of *I*4/*mcm* for the structure of tetragonal with lattice constants of ***a*** = ***b*** = 5.12 Å and ***c*** = 4.28 Å. In the

crystal, all boron atoms form the boron-boron bond with the bond length of 1.80 Å except the boron atoms on the ***c*** axis between chromium ions, which are isolated boron ions.

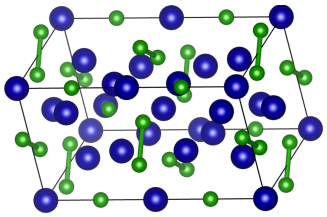

Figure 5.16. Crystal structure of $Cr_5B_3$ (Cr in blue, B in green).

Figure 5.17 shows the crystal structure of $CrB_4$ with space group of *Pm* in monoclinic symmetry. The lattice constants are ***a*** = 4.73 Å, ***b*** = 5.47 Å and ***c*** = 2.85 Å with tiny deviation of $\gamma$ from the right angle. The chromium ions are surrounded with boron cages.

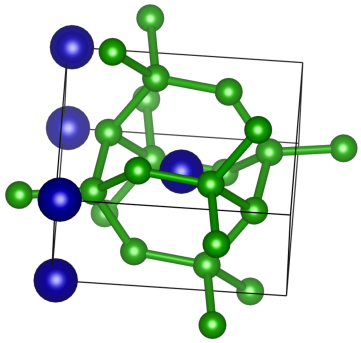

Figure 5.17. Crystal structure of $CrB_4$ (Cr in blue, B in green).

Figure 5.18 shows the mode-followed crystal structure of $CrB_6$ with symmetry broken from the original crystal structure of $Pm\bar{3}m$ in cubic structure that was unstable due to 3 non-transitional imaginary modes of 6.86 THz. The lattice parameters of the mode-followed crystal are ***a*** = ***c*** = 4.31 Å, ***b*** = 3.66 Å, $\boldsymbol{\alpha}$ = 76.54°, $\boldsymbol{\beta}$ = 75.68° and $\boldsymbol{\gamma}$ = 103.55°.

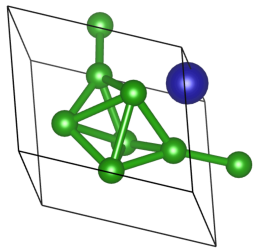

Figure 5.18. Crystal structure of $CrB_6$ (Cr in blue, B in green).

The phase diagram of Mg-Cr-B is calculated by competing all the possible phases in table 5.4 by minimizing the system's free energy using GCLP. The free energies are calculated from the phonon frequencies performed on the relaxed crystal structures of all the competing phases. From the phase diagram as shown in figure 5.19, the separate phases of $MgB_2$, CrB and $CrB_4$ constitute the low temperature phases in the phase diagram below 171 °C, where CrB and $CrB_4$ transits into $Cr_3B_4$ as plotted by dashed red line in the phase diagram. Therefore the phases contain $MgB_2$, $Cr_3B_4$ and the rest $CrB_4$, which then form the 3.7 % solid solution of $Mg_{26}CrB_{54}$ at the phase transition temperature of 392 °C marked as solid black line in the phase diagram so that the high temperature phase consists of the solid solution and the rest chromium borides of $Cr_3B_4$ and $CrB_4$.

Therefore, there are no favorable ternary borides at low temperatures for Mg-Cr-B system.

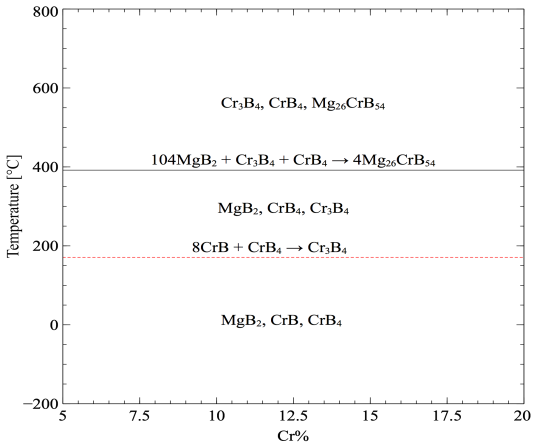


Figure 5.19. Phase diagram at Mg-rich side in Mg-Cr-B system.

## 5.8 Mg-Mn-B SYSTEM

The competing phases of Mg-Mn-B system are listed in table 5.5. Manganese borides consist of $MnB_2$, $Mn_2B$, $Mn_3B4$, MnB and $MnB_4$, in which $MnB_2$ is the same as other transition metal diborides in the space group of *P*6/*mmm* and $Mn_3B_4$ has also the same symmetry as $Cr_3B_4$. The solid solutions are created by substituting some Mg atoms for Mn atoms in the symmetry of *P*6/*mmm*. *Pbam* ternary boride candidates will compete with the common Mn borides.

Table 5.5. Competing phases in Mg-Mn-B system.

| Material | Symmetry | f.u. | *k*-points | E [eV/f.u.] | ZPE [eV/f.u.] |
|---|---|---|---|---|---|
| $MgB_2$ | *P*6/*mmm* | 1 | 16x16x16 | -15.38 | 0.18 |
| B | *R*-3*m* | 36 | 4x4x2 | -6.69 | 0.13 |
| Mg | *P*-3*m*1 | 2 | 16x16x16 | -1.52 | 0.02 |
| Mn | $P6_3/mmc$ | 2 | 16x16x16 | -1.11 | 0.01 |
| $MnB_2$ | *P*6/*mmm* | 1 | 16x16x16 | -22.73 | 0.21 |
| $Mn_2B$ | *I*4/*mcm* | 16 | 4x8x14 | -25.77 | 0.19 |
| $Mn_3B_4$ | *Immm* | 2 | 18x4x18 | -55.90 | 0.54 |
| MnB | *Pnma* | 4 | 8x16x10 | -16.42 | 0.15 |
| $MnB_4$ | $P2_1/c$ | 4 | 8x8x8 | -37.12 | 0.52 |
| $Mg_{26}MnB_{54}$ | *P*1 | 1 | 2x2x2 | -422.65 | 7.29 |
| $Mg_{25}Mn_2B_{54}$ | *P*1 | 1 | 2x2x2 | -430.38 | 7.38 |
| $Mg_{24}Mn_3B_{54}$ | *P*1 | 1 | 2x2x2 | -437.76 | 7.40 |
| $Mg_{23}Mn_4B_{54}$ | *P*1 | 1 | 2x2x2 | -445.55 | 7.46 |
| $Mg_{22}Mn_5B_{54}$ | *P*1 | 1 | 2x2x2 | -453.23 | 7.52 |
| $MgMnB_4$ | *Pbam* | 4 | 6x2x10 | -38.93 | 0.56 |
| $Mg_2MnB_6$ | *Pbam* | 4 | 4x2x12 | -54.00 | 0.81 |

The crystal structure of $Mn_2B$ is shown in figure 5.20 with the space group of *I*4/*mcm* in tetragonal structure. The lattice constants are $\boldsymbol{a} = \boldsymbol{b} = 5.06$ Å and $\boldsymbol{c} = 4.10$ Å. The boron atoms do not form bonding since they stay far away for the length of 2.05 Å.

The Mn atoms occupy the six vertices of the hexahedron and the boron atom occupies the center of the hexahedron.

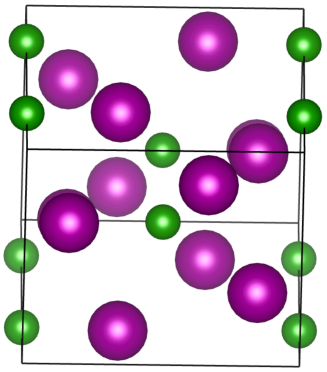

Figure 5.20. Crystal structure of $Mn_2B$ (Mn in purple, B in green).

The crystal structure of MnB in the space group of *Pnma* of orthorhombic structure is shown in figure 5.21. The lattice constants of the crystal are $\boldsymbol{a}$ = 5.54 Å, $\boldsymbol{b}$ = 2.84 Å and $\boldsymbol{c}$ = 4.09 Å. Each three atoms form a short chain with bond length of 1.75 Å.

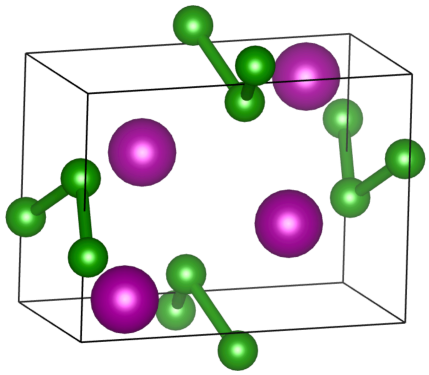

Figure 5.21. Crystal structure of MnB (Mn in purple, B in green).

The crystal structure of $MnB_4$ is shown in figure 5.22. The space group of the crystal is $P2_1/c$ in monoclinic with lattice constants of $\boldsymbol{a}$ = 5.89 Å, $\boldsymbol{b}$ = 5.35 Å and $\boldsymbol{c}$ = 5.48 Å together with the angle $\boldsymbol{\beta}$ = 122.86°. The boron atoms form boron-boron bonds with boron length of 1.69 Å along $\boldsymbol{b}$ axis.

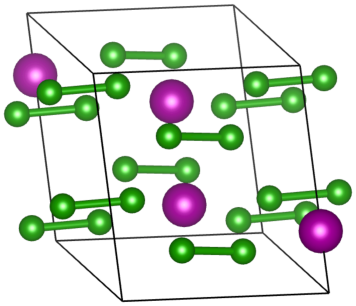

Figure 5.22. Crystal structure of $MnB_4$ (Mn in purple, B in green).

The competing phases shown in table 5.5 were optimized to put in the phonon calculations. The free energies were evaluated from the phonon results and put in to find the favorable phases in the phase diagram by GCLP.

The $MgB_2$ and the ternary boride $MgMnB_4$ beat over other candidates to show up in the low temperature region below 445 °C where the two phases merge into the 3.7% solid solution so that the high temperature region contains the solid solution and the rest $MgB_2$ as shown in figure 5.23.

In the Mg-Mn-B system, the ternary boride $MgMnB_4$ shows up as the favorable phase that can be a candidate for the further investigation of the corresponding borohydride.

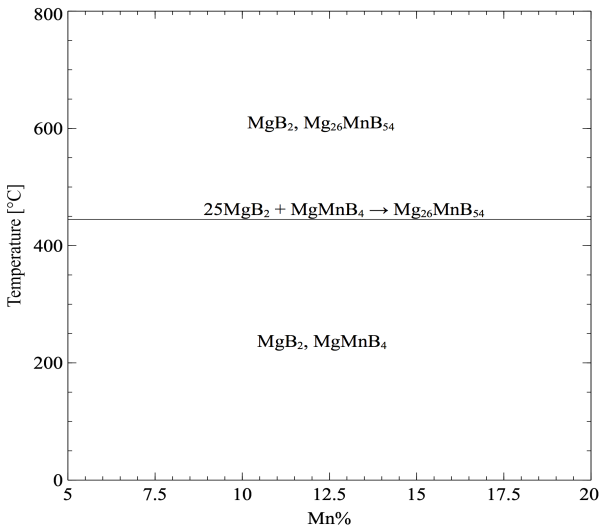


Figure 5.23. Phase diagram at Mg-rich side in Mg-Mn-B system.

## 5.9 Mg-Fe-B SYSTEM

Table 5.6 lists the competing phases of Mg-Fe-B system. The electronic ground state energy and zero point energy (ZPE) of the relaxed crystals are listed in the table. Iron borides consist of $Fe_2B$, $Fe_3B$ and FeB, in which $Fe_2B$ is the same as the structure of $Mn_2B$ and FeB has also the same symmetry as MnB. The solid solutions of Mg-Fe-B are also put into competition together with the *Pbam* ternary borides. The favorable phases will show up via GCLP.

Table 5.6. Competing phases in Mg-Fe-B system.

| Material | Symmetry | f.u. | *k*-points | E [eV/f.u.] | ZPE [eV/f.u.] |
|---|---|---|---|---|---|
| $MgB_2$ | *P*6/*mmm* | 1 | 16x16x16 | -15.38 | 0.18 |
| B | *R*-3*m* | 36 | 4x4x2 | -6.69 | 0.13 |
| Mg | *P*-3*m*1 | 2 | 16x16x16 | -1.52 | 0.02 |
| Fe | *P*4/*nmm* | 2 | 16x16x16 | -7.76 | 0.02 |
| $Fe_2B$ | *I*4/*mcm* | 4 | 14x14x16 | -23.68 | 0.16 |
| $Fe_3B$ | *Pnma* | 4 | 16x12x18 | -31.72 | 0.22 |
| FeB | *Pnma* | 4 | 12x20x16 | -15.51 | 0.14 |
| $Mg_{26}FeB_{54}$ | *P*1 | 1 | 2x2x2 | -421.96 | 7.33 |
| $Mg_{25}Fe_2B_{54}$ | *P*1 | 1 | 2x2x2 | -428.41 | 7.38 |
| $Mg_{24}Fe_3B_{54}$ | *P*1 | 1 | 2x2x2 | -434.86 | 7.44 |
| $Mg_{23}Fe_4B_{54}$ | *P*1 | 1 | 2x2x2 | -441.45 | 7.47 |
| $Mg_{22}Fe_5B_{54}$ | *P*1 | 1 | 2x2x2 | -447.89 | 7.48 |
| $MgFeB_4$ | *Pbam* | 4 | 6x2x10 | -38.00 | 0.55 |
| $Mg_2FeB_6$ | *Pbam* | 4 | 4x2x12 | -53.46 | 0.82 |

The crystal structure of $Fe_3B$ is shown in figure 5.24, which is the space group of *Pnma* in orthorhombic symmetry and the lattice constants are $\boldsymbol{a}$ = 5.11 Å, $\boldsymbol{b}$ = 6.59 Å and $\boldsymbol{c}$ = 4.34 Å. It is a boron poor binary boride. Hence the boron atoms are isolated among iron atoms. The distance of the closest boron atoms is 4.17 Å.

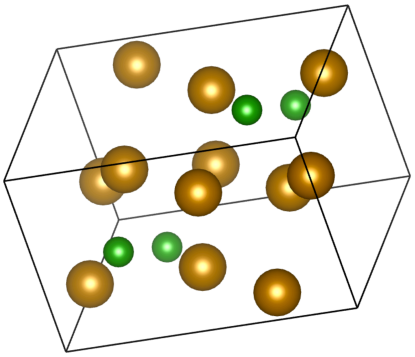

Figure 5.24. Crystal structure of $Fe_3B$ (Fe in gold, B in green).

The competing phases were put in competing the free energy to find the favorable phases in the phase diagram by phonon calculations in the harmonic approximation. The phase diagram is shown in figure 5.25.

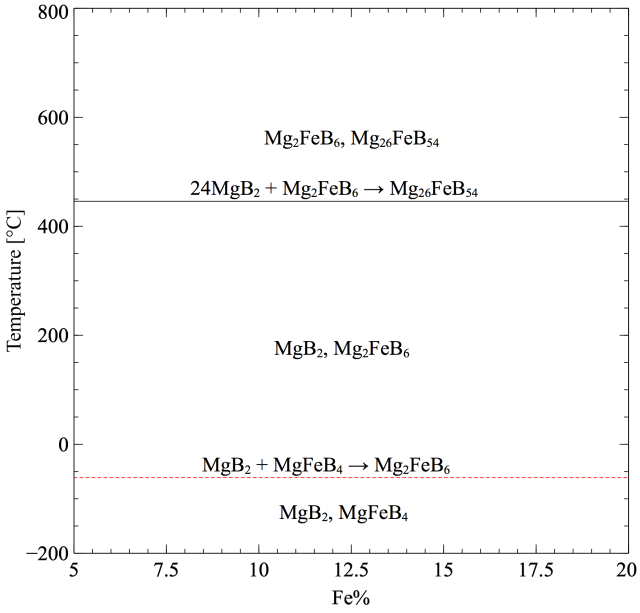


Figure 5.25. Phase diagram at Mg-rich side in Mg-Fe-B system.

The $MgB_2$ and the ternary boride $MgFeB_4$ constitute the low temperature region below -61 °C that is so low since the free energy only contains the harmonic part but not take account into the kinetic barrier that may increase the phase transition temperature. $MgFeB_4$ consumes some rest $MgB_2$ to form another ternary boride $Mg_2FeB_6$ at the transition temperature so that the phase region consists of $Mg_2FeB_6$ and the rest $MgB_2$

until 446 °C, where $Mg_2FeB_6$ consumes all rest $MgB_2$ to form the 3.7% solid solution constituting the high temperature region together with the rest $Mg_2FeB_6$.

In the Mg-Fe-B system, the ternary boride $MgFeB_4$ and $Mg_2FeB_6$ are favorable throughout the entire phase diagram, in which $MgFeB_4$ is the low temperature phase that should be stable in the Mg-Fe-B system. The corresponding borohydride of $MgFe(BH_4)_4$ is expected to decompose into the stable boride and releases hydrogen.

## 5.10 Mg-Co-B SYSTEM

Cobalt is in the same group as that of iron. Therefore the binary borides of Co-B system are the same as that of iron with CoB, $Co_2B$ and $Co_3B$ with the same crystal structures as the corresponding iron borides. The competing phases are shown in table 5.7.

Table 5.7. Competing phases in Mg-Co-B system.

| Material | Symmetry | f.u. | *k*-points | E [eV/f.u.] | ZPE [eV/f.u.] |
|---|---|---|---|---|---|
| $MgB_2$ | *P*6/*mmm* | 1 | 16x16x16 | -15.38 | 0.18 |
| B | *R*-3*m* | 36 | 4x4x2 | -6.69 | 0.13 |
| Mg | *P*-3*m*1 | 2 | 16x16x16 | -1.52 | 0.02 |
| $Mg_{26}CoB_{54}$ | *P*1 | 1 | 2x2x2 | -420.40 | 7.30 |
| $Mg_{25}Co_2B_{54}$ | *P*1 | 1 | 2x2x2 | -425.54 | 7.33 |
| $Mg_{24}Co_3B_{54}$ | *P*1 | 3 | 2x2x2 | -430.28 | 7.29 |
| $Mg_{23}Co_4B_{54}$ | *P*1 | 1 | 2x2x2 | -435.08 | 7.28 |
| $Mg_{22}Co_5B_{54}$ | *P*1 | 1 | 2x2x2 | -439.55 | 7.19 |
| $Mg_2CoB_6$ | *Pbam* | 4 | 4x2x12 | -52.28 | 0.83 |
| $MgCoB_4$ | *Pbam* | 4 | 6x2x10 | -36.73 | 0.54 |
| Co | $P6_3/mmc$ | 2 | 16x16x10 | -6.80 | 0.02 |
| CoB | *Pnma* | 4 | 6x12x10 | -14.47 | 0.14 |
| $Co_2B$ | *I*4/*mcm* | 4 | 8x8x10 | -21.26 | 0.16 |
| $Co_3B$ | *Pnma* | 4 | 10x8x12 | -28.10 | 0.21 |

The phase diagram of Mg-Co-B system is similar to that of Mg-Fe-B system except the fact that $MgCoB_4$ does not show up in the phase diagram as shown in figure 5.26. The low temperature region is composed of $MgB_2$ and the ternary boride $Mg_2CoB_6$ that consumes all the $MgB_2$ to form the 3.7% solid solution of $Mg_{26}CoB_{54}$ at the critical temperature of 479 °C (black line in figure 5.26). $Mg_2CoB_6$ and the solid solution constitute the high temperature phase region.

Therefore $Mg_2CoB_6$ is the ternary boride favorable in the low temperature region, which may have the derivative borohydride of $Mg_2Co(BH_4)_6$ that could decompose directly into the ternary boride without formation of any polyboron hydrides.

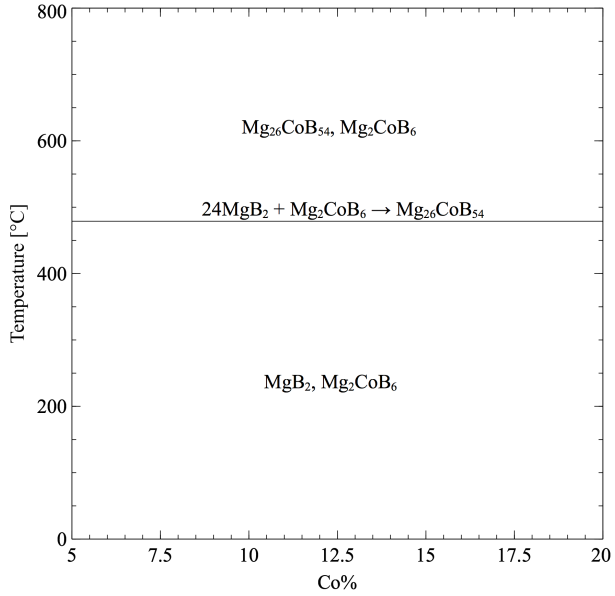


Figure 5.26. Phase diagram at Mg-rich side in Mg-Co-B system.

## 5.11 Mg-Ni-B SYSTEM

Nickel is also in the same group as that of iron. Therefore the binary borides of Ni-B system are similar to that of iron with $Ni_2B$ and $Ni_3B$ with the same crystal structures as the corresponding iron borides. The crystal structure of NiB is in the space group of *Cmcm* of orthorhombic structure the same as that of CrB. $Ni_4B_3$ is the unique favorable structure in Ni-B structure as shown in table 5.8. The solid solutions in Mg-N-B system are still the structure of the solid solution in Mg-Fe-B system by substituting Ni

atoms for Fe atoms. The *Pbam* ternary borides are made by substituting Ni atoms for Fe atoms in *Pbam* ternary borides in Mg-Fe-B system. The Mg-Ni-B system is expected to have the similar properties to that of the Mg-Fe-B system since the elements are in the same group.

Table 5.8. Competing phases in Mg-Ni-B system.

| Material | Symmetry | f.u. | *k*-points | E [eV/f.u.] | ZPE [eV/f.u.] |
|---|---|---|---|---|---|
| $MgB_2$ | *P*6/*mmm* | 1 | 16x16x16 | -15.38 | 0.18 |
| B | *R*-3*m* | 36 | 4x4x2 | -6.69 | 0.13 |
| Mg | *P*-3*m*1 | 2 | 16x16x16 | -1.52 | 0.02 |
| $Mg_{26}NiB_{54}$ | *P*1 | 1 | 2x2x2 | -418.67 | 7.30 |
| $Mg_{25}Ni_2B_{54}$ | *P*1 | 1 | 2x2x2 | -421.79 | 7.26 |
| $Mg_{24}Ni_3B_{54}$ | *P*1 | 3 | 2x2x2 | -424.62 | 7.14 |
| $Mg_{23}Ni_4B_{54}$ | *P*1 | 1 | 2x2x2 | -427.67 | 7.09 |
| $Mg_{22}Ni_5B_{54}$ | *P*1 | 1 | 2x2x2 | -430.53 | 7.04 |
| $Mg_2NiB_6$ | *Pbam* | 4 | 4x2x12 | -50.20 | 0.78 |
| $MgNiB_4$ | *Pbam* | 4 | 6x2x10 | -34.66 | 0.50 |
| Ni | *Fm*-3*m* | 4 | 10x10x10 | -5.40 | 0.03 |
| NiB | *Cmcm* | 4 | 12x4x12 | -12.60 | 0.13 |
| $Ni_2B$ | *I*4/*mcm* | 4 | 8x8x10 | -18.45 | 0.15 |
| $Ni_3B$ | *Pnma* | 4 | 10x8x12 | -24.12 | 0.20 |
| $Ni_4B_3$ | *C*2/*c* | 4 | 8x12x6 | -43.78 | 0.43 |

Figure 5.27 shows the crystal structure of $Ni_4B_3$ in the space group of *C*2/*c* of monoclinic structure with the lattice constants of $\boldsymbol{a}$ = 6.37 Å, $\boldsymbol{b}$ = 4.91 Å, $\boldsymbol{c}$ = 7.87 Å and $\beta$ = 102.12°. Each three boron atoms form a straight chain with the bond length of 1.87 Å.

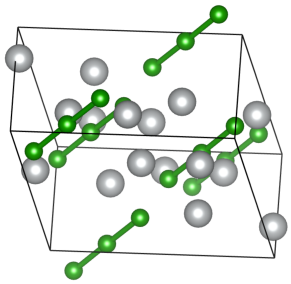

Figure 5.27. Crystal structure of $Ni_4B_3$ (Ni in grey, B in green).

The phase diagram of Mg-Ni-B system is shown in figure 5.28 calculated from the GCLP minimization of the competing phases. The low temperature region is composed of $MgB_2$, pure boron and $Ni_4B_3$ until the calculated phase transition temperature of -77 °C (red dashed line) where those phases merge into the ternary boride of $Mg_2NiB_6$. $MgB_2$ consumes all boron and $Ni_4B_3$ so that the high temperature region constitutes $MgB_2$ and $Mg_2NiB_6$ that then consumes the rest $MgB_2$ to form the 3.7% solid solution of $Mg_{26}NiB_{54}$ at 441 °C (black solid line). Thus the solid solution and the ternary boride of $Mg_2NiB_6$ form the high temperature phase above 441 °C.

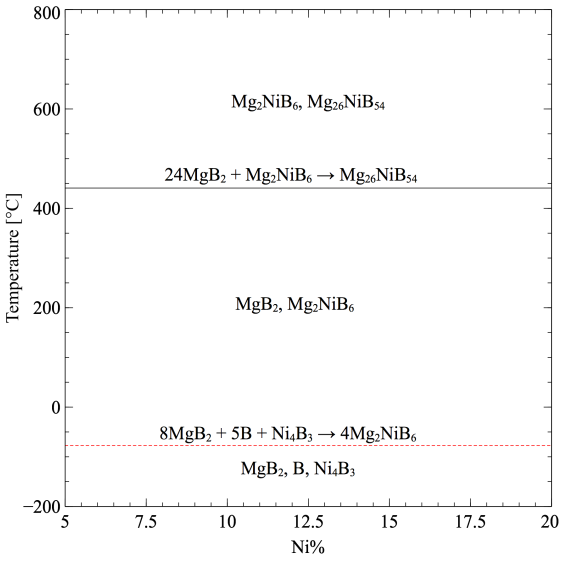


Figure 5.28. Phase diagram at Mg-rich side in Mg-Ni-B system.

From the phase diagram, the ternary boride $Mg_2NiB_6$ appears in the relatively high temperature region. There may be no applicable ternary boride as the further candidate.

## 5.12 PEGS SEARCH OF Mg-TM-$BH_4$ SYSTEMS

The investigations of Mg-TM-B system for TM = {Sc, Ti, V, Cr, Mn, Fe, Co, Ni} show that the *Pbam* ternary borides may be favorable at low temperatures for TM = {Mn, Fe, Co, Ni} summarized in table 5.9.

Table 5.9. Favorable *Pbam* magnesium transition metal ternary borides.

| TM | Favorable Ternary Borides | TM | Favorable Ternary Borides |
|---|---|---|---|
| Mn | $MgMnB_4$ | Co | $Mg_2CoB_6$ |
| Fe | $MgFeB_4$, $Mg_2FeB_6$ | Ni | $Mg_2NiB_6$ |

The favorable phases of the corresponding borohydrides for those favorable ternary borides in the forms of $MgTM(BH_4)_4$ for TM = {Mn and Fe} and $Mg_2TM(BH_4)_6$ for TM = {Fe, Co, Ni} fall in the consideration. However there have not been any such ternary borohydrides found by literature. Therefore the PEGS algorithm that searches possible structures by minimizing the ionic energy function using simulated annealing algorithm is applied. The possible structures of $MgMn(BH_4)_4$ and $Mg_2Mn(BH_4)_6$ are shown in figure 5.29 (a) and (b) respectively.

(a) (b)

Figure 5.29. PEGS structures of $MgMn(BH_4)_4$ (a) and $Mg_2Mn(BH_4)_6$ (b), (Mg in gold, Mn in purple, B in green, H in white).

The PEGS structures have no symmetry. The other ternary borides for TM = {Fe, Co, Ni} are made by substituting Mn atoms for the certain TM atoms, which are then relaxed by VASP. Those hypothetical structures are used to check the decomposition properties.

## 5.13 DIRECT DECOMPOSITIONS OF $MgTM(BH_4)_4$ AND $Mg_2TM(BH_4)_6$

The desired decompositions of the magnesium borohydrides are to investigate their direct releases of hydrogen without any byproducts as follows.

$$MgTM(BH_4)_4 \rightarrow MgTMB_4 + 8H_2 \text{ for TM = \{Mn and Fe\}} \quad (5.1)$$

$$Mg_2TM(BH_4)_6 \rightarrow Mg_2TMB_6 + 12H_2 \text{ for TM = \{Fe, Co and Ni\}} \quad (5.2)$$

The direct decompositions by reactions (5.1) and (5.2) for them at the room temperature of 27 °C is going to be investigated.

Table 5.10 shows the enthalpies of the decompositions of the magnesium transition metal borohydrides into the corresponding borides and hydrogen for equations (5.1) and (5.2) at the room temperature of 27 °C. The values are similar ranging from 34.4 kJ/mol $H_2$ to 35.6 kJ/mol $H_2$. The positive values indicate the decompositions are endothermic reactions.

Table 5.10 Enthalpies of direct decompositions of magnesium borohydrides at 27 °C.

| Borohydride | $\Delta H$ [kJ/mol $H_2$] |
|---|---|
| $MgMn(BH_4)_4$ | 35.6 |
| $MgFe(BH_4)_4$ | 35.3 |
| $Mg_2Fe(BH_4)_6$ | 34.9 |
| $Mg_2Co(BH_4)_6$ | 34.7 |
| $Mg_2Ni(BH_4)_6$ | 34.4 |

## 5.14 CONCLUSION

The magnesium transition metal borohydrides and borides are theoretically studied by differential functional theory (DFT) method. The favorability of magnesium

transition metal borides was investigated and some favorable *Pbam* structures of the ternary borides are predicted. The structures of the corresponding borohydrides were also predicted by PEGS algorithm so that the favorite direct decompositions of the borohydrides were investigated to find appropriate decomposition enthalpies. However those PEGS structures of the borohydrides are theoretical predictions that have not been reported in experiments. The direct decompositions are also hypothetical reactions having not been verified by experiments. Therefore it needs further experimental investigations of the borohydrides and borides to verify and improve the theoretical predictions.

# PAPER

## I. STUDY OF THE HEAT AND PRESSURE-INDUCED S105 PHASE IN $NaAlH_4$

David Peaslee[a], Gang Wang[a], Dongxue Zhao[a], Eric Sorte[b], Sophia Hayes[c], Mark Conradi[b], Bob Bowman[d], and Eric Majzoub[a]

[a]Center for Nanoscience and Department of Physics and Astronomy, University of Missouri-St. Louis

[b]Department of Physics Washington University

[c]Department of Chemistry Washington University

[d]Oak Ridge National Laboratory

### INTRODUCTION

Hydrogen is an efficient and pollution-free energy carrier. The current barrier of entry for hydrogen in the energy market is a low cost and reliable storage method. Complex anionic hydrides such as sodium aluminum hydride ($NaAlH_4$) are promising storage materials due to their high hydrogen storage capacities (about 5-6 wt.%), and reasonable reaction temperatures (around 100 °C using a catalyst).

This paper presents a study of the decomposition of a high purity bulk $NaAlH_4$ (crystal structure shown in Figure 3.1) with a new phase created under a high hydrogen pressure (200 bar) and high temperature (near 180 °C). Recent NMR studies have found a highly mobile Al-species (the "S105 phase") in heat and pressure-treated $NaAlH_4$ [1, 2]. By studying the decomposition pathways with a high temperature direct line-of-sight mass spectrum residual gas analyzer (MS-RGA), approximation can be made on the decomposition energy and reaction rates of the bulk material. Figure 1 shows the $NaAlH_4$ unit cell structure:

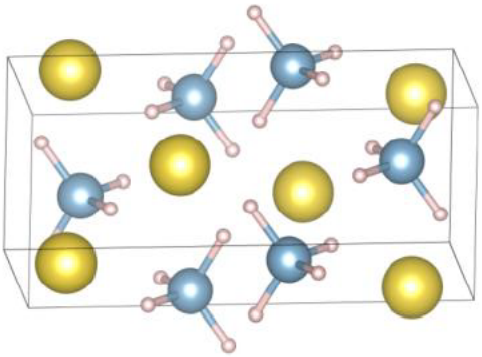

Figure 1. GSAS crystal structure representation of $NaAlH_4$ [3].

## EXPERIMENTAL SECTION

Figure 2 shows how the high purity bulk $NaAlH_4$ crystals were synthesized using the evaporation crystallization method. Three samples have been created to determine some of the properties of this phase:

- Pure $NaAlH_4$: synthesized in lab.
- N97 (no S105): Heated to just below melting temperature under high $H_2$ pressure.
- N98 (S105): Heated to just above melting temperature under high $H_2$ pressure.

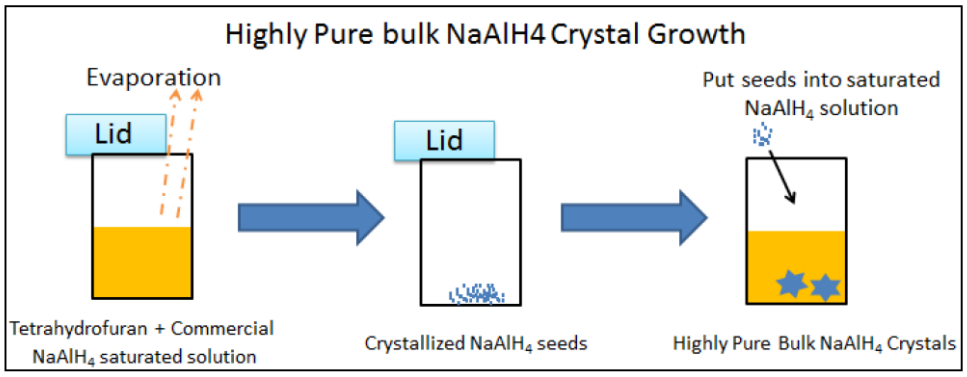


Figure 2. Preparation and crystal growth of high purity $NaAlH_4$.

Powder X-ray diffraction (XRD) was performed on a Rigaku Ultima IV X-ray diffraction (XRD) system with Cu Kα radiation. The XRD data is analyzed using the Rietveld refinement method. The refined pattern with optimized structure is shown in Figure 3. The criterion of the refinement fit is determined by whole pattern residuals (*Rp*) and weighted residuals (*wRp*).

$$Rp = \frac{\sum | I_0 - I_c |}{\sum I_0} \quad (1)$$

$$wRp = \frac{\sum w \cdot | I_0 - I_c |^2}{\sum w \cdot {I_0}^2} \quad (2)$$

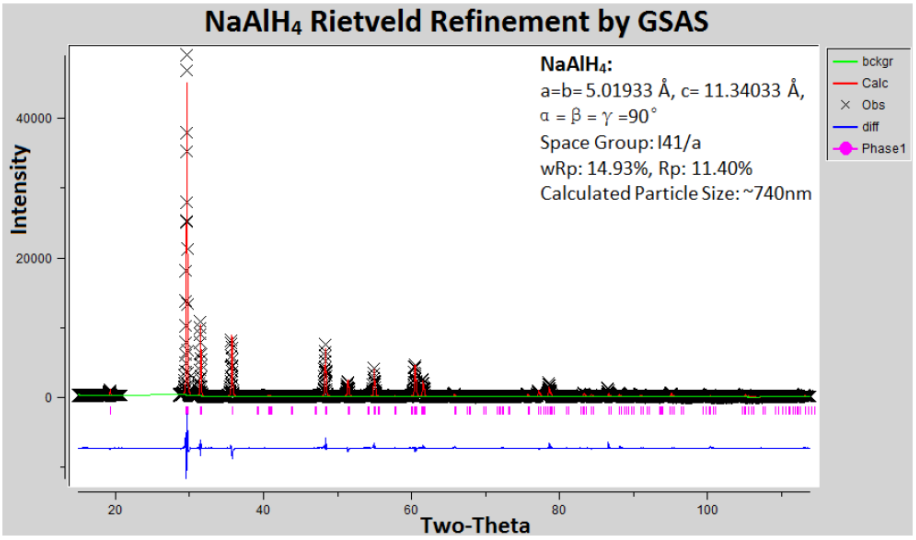


Figure 3. Rietveld refined X-ray diffraction pattern.

Here $I_O$ is the XRD observed intensity, and $I_C$ is the calculated intensity. The calculated particle sizes range is given by the Debye–Scherrer equation (3).

$$D = 0.94 \times \frac{\lambda}{FWHM \cdot \cos\theta} \quad (3)$$

It can be clearly seen that the pattern is well fitted with optimized structure constants by the whole pattern Rietveld refinement method. From Figure 3, *wRp* is 14.93, *Rp* is 11.40%, and the calculated coherence length is 740 nm.

## RESULTS AND DISCUSSION

The First Principles Study of the Decomposition of $NaAlH_4$. $NaAlH_4$ decomposes by 3 steps:

$$NaAlH_4 \rightarrow \frac{1}{3} Na_3AlH_6 + \frac{2}{3} Al + H_2 \quad \text{(Reaction 1)} \quad (4)$$

$$Na_3AlH_6 \rightarrow 3NaH + Al + \frac{3}{2} H_2 \quad \text{(Reaction 2)} \quad (5)$$

$$NaH \rightarrow Na + \frac{1}{2} H_2 \text{ (Reaction 3)} \quad (6)$$

Experimentally, the 3 decomposition steps occur in bulk material at 230, 265 and 660 °C [4]. By first-principles calculations of the thermodynamic free energy, at 1 atm of $H_2$ and ignoring kinetic barriers, they occur at -50.1, -19.15 and 591.85 °C. Details are shown in Table 1.

Table 1. Theoretical and Experimental Enthalpies at 1 atm.

| | $\Delta H$ [4] | | $\Delta H$ (calc.) | | $\Delta H$ (exp.) | |
|---|---|---|---|---|---|---|
| | °C | kJ/mol $H_2$ | °C | kJ/mol $H_2$ | °C | kJ/mol $H_2$ |
| Reaction 1 | 230 | 25 | -50 | 23 | 249.5 | 52.6 |
| Reaction 2 | 265 | 39 | -19 | 37 | | |
| Reaction 3 | 660 | 76 | 592 | 78 | 434.41 | 66.3 |

The melting temperature of $NaAlH_4$ was about 183 °C, and its experimental heat of fusion was 1.5 kJ/mol. The calculated enthalpy of the first two reactions are 64 kJ/mol $H_2$, which is greater than the experimental value of about 52.6 kJ/mol $H_2$. The difference may be caused by the crystallization of $Na_3AlH_6$, from molten $NaAlH_4$, when the first decomposition proceeds to produce $Na_3AlH_6$, which has a melting temperature of 252 °C.

The reacting enthalpies are shown in Figure 4(a). They show the same trend as the experimental enthalpies show. They increase at the beginning, reach a peak and then decrease with the increase of temperature.

The phase diagram (pressure vs. temperature) has also been investigated as illustrated in Figure 4(b). The black, red and green boundaries clearly mark the edges of the three phase regions. In the first region, there is only $NaAlH_4$. In the second region, $NaAlH_4$ decomposes into $Na_3AlH_6$ and Al to release $H_2$. The temperature of the phase boundaries increases with the increase of $H_2$ pressure.

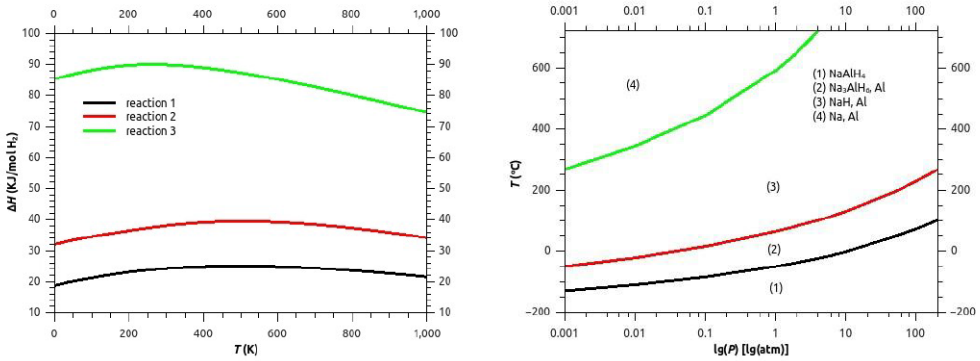


Figure 4 (Left). The calculated reaction enthalpies as a function of temperature. (Right). The phase diagram of $NaAlH_4$.

Oxidized $NaAlH_4$ was also investigated using supercell first-principles calculations. $[AlH_4]^-$ was replaced with $OH^-$ to inspect the solubility of NaOH in $NaAlH_4$, which can be determined by the difference of free energy between $(NaAlH_4)_{(1-x)}(NaOH)_x$ and $NaAlH_4$+NaOH by the equation:

$$\Delta F = F\left[(NaAlH_4)_{(1-x)}(NaOH)_x\right] - (1-x)F(NaAlH_4) - xF(NaOH) \qquad (7)$$

Figure 5(a) illustrates the calculated free energies of $(NaAlH_4)_{(1-x)}(NaOH)_x$. This clearly shows that the free energy increases with the increase of NaOH concentration up to the free energy of NaOH. The changes of free energies can be deduced from the data as shown in Figure 5(b). Within the temperature zone $0 < T < 1000$ K, the changes of the free energies gradually decrease, becoming favorable. The exception is for $x = 0.4375$, which becomes favorable beyond 1000 K. This data clearly indicates that NaOH is soluble in $NaAlH_4$ over a wide composition range.

Figure 6(a) was derived from the changes of free energies of $(NaAlH_4)_{(1-x)}(NaOH)_x$ at the points $\Delta F$ just below 0, which illustrate the saturated concentrations of NaOH in $NaAlH_4$ at various temperatures. Furthermore, the solubility occurs above 650 K (400 °C). However, $NaAlH_4$ decomposes before this temperature, which implies that NaOH cannot dissolve into $NaAlH_4$ at 1 atm. The solubility might be observed at high $H_2$

overpressures where $NaAlH_4$ is prevented from decomposing. The solution enthalpies of $(NaAlH_4)_{(1-x)}(NaOH)_x$ have also been investigated.

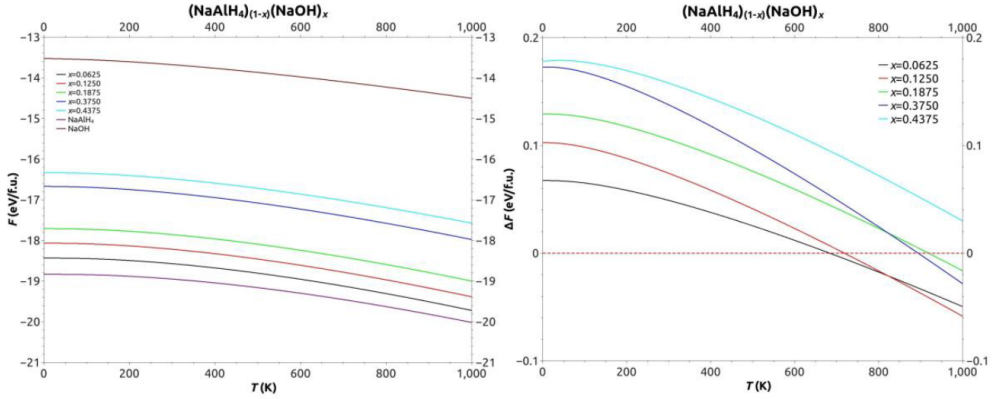


Figure 5 (Left). The free energies of $(NaAlH_4)_{(1-x)}(NaOH)_x$.

(Right). The changes of free energies. For a particular concentration $x$, $OH^-$ is soluble when $\Delta F < 0$. As x increases $\Delta F$ at 0 K also increases.

Figure 6(b) shows the calculated enthalpies in a wide temperature range. The meaningful ones are above the temperatures at which solubility occurs. The figure shows that the reaction enthalpies increase with the increase of temperature, becoming more favorable.

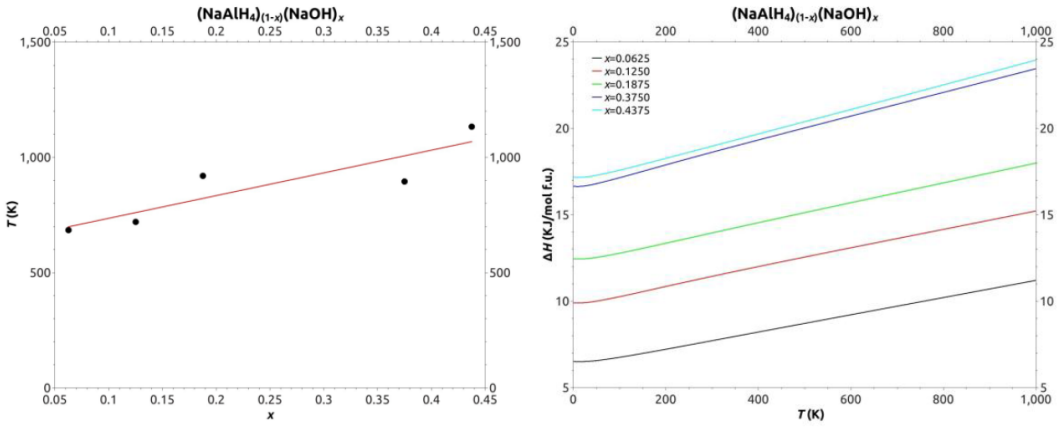


Figure 6 (Left). The solubility of NaOH into $NaAlH_4$ with temperature.

(Right). Molar solution enthalpies of $(NaAlH_4)_{(1-x)}(NaOH)_x$. As x increases the enthalpies also increase.

Mass spectroscopy measurements during the decomposition of these materials reveal some important clues to their reaction pathways. Figure 7 outlines the decomposition of bulk $NaAlH_4$. Under ultra high vacuum, a mass spectrum residual gas analyzer (MS-RGA) detects that the bulk material melts at 180 °C, and begins to release $H_2$ at about 200 °C. This reaction reaches its peak rate at 245 °C, and in some cases, a second round of $H_2$ emission precedes the decomposition of $Na_3AlH_6$ (at 280 °C) into NaH, Al, and $H_2$. In Figure 7, the mass (m/z) of 23 may represent the fracturing of NaH into the ions $Na^+$ and $H^-$ implying that NaH is lost as a gas. Small amounts of other ions are detected in the MS-RGA, which indicate that other gases are present in the $H_2$ stream. These gasses may be forming from oxygen impurities in the sample.

The Differential Scanning Calorimetry (DSC) instrument was used to measure the experimental decomposition enthalpies for pure $NaAlH_4$, N97 and N98. The enthalpies for the materials heated at 1 °C/minute are listed in Table 2.

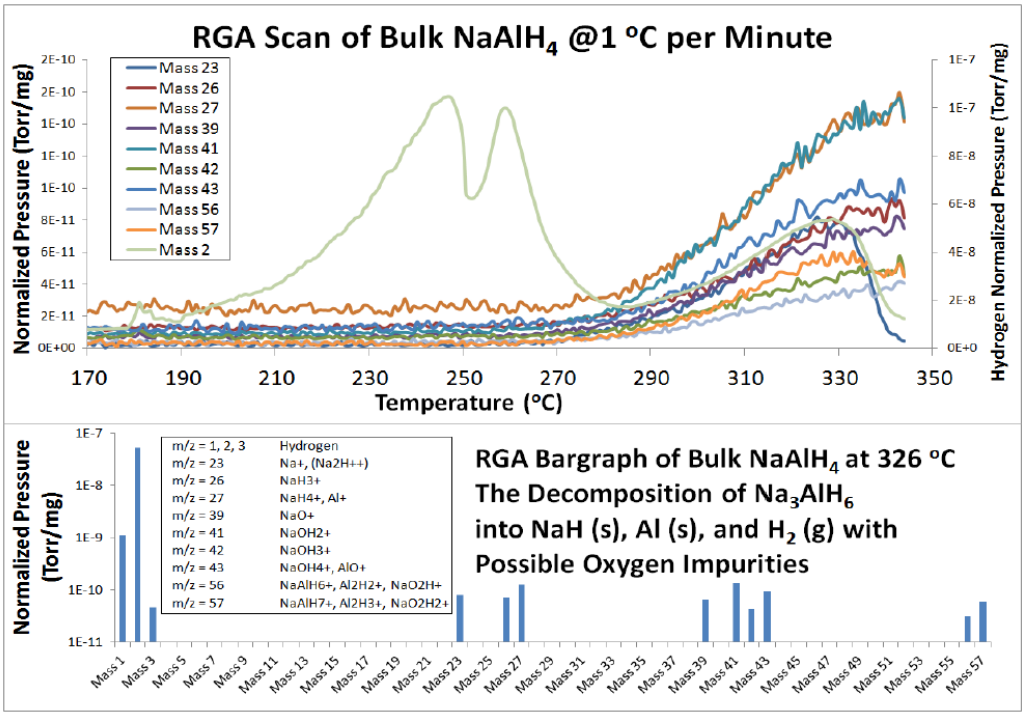


Figure 7. MS-RGA measurements of the thermal decomposition of $NaAlH_4$ showing increase in important masses during the second step of decomposition.

These DSC measurements are plotted along with the RGA data and most of the results have a strong correlation. The results of the MS-RGA show that all 3 samples decompose through the same reaction pathways, but N97 and N98 decompose at a lower temperature than the bulk material. Additionally, N98 in the S105 phase shows a smaller temperature range for Reaction 2 to complete.

Table 2. DSC experimentally calculated enthalpies.

| | Bulk | | N97 | | N98(S105 phase) | |
|---|---|---|---|---|---|---|
| | °C | J/g | °C | J/g | °C | J/g |
| Reaction 1 | 183 | 273 | 179 | 315 | 179 | 166 |
| Reaction 2 | 250 | 487 | 250 | 333 | 234 | 434 |
| Reaction 3 | 434 | 614 | 402 | 801 | 391 | 802 |

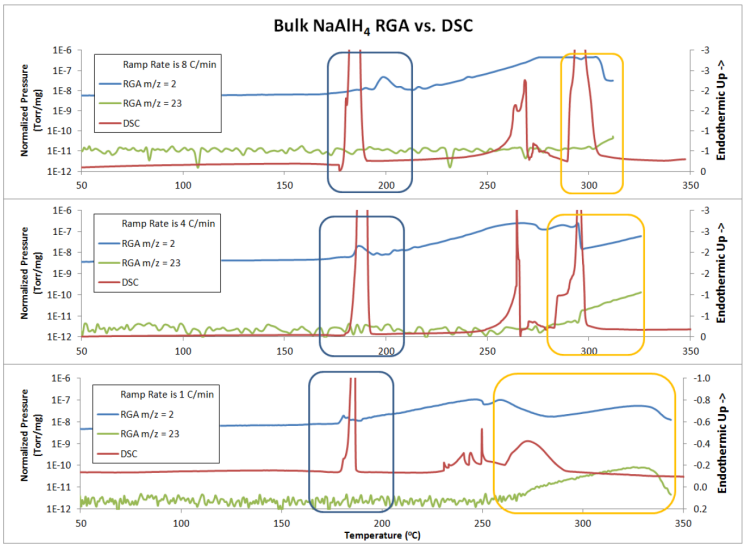


Figure 8.(a). MS-RGA measurements of the thermal decomposition at various ramp rates for bulk $NaAlH_4$. In figures (a)-(c): the top dark line represents the partial pressure of $H_2$, the bottom dark line represents DSC analysis, and the bottom grey line represents the partial pressure of NaH. Starting from the top chart, the ramp rates are 8, 4, and 1 °C/minute.

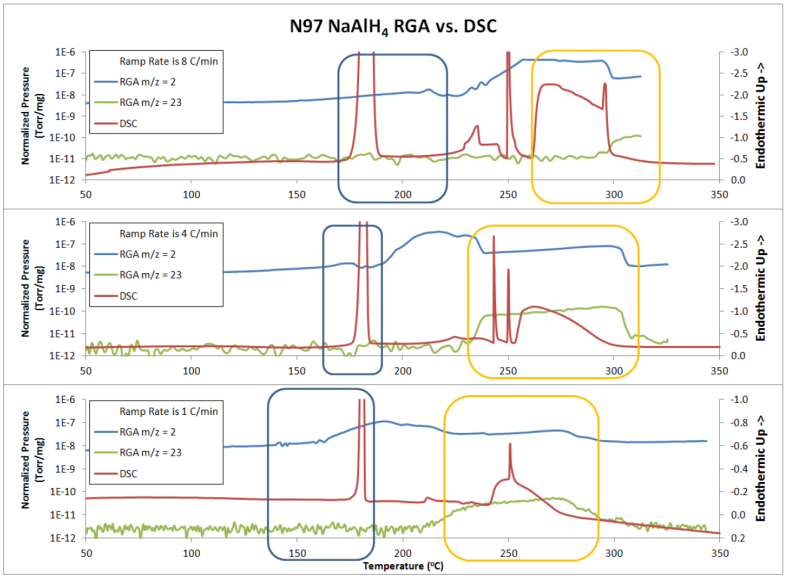


Figure 8.(b). MS-RGA measurements of the thermal decomposition at various ramp rates for high $H_2$ pressure N97.

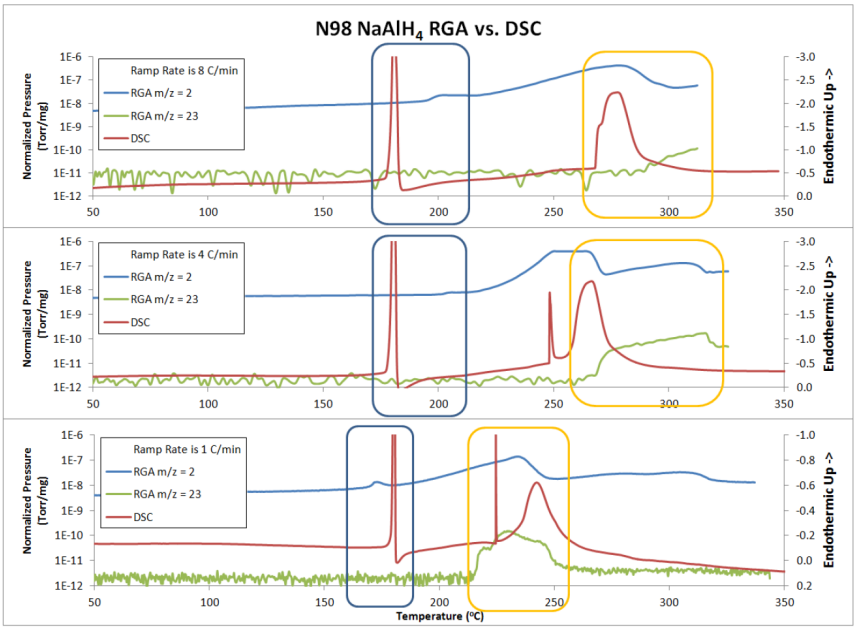


Figure 8.(c). MS-RGA measurements of the thermal decomposition at various ramp rates for the high temperature/pressure phase “S105” N98.

## CONCLUSION

Heat and pressure-treated $NaAlH_4$ in the S105 phase has been shown to melt and decompose into $Na_3AlH_6$ and $H_2$ gas at a lower temperature than the as-prepared bulk material. This would indicate that the effect of pretreating $NaAlH_4$ with a high temperature and $H_2$ pressure improves this material's ability to store and release $H_2$ gas at moderate temperatures without the use of catalysts.

## ACKNOWLEDGEMENTS

The authors gratefully acknowledge support from DOE Basic Energy Sciences grant DE-FG02-05ER46256.

## REFERENCES

[1] "Discovery of a New Al Species in Hydrogen Reactions of $NaAlH_4$" Ivancic, T. M.; Hwang, S-J.; Bowman, R. C., Jr.; Birkmire, D. S.; Jensen, C. M.; Udovic, T. J.; Conradi, M. S., *Phys. Chem. Lett*. **2010**, 1, 2412- 2416.

[2] "Mobile Species in $NaAlH_4$" Eric Glenn Sorte, Robert C. Bowman, Eric H. Majzoub, Margriet H.W. Verkuijlen, Terrence J. Udovic, and Mark S. Conradi, *J. Phys. Chem. C*. **2013**, 117(16), 8105-8113.

[3] "General Structure Analysis System (GSAS)" A.C. Larson and R.B. Von Dreele, *Los Alamos National Laboratory Report* LAUR 86-748 (**2000**).

[4] "Metal-doped sodium aluminium hydrides as potential new hydrogen storage materials" B. Bogdanovic, R.A. Brand, A. Marjanovic, M. Schwicardi, J. Tolle, *J. Alloys and Compounds*, v302, 36, **2000**.

## II. EFFECTS OF NaOH IN SOLID NaH: SOLUTION/SEGREGATION PHASE TRANSITION AND DIFFUSION ACCELERATION

Eric G. Sorte,[*,†] E. H. Majzoub,[‡] Tim Ellis-Caleo,[†] Blake A. Hammann,[§] Gang Wang,[‡] Dongxue Zhao,[‡] Robert C. Bowman, Jr.,[||] and Mark S. Conradi [*,†,§]

[†]Department of Physics, Washington University, One Brookings Drive, Saint Louis, Missouri 63130, United States

[‡]Center for Nanoscience and Department of Physics and Astronomy, University of Missouri St. Louis, One University Boulevard, St. Louis, Missouri 63121, United States

[§]Department of Chemistry, Washington University, One Brookings Drive, Saint Louis, Missouri 63130, United States

[||]RCB Hydrides, LLC, 117 Miami Avenue, Franklin, Ohio 45005, United States

### ABSTRACT

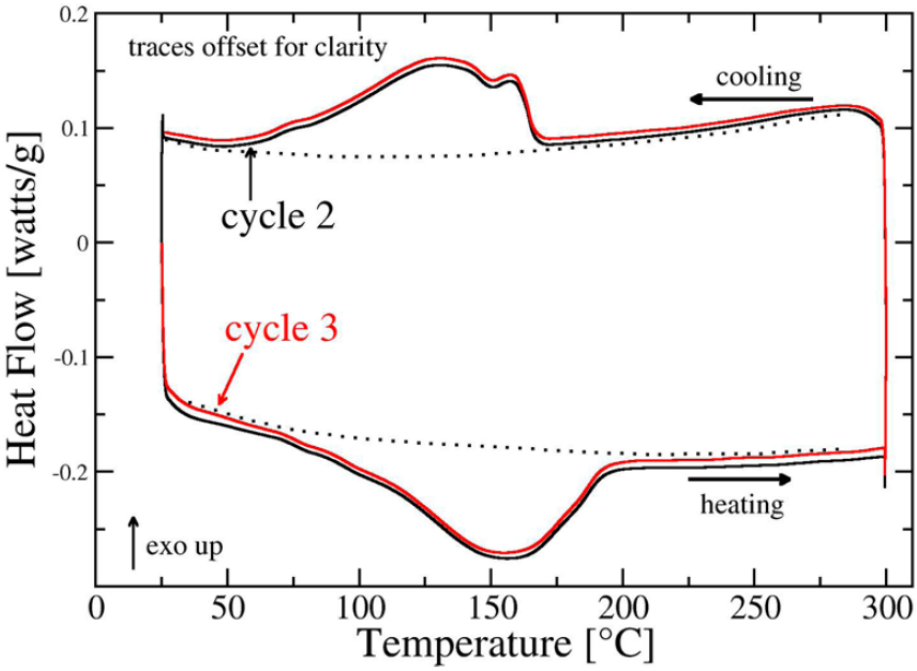


The presence of approximately 10 mol % NaOH mixed with NaH powder is shown to result in much more rapid hydrogen motion in the NaH above 150 °C, as indicated by the

onset of hydrogen NMR line narrowing at this temperature. A similar result appears for air-exposed NaH due to the formation of hydroxide from atmospheric $H_2O$. The NMR line narrowing is too rapid, as a function of temperature, to be described by thermal activation; rather, it is suggestive of a phase transition. Indeed, differential scanning calorimetry finds, after an initial thermal cycle, a reversible thermal anomaly indicating a phase transition near 150 °C. Powder X-ray diffraction with an excess of NaOH displays a remarkable lattice expansion of the NaH in the temperature range of 100−240 °C where the (200), (220), and (311) reflections indicate a volume lattice expansion of up to 11%; the expansion is reversible upon cycling. The data thus point to a reversible phase transition in which NaOH enters the NaH structure above 150 °C and exits the NaH below that temperature. First-principles calculations using OH-substituted NaH supercells indicate significant solubility in the NaH lattice and find a transition temperature and enthalpy change that are in approximate agreement with differential scanning calorimetry (DSC) measurements, confirming the presence of a phase transition.

## INTRODUCTION

The slow rate of hydrogen diffusion in many metal hydrides is often a limiting factor in whether the material can ultimately be useful as a means of practical hydrogen storage.[1−4] Diffusion of hydrogen in storage solids is crucial to the kinetics of dehydriding and rehydriding.[5] A well-known example of this is the "hydrogen-blockade" formed during hydriding of Mg: a thick layer of $MgH_2$ forms on the outside of Mg particles and, due to the slow diffusion of hydrogen through $MgH_2$, blocks further uptake and reaction of hydrogen.[6] As one of the simplest and most well-understood [7−9] light metal hydrides, NaH can provide a test case for many of the other hydrides of more practical interest. Moreover, $NaAlH_4$ (a viable hydrogen storage system) dehydrides to yield NaH, as well as Al and $H_2$ gas. Its rehydriding behavior is therefore dependent on the surface properties and impurity-induced changes of the NaH. Thus, the present results will be of interest to the larger hydrogen storage community. NMR has proven extremely useful in determining hydrogen diffusion rates in metal hydrides and for identifying strategies to enhance diffusion. [2,10−12] An earlier NMR study focused on the intrinsic, thermally activated hydrogen line narrowing of NaH. [13] While an investigation of the effects of

NaOH in NaH was not the main focus of that work, it was noticed that one NaOH-containing sample showed substantially early hydrogen line narrowing (i.e., narrowing commencing at a lower temperature). This sample was estimated to contain 30 mol % NaOH on the basis of integrated X-ray diffraction (XRD) peak area and displayed $^{1}$H NMR early line narrowing starting near 140 °C. A second NaOH-containing sample line narrowed in the 250−275 °C range, just as nominally pure NaH does. In that work,[13] this second sample was incorrectly estimated to contain 20 mol % NaOH; a reanalysis of the XRD data reveals that this sample had only 5 mol % NaOH. The normal hydrogen line-narrowing behavior of the second sample is therefore not unexpected. The surprising early line narrowing of the sample containing 30 mol % NaOH is the motivation for the current work. Here, we report the results of a thorough investigation of the effects of hydroxide additives on the hydrogen diffusion behavior of NaH, focusing on the effects of NaOH with NaH. We show new NMR line-shape measurements as a function of temperature as well as results from differential scanning calorimetry (DSC) and in situ powder XRD. First principles calculations confirm the experimental results and provide a partial explanation of the behavior. Together, these data point to a solid−solid phase transition in NaH containing NaOH.

## EXPERIMENTAL METHODS

NaH material was used as received from Sigma-Aldrich, with a stated purity of 95%. NaOH was also purchased from Sigma-Aldrich. One bottle of NaOH appeared to have absorbed some atmospheric water and is here termed wet NaOH; based on NMR measurements described below, we estimate our wet NaOH to have about 3.5 mol % $H_2O$. For some measurements, we dried NaOH at 150 °C under vacuum for 48 h to yield dry NaOH. All samples were handled in a glovebag with flowing pure $N_2$ gas (at WU) and in an argon atmosphere glovebox (at UMSL). Samples were flame-sealed into glass tubes for NMR measurements. Except when otherwise indicated, all samples were combined by hand-mixing the powders or grinding with a mortar and pestle for about 100 s in an inert atmosphere.

Hydrogen NMR lineshapes were obtained from a home-built spectrometer operating at 85.03 MHz (2.0 T). Free induction decays (FIDs) were corrected for the

receiver blocking/probe ringing at early times and Fourier transformed.[14] Some $^{23}Na$ spectra were measured at 4.7 and 7.0 T (53.4 and 79.3 MHz). In all cases, care was taken to record fully relaxed signals (the proton spin lattice relaxation time $T_1$ in many of these samples is long). The temperature was controlled with a stream of heated, thermally regulated air flowing across the sample.

Differential scanning calorimetry (DSC) was performed on a Q2000 series analyzer (TA Instruments). About 6 mg of sample was loaded in an aluminum pan in an argon-filled glovebox and crimped with an aluminum hermetic lid. The sample was heated to a maximum of 300 °C; the typical heating and cooling rates were 5 °C/min.

Hot stage (in situ) powder X-ray diffraction (XRD) was performed on a Rigaku Ultima IV diffractometer with an HT 1500 high-temperature attachment. XRD measurements used Cu Kα radiation, and the samples were held as thin, uniform layers of powder on a Pt slide and measured under dynamic vacuum. The temperature was measured with an R-type thermocouple in a temperature-controlled feedback loop. Air exposure of the samples was unavoidable when loading into the Rigaku high-temperature attachment. As a result, we also performed some variable-temperature XRD measurements on a homemade XRD hot stage that permitted air/water exclusion from the sample. Samples were loaded in a glovebox on an aluminum XRD slide and sealed with Kapton tape (the adhesive is good to 260 °C according to the manufacturer's specifications). The slide was then loaded into the Rigaku diffractometer, and a 25 W Dale power resistor with a flat extruded aluminum case was attached to the bottom of the aluminum sample holder. The sample was heated by applying ac voltage to the power resistor through a variable autotransformer or through a temperature-regulating circuit. The temperature was measured and controlled with T-type thermocouples. Some XRD measurements at room temperature were also performed with samples sealed under a lowdensity polyethylene film (Saran wrap).

## COMPUTATIONAL METHODS

First-principles calculations were performed using the planewave density functional theory (DFT) code VASP (Vienna Abinitio Simulation Package).[15,16] The generalized gradient functional of Perdew and Wang [17] was used to describe exchange-correlation of

the electrons, and the projector augmented wave (PAW) method was used to describe the interaction between the valence electrons and ion cores.[18,19] The planewave cutoff energy was 600.0 eV for all calculations. Monkhorst−Pack meshes were used for k-point sampling of the Brillouin zone with a spacing of less than 0.05 $Å^{-1}$.[20]

Hydroxide-substituted crystal structures were generated by placing OH anions at random H locations in NaH supercells for a variety of OH/H ratios. These structures were relaxed using the conjugate gradient algorithm until the forces on the atoms were below 0.01 eV/Å and stresses were below 0.05 kbar. Finite-temperature thermodynamics were obtained from the crystal entropy in the harmonic approximation, using phonon frequencies calculated from the linear response capabilities in VASP5.

The phase diagram of the NaH/NaOH system was calculated by minimizing the Gibb's free energy as a function of temperature at constant pressure using the Grand Canonical Linear Programming method presented elsewhere.[21]

## RESULTS AND DISCUSSION

**NMR.** The $^1H$ NMR linewidths as a function of temperature for several NaH samples appear in Figure 1. In essence, when the hydrogen nuclear spins begin to translationally hop at a rate of $10^5$ $s^{-1}$ or faster, the dipolar contributions to the hydrogen linewidth are time-averaged, resulting in a reduction in hydrogen NMR linewidth. Faster motion results in a narrower resonance line in this regime. The linewidth curves fall into two classes − those that narrow in the 250−275 °C range and those that narrow near 150 °C. The list of systems that narrow in the 250−275 °C range includes nominally pure NaH, NaH + dried NaOH on the first heating, NaH + dried $Al(OH)_3$, and NaH + $Mg(OH)_2$. All of the hydroxide additives are present in concentrations of approximately 10 mol %. Systems that narrow in the 150 °C range include NaH + wet (i.e., not specifically dried) NaOH in various concentrations, NaH + wet $Al(OH)_3$, air-exposed NaH, and the NaH + dried NaOH in subsequent heating cycles (indicated as [C2] and [C3] for temperature cycles 2 and 3 in Figure 1).

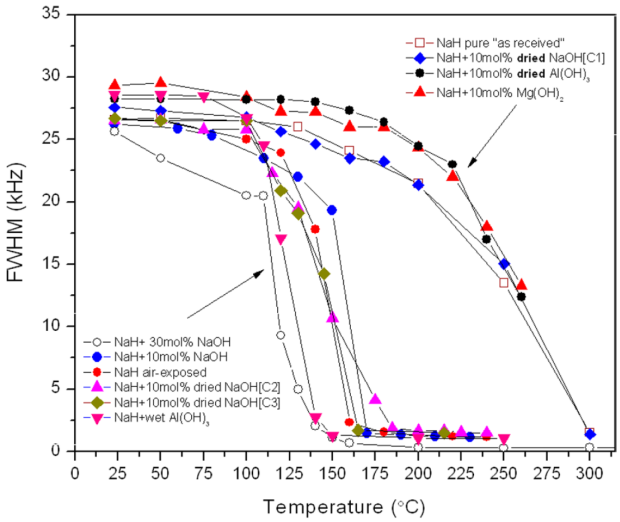


**Figure 1.** $^{1}$H NMR linewidths of samples of NaH mixed with various additives. The plot indicates the full-width-at-half-maximum (fwhm) of the hydrogen resonance. Samples indicated in the top legend include pure NaH and NaH + dried hydroxides (C1 = temperature cycle 1). Samples indicated in the bottom legend include NaH + wet hydroxides, air-exposed NaH, and NaH + dried NaOH on the second and third temperature cycles (C2 and C3, respectively). The curves through the data are guides for the eyes.

It is important to note that in all of the cases in Figure 1 the lineshapes showed uniform narrowing; that is, the entire resonance is narrowed. In Figure 2, the lineshapes for air-exposed NaH are shown. This sample is representative of the group of samples whose resonances are seen to narrow around 150 °C in Figure 1. The uniform narrowing observed here is in contrast to many reported systems, particularly ball-milled hydrides, which display a narrowed component superimposed on a broad resonance.[2,10,22] We also remark that NaH is the primary component in all the samples, so the hydrogen NMR signal is dominated by hydrogen from the NaH. For samples with smaller concentrations of NaOH, such as 1−5 mol % in hand-mixed powders, line narrowing was observed near 150 °C, but only for a portion of the hydrogen resonance. That is, for the samples with lower concentrations of NaOH, there was a broad signal (not narrowed) together with the narrowed component.

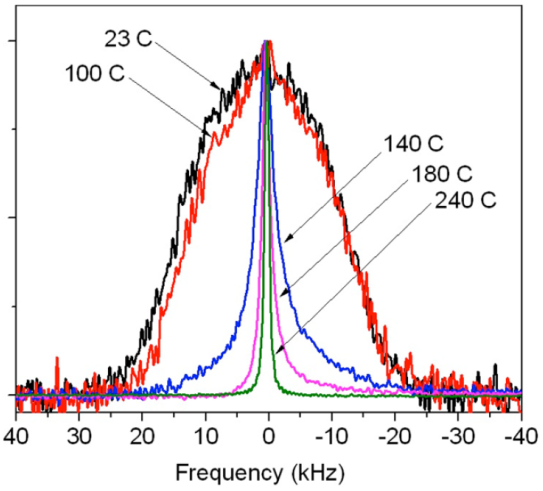


**Figure 2.** $^{1}$H NMR of air-exposed NaH. The NaH was exposed to the air for 5 min prior to NMR measurements. All curves have been normalized to the room-temperature peak amplitude. Note the dramatic narrowing from 100 to 140 °C.

$^{23}$Na NMR was also performed on the samples above to investigate the effects of NaOH on the sodium motion. The previous study [13] of sodium hydride reported some cation motion in NaH with 30 mol % NaOH upon the second and third heating cycles at the highest temperatures. In the present study, where smaller amounts of NaOH were present, we saw no significant line narrowing of the $^{23}$Na (beyond the narrowing expected from the hydrogen motion [13]), which would have indicated sodium motion in the samples (data not shown).

*Thermal Activation Analysis.* The hydrogen linewidths of the early narrowing samples in Figure 1 (example spectra for which are shown in Figure 2) are remarkably rapid functions of temperature. We tried fitting the thermal activation expression (Arrhenius, describing single particle, over-the-barrier motion) to the data using

$$\frac{1}{\tau} = \omega_0 \exp[-E/K_B T] \quad (1)$$

Here $\tau$ is the jump time of hydrogen in NaH; $\omega_0$ is the attempt frequency; E is the activation energy for hopping motion; and T is the absolute temperature. At the onset of narrowing, $1/\tau$ is nearly equal to the rigid lattice (unnarrowed) linewidth, about $10^5$ $s^{-1}$.

We set the attempt frequency to a typical vibrational frequency of $10^{13}$ $s^{-1}$. The activation energy is then chosen so that $1/\tau$ from eq 1 yields $10^5$ $s^{-1}$ at 150 °C; the result is E = 0.67 eV ($E/k_B$ = 7800 K). However, as discussed below, this activation energy is too small to describe the strong temperature dependence of the narrowing.

In the regime of narrowing, the linewidth $\Delta f$ varies reciprocally with the rate of motion [23−25]

$$\Delta f = \frac{1}{2\pi} M_2 \tau \tag{2}$$

where $M_2$ is a mean-squared dipole−dipole interaction strength. Using the above-obtained estimate of activation energy $E$, the linewidth predicted from eq 2 falls approximately only half as rapidly with further temperature increase, compared to the data. A much larger value of E would describe the steep slope of the linewidths near 150 °C in Figure 1. However, this would require an unphysically large attempt frequency $\omega_0$ to agree with the observed temperature (150 °C) of narrowing onset. Thus, a reasonable value of $\omega_0$ and a value of $E$ chosen to fit the temperature of the onset of narrowing cannot explain why the narrowing is such a strong function of temperature. As a comparison, for the samples that narrow in the 250−275 °C range, the variation of linewidth versus temperature is in accord with the activation energy (0.83 eV and $E/k_B$ = 9600 K) similarly obtained. Indeed, the much steeper slope of the linewidth of the early narrowing samples, compared to those narrowing in the 250−275 °C range, is clearly evident in Figure 1. Thus, for the samples narrowing near 150 °C, the thermal activation calculations suggest that a more collective process, such as a phase transition, is involved in the rapid transition to complete motional narrowing. Measurements of linewidth on subsequent temperature cycles are reversible and repeatable, confirming that any phase transition is reversible.

*Effects of Water.* A perplexing aspect of the observed early narrowing is how a mixture of solid powders can interact at all since dry powder particles presumably touch only at asperities or protrusions. A more intimate and thorough contact would occur if there were small amounts of a liquid agent present. We performed hydrogen NMR on our wet NaOH powder without any added NaH to look for such a liquid. At and above 60 °C, a liquid signal is evident on top of the broad solid signal. According to published

$NaOH{\cdot}H_2O$ phase diagrams, [26–28] a two-phase coexistence between pure NaOH solid and an NaOH-rich water-containing liquid occurs at and above 60 °C, which explains our observation of a liquid-like signal above 60 °C in the wet NaOH NMR. Below 60 °C the phase diagram predicts coexistence between NaOH solid and $NaOH{\cdot}H_2O$ monohydrate solid, and indeed only a solid signal is observed below that temperature in our wet NaOH. According to the phase diagram, the relative amount of liquid in the two-phase coexistence above 60 °C increases with increasing $H_2O$ content. From the relative intensities of the liquid and solid signals at 80 °C, we determined that the wet NaOH contained approximately 3.5 mol % water. We note that there was no liquid-like signal observed in specifically dried NaOH up to 250 °C.

In our NaH + wet NaOH mixed samples, we believe the absorbed water in the NaOH provides the medium to allow for the necessary contact between the NaH and NaOH powders. Similarly, in the NaH + wet $Al(OH)_3$ sample and the initially pure NaH sample that had been exposed to laboratory air for 5 min, we believe that residual water absorbed in the hygroscopic hydroxide or from the atmosphere reacts with the NaH to produce NaOH through

$$NaH + H_2O \rightarrow NaOH + H_2 \tag{3}$$

Indeed, when the hydroxides were scrupulously dried prior to mixing with the NaH, the early line-narrowing effect vanished (see Figure 1) on the first heating. However, after heating beyond the 318 °C melting point of NaOH, subsequent heatings of the NaH + dry NaOH did show the onset of early line narrowing, indicating that the first thermal cycle caused a change in the NaH + dry NaOH mixture. Specifically, we propose that the molten NaOH partially dissolved into the NaH on the first heating, as discussed below, and exited the NaH as very small precipitates upon cooling. The resulting intimate NaH−NaOH contacts were effective on subsequent cycles for promoting rapid kinetics.

*Effects of Other Additives.* Beyond the systems in Figure 1, we examined many other systems, including NaH mixed with silica, alumina, NaBr, NaCl, NaF, and $MgH_2$. For hand-mixed samples of the above constituents, the effects on both the hydrogen and

sodium linewidths were small. For ball-milled mixtures, even inert additives like $SiO_2$ resulted in a narrow component on top of a broad hydrogen resonance, similar to what has been reported for other ball-milled systems.[2,10,22] The effects of ball-milled impurities on NaH are not the subject of this work; by hand mixing our samples we avoided the complications of the narrow resonance component due to ball milling. We do note that ball milling our nominally pure dry NaH did not result in any change in line narrowing of the main broad resonance compared to the initial NaH powder. It is possible that NaH does not ball mill to a small grain size in the absence of additives. For example, it has been noticed in LiH + LiOH that ball milling with additives leads to a much finer dispersal and mixing than does ball milling the compounds alone.[29] Also, some alanates ($NaAlH_4$ and $LiAlH_4$) are extremely difficult to refine by ball milling.[30]

**Scanning Calorimetry.** The strong temperature dependence of the line narrowing motivated us to use DSC on handmixed powders of NaH with wet NaOH. To enhance any effects, the concentration of NaOH was made to be 20 mol %, up from the 10 mol % used in many of the NMR samples. On first heating (not shown), there was a broad endothermic peak from 280 to 320 °C, which includes the melting of NaOH at 318 °C. Upon cooling, and on subsequent heating cycles, a prominent thermal anomaly was apparent near 150 °C, as presented in Figure 3. The heating (bottom) curves show an endothermic peak, and the cooling (top) curves show an exothermic peak, as would be expected for an equilibrium phase transition. Figure 3 presents data from the second and third heating cycles; clearly the data are reversible. The reversibility of this transition is a remarkable aspect of the NaOH−NaH system.

The enthalpy of the reaction calculated by integrating under the endothermic and exothermic peaks is roughly 50 J/g, i.e., 50 J per total grams, so 1360 J/mol. Thus, the molar entropy change at the transition (taken as 150 °C) is 0.39R, where R is the gas constant. For an ideal solid solution of concentration $x$, the configurational entropy is

$$\Delta S = R\,[\,-x\,ln\,x - (1-x)\ln\,(1-x)\,] \qquad (4)$$

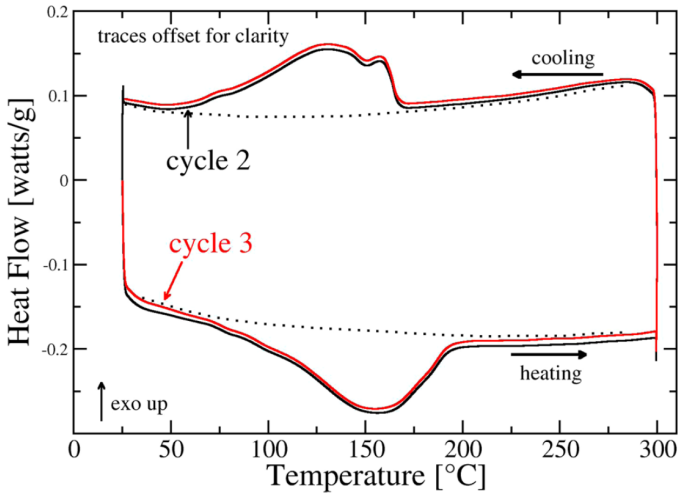


**Figure 3.** Differential Scanning Calorimetry (DSC) data for a 2:8 molar mixture of NaOH:NaH. The first cycle (not shown) is taken above the melting temperature of NaOH (318 °C). Subsequent cycles below the melting temperature of NaOH show the reversible behavior. The dashed lines are guides for the eyes, serving as baselines.

Using the present $x = 0.2$, we expect $\Delta S$ of about $0.5R$. The agreement with the measured value is as good as should be expected for such DSC data. In addition, the transition may not run to completion, and there may be short-range order in the solid solution, all of which would decrease the experimental entropy change.

The transition in NaH with NaOH resembles the behavior of KCl−NaCl, as studied by Barrett and Wallace.[31] There the miscibility gap between KCl and NaCl closes while still in the solid. At low temperatures, nearly pure KCl and NaCl are found, while a single-phase solid solution appears at high temperatures. Other systems such as NaCl−NaBr [32] and III−V pseudobinary semiconductor alloys [33] behave similarly.

**X-ray Diffraction.** In situ powder XRD was carried out to observe the NaH/NaOH mixtures during the heating process. We used a mixture of NaH + dried NaOH for this study. In situ XRD of physically mixed 2:8 ratio mixtures of NaOH:NaH from room temperature to 240 °C show a shifting of the NaH peaks, giving a thermal expansion of about 1.3% of the unit cell length, not significantly greater than our measurements of pure NaH at 1.15%. Our measurements of the thermal expansion of pure NaH were in reasonable agreement with those of Kuznetsov, with a linear expansion constant of $\alpha_L = 60 \times 10^{-6}$ °C. [34]

In an attempt to saturate the solubility limit of NaOH in NaH [35] and see the largest possible effect, we also used a mixture of approximately 80 mol % NaOH. The sample was exposed to an initial heat treatment of 330 °C for 1 h under 70 bar $H_2$, thus melting the NaOH. The sample was then cooled to room temperature and loaded into the hot-stage XRD. Figure 4 shows the initial XRD of the starting materials and relevant peak indices. The majority phase in this sample is NaOH, and the NaH (111) peak appears as a shoulder just below 32 degrees two-theta. The platinum peaks belong to the high-temperature sample holder. The in situ data are shown in Figure 5; the time progression begins at the bottom of the figure ($T$ = 35 °C), proceeds upward as the sample is heated to 240 °C, and ends at the top of the figure as the sample is cooled back to 55 °C.

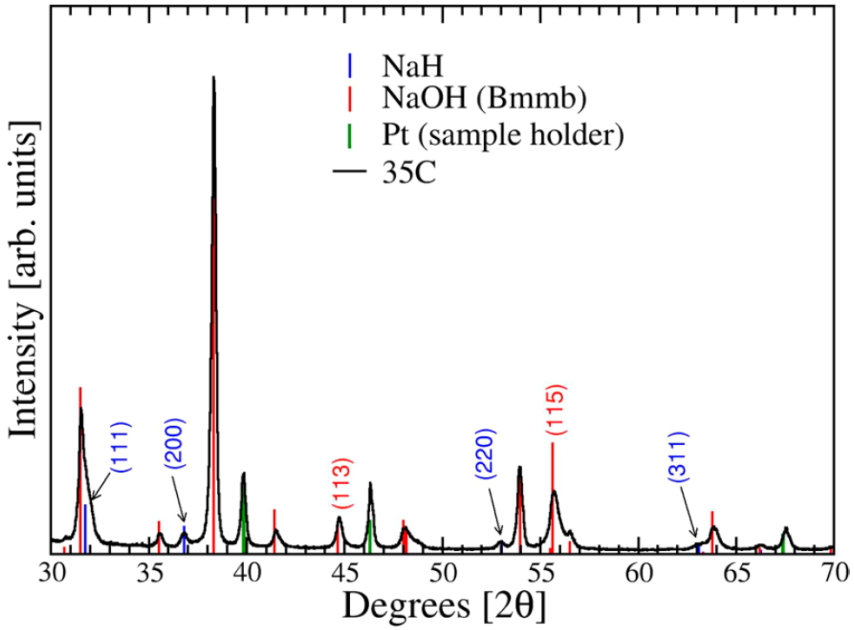


**Figure 4.** First XRD scan of the in situ data for premelted 80% NaOH with 20% NaH at 35 °C. Stick patterns are for NaH (blue), NaOH in spacegroup Bmmb (red), and platinum sample holder (green). The peak indexes (111), (200), (220), and (311) correspond to NaH.

The NaOH peaks present in Figure 5 shift slightly to lower angle as the temperature is increased and return to their roomtemperature positions as the sample is cooled. This shift corresponds to simple thermal expansion of the NaOH lattice with an

increase in the cell volume from 131 $Å^3$ to about 134 $Å^3$, about 2% volumetrically (0.7% linear expansion). The NaH peaks, in contrast, show a more remarkable behavior. As the sample is heated to 240 °C, the NaH (200), (220), and (311) reflections (at 36.8°, 53.0°, and 63.1°, respectively, indicated by black dots in Figure 5) shift dramatically to lower angles, demonstrating an approximate 3.5% increase in lattice parameter, an approximately 11% increase in cell volume. As the sample cools, the reflections nearly return to their initial positions and intensities. The expansion suggests that some NaOH enters the NaH lattice on heating and exits upon cooling. At 240 °C, the NaH peaks sharpen and increase in intensity at the same time as several of the NaOH peaks (e.g., at 44.8°, 55.8°, and 64°) broaden and shrink. The loss of some NaOH peaks at 240 °C is likely related to the structural phase transition from Bmmb (orthorhombic) to $P2_1/m$ (monoclinic) that is reported to occur at 241 °C. [36,37]

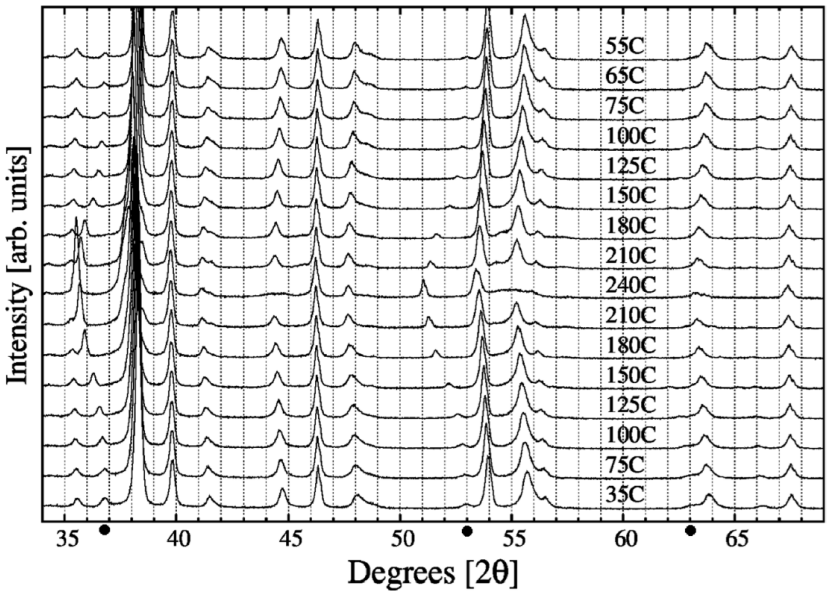


**Figure 5.** In situ XRD of 8:2 molar ratio of NaOH:NaH. Note the peak shifts of the NaH (200) at about 37° and (220) at about 53° (highlighted by black dots on the x-axis); the weak (311) at about 63° shifts similarly but is only evident with magnification. Refer to Figure 4 for identification of the peaks. Vertical guidelines (dotted lines) are given to emphasize the peak shifts.

In this picture, the effect of the first thermal cycle is to dissolve NaOH into the NaH and, upon cooling, to precipitate out the NaOH. The fine precipitates have larger contact area with the NaH and are small, both of which promote the kinetics in subsequent thermal cycles. The fine precipitates are involved in the DSC behavior on second and higher temperature cycles, as discussed above in connection with Figure 3.

For an fcc lattice (like NaH) with cube edge length *a*, the spacing *d* of the X-ray reflecting planes (specified by integers *h*, *k*, *l*) during a lattice expansion will obey the *d*-spacing formula

$$\frac{1}{d^2} = \frac{h^2 + k^2 + l^2}{a^2} \tag{5}$$

The diffraction condition is given by

$$\frac{1}{d} = \frac{2 \sin\theta}{\lambda} \tag{6}$$

The NaH (200), (220), and (311) peaks appear to shift in accordance with the cubic *d*-spacing formula as temperature increases. Additionally, the shifted (220) peak appears to split at the highest temperatures, suggesting a small distortion in the fcc lattice. As the sample cools, the NaH returns to an fcc lattice parameter of 4.87 Å, the nominal value for pure NaH. [34] We note that NaOH has an fcc phase above 293 °C, [36] allowing NaOH to be compared to (fcc) NaH at the same temperature. For NaOH, the lattice parameter is 5.10 Å, [36] just 3% larger than the 4.95 Å of NaH, [34] all at 300 °C. The similar sizes imply that dissolution of NaOH into NaH is feasible.

We return to the question: why does the hydrogen in NaH diffuse so much faster (see Figures 1 and 2) once some NaOH has entered the NaH lattice? The increase in NaH lattice parameter even with the 20% NaOH material is barely larger than the thermal expansion for pure NaH (see above). Thus, lattice expansion does not explain the increased rate of hydrogen motion. The OH dynamic orientational disorder may play a role [38] in the accelerated diffusion. In the end, the reason for enhanced motion of the hydrogen anions in NaH is not known.

**First-Principles Calculations.** The solubility of NaOH in NaH can be studied computationally by investigating the reaction

$$(1-x)\mathrm{NaH} + x\mathrm{NaOH} \rightarrow \mathrm{NaH}_{(1-x)}(\mathrm{OH})_x \quad (7)$$

for $0 < x < 1$. The solid solution $\mathrm{NaH}_{(1-x)}(\mathrm{OH})_x$ is favorable when the free energy becomes less than the sum of the free energies of separated NaOH and NaH

$$\Delta F = F\left[NaH_{(1-x)}(OH)_x\right] - xF(NaOH) - (1-x)F(NaH) < 0 \quad (8)$$

where F are molar free energies.

Table 1. Total energies ($T$ = 0 K), Zero-Point Energy (ZPE), and thermodynamic data from first-principles calculations[a].

| Compound | $U_0$ (eV/f.u.) | ZPE (eV/f.u.) | # f.u. | NaOH % | Conf. $S$ (eV/K/cell) | Calc. $S$ (298 K) (J/mol/K) | $T_c$ (°C) | $\Delta H(T_c)$ (J/g) |
|---|---|---|---|---|---|---|---|---|
| NaOH | -13.766 | 0.364 | 32 | - | - | 60.78 | - | - |
| NaH | -5.154 | 0.159 | 32 | - | - | 37.02 | - | - |
| $Na_{32}H_{29}(OH)_3$ | -190.200 | 5.651 | 1 | 9.38 | 0.00086 | 43.41 | 130 | 67 |
| $Na_{32}H_{26}(OH)_6$ | -215.709 | 6.290 | 1 | 18.75 | 0.00133 | 47.14 | 209 | 104 |

[a]The calculated critical temperatures indicate when the composite crystals become favorable. The enthalpy changes are given at the *calculated* critical temperatures.

The free energy of a solid as a function of temperature can be evaluated by

$$F = U_0 + \sum_r \{\tfrac{\hbar\omega_r}{2} + k_B T(1 - \exp[\tfrac{-\hbar\omega_r}{k_B T}])\} - TS_{conf} \quad (9)$$

where $U_0$ is the electronic total energy ($T$ = 0 K) of the structure from the geometric optimization via DFT; $k_B$ is Boltzmann's constant; $\omega_r$ are the phonon frequencies of the crystal; and the first term in the sum is the zero-point energy (ZPE) representing the atomic vibrations at $T$ = 0 K. Sconf denotes the configurational entropy and is given by eq 4 for the pseudobinary compound $\mathrm{NaH}_{(1-x)}(\mathrm{OH})_x$, considering the mixing between H and OH ions.

In the solid solubility calculations, the critical soluble temperature ($T_c$) is the temperature where the total free energy of a specific supercell becomes equal to that of the phase separated NaH and NaOH, i.e., where $\Delta F(T_c,x) = 0$, from eq 8. The enthalpy change at the critical temperature can be calculated by

$$\Delta H = T\Delta S = T[S(T,Na(OH)_x H_{(1-x)}) - xS(T,NaOH) - (1-x)S(T,NaH)] \qquad (10)$$

Table 1 shows the calculated critical temperatures and enthalpy changes for the solid solution reactions. The appropriate supercell sizes were chosen to be large enough that the calculated entropies are close to the experimental values. The calculated critical temperatures indicate when the solid solution phase becomes favorable according to eq 8, and the enthalpy change is given at the calculated critical temperature. All calculations used a 2 × 2 × 2 density of k-space points.

The solution of NaOH in NaH was investigated by calculating the reaction free energies and enthalpies for reaction 7. In the calculations, NaOH in space group Bmmb was used since it is the stable phase in the experimental temperature range. The NaH/NaOH supercells were created by adding appropriate numbers of oxygen atoms in a 32 f.u. NaH supercell. Metropolis Monte Carlo Simulated Annealing (MMCSA) was used to distribute the OH positions uniformly in NaH by placing the OH as far apart in the supercell as possible (obeying periodic boundary conditions). The atomic coordinates and cell geometry of the generated structures were optimized using the DFT methods described above. The enthalpy changes for the solution transition were calculated for the critical temperature obtained from the Grand Canonical Linear Programming (i.e., $\Delta F = 0$ in eq 8). Table 1 lists the calculated critical temperatures and the enthalpy changes of the solid solution of the NaOH in NaH at the critical temperatures. These temperatures in Table 1 are in reasonable accord with the experimental value of 150 °C from NMR at 10% NaOH content and from DSC at 20% NaOH. The enthalpies likewise show reasonable agreement, to within a factor of 2. The DFT calculations thus support the interpretation of the NMR and DSC data, indicating a phase transition between segregated components and a solid solution.

## CONCLUSIONS

Hydrogen NMR line narrowing of NaH hand mixed with NaOH occurs around 150 °C, approximately 100 °C cooler than for nominally pure NaH. Early hydrogen line narrowing is also obtained for NaH exposed to atmospheric moisture or moisture present in other compounds (i.e., wet $Al(OH)_3$) from the reaction

$$NaH + H_2O \rightarrow NaOH + H_2$$

The line narrowing is too strong a function of temperature to be represented by a physically reasonable Arrhenius dependence. Scanning calorimetry shows a reversible thermal anomaly near 150 °C for the system of mixed NaH and NaOH powders, after one thermal precycle. Powder XRD reveals a large and reversible lattice expansion of the NaH in the presence of excess NaOH beginning in the vicinity of 150 °C. DFT calculations show that the temperature for which $\Delta F = 0$ (the free energy of mixing) is comparable to our experimentally measured temperature.

Together, these data point to a reversible phase transition near 150 °C, with NaOH dissolving into solid NaH above the transition. Below this temperature, the NaOH is expelled from the NaH structure. The origins of the enhanced rate of hydrogen diffusion in NaH and the lower onset temperature of NMR line narrowing are not understood. However, the enhanced hydrogen diffusion observed here in sodium hydride samples containing hydroxide may be relevant for accelerating the hydrogen reaction kinetics of other hydrogen storage solids.

## ACKNOWLEDGEMENTS

The authors gratefully acknowledge support from the US Department of Energy, Basic Energy Science, through grant DE-FG02-ER46256. TE-C acknowledges partial support from Washington University's Office of Undergraduate Research. We thank David Osborn in the Center for Nanoscience for assistance in collecting the in situ XRD and DSC data. Special thanks are due to W. E. Buhro for alerting us to the work of Barrett and Wallace.

## REFERENCES

[1] Jensen, T. R.; Andreasen, A.; Vegge, T.; Andreasen, J. W.; Stahl, K.; Pedersen, A. S.; Nielsen, M. M.; Molenbroek, A. M.; Besenbacher, F. Dehydrogenation Kinetics of Pure And Nickel-Doped Magnesium Hydride Investigated by in situ Time-Resolved Powder X-Ray Diffraction. *Int. J. Hydrogen Energy* **2006**, *31*, 2052−2062.

[2] Corey, R. L.; Ivancic, T. M.; Shane, D. T.; Carl, E. A.; Bowman, R. C., Jr.; von Colbe, J. M. B.; Dornheim, M.; Bormann, R.; Huot, J.; et al. Hydrogen Motion in Magnesium Hydride by NMR. *J. Phys. Chem. C* **2008**, *112*, 19784−19790.

[3] Gross, A. F.; Vajo, J. J.; Van Atta, S. L.; Olson, G. L. Enhanced Hydrogen Storage Kinetics of $LiBH_4$ in Nanoporous Carbon Scaffolds. *J. Phys. Chem. C* **2008**, *112*, 5651−5657.

[4] Stephens, R. D.; Gross, A. F.; Van Atta, S. L.; Vajo, J. J.; Pinkerton, F. E. The Kinetic Enhancement of Hydrogen Cycling in $NaAlH_4$ by Melt Infusion into Nanoporous Carbon Aerogel. *Nanotechnology* **2009**, *20* (204018), 1−6.

[5] Borgschulte, A.; Jain, A.; Ramirez-Cuesta, A. J.; Martelli, P.; Remhof, A.; Friedrichs, O.; Gremaud, R.; Züttel, A. Mobility and Dynamics in the Complex Hydrides $LiAlH_4$ and $LiBH_4$. *Faraday Discuss*. **2011**, *151*, 213−230.

[6] Stander, C. M. Z. Kinetics of Formation of Magnesium Hydride from Magnesium and Hydrogen. *Phys. Chem. N. F*. **1977**, *104*, 229−238.

[7] Hao, S.; Sholl, D. S. Role of Schottky Defects in Hydrogen and Metal Diffusion in NaH, $MgH_2$, and $NaMgH_3$. *J. Phys. Chem. Lett*. **2010**, *1*, 2968−2973.

[8] Singh, S.; Eijt, S. W. H. Hydrogen Vacancies Facilitate Hydrogen Transport Kinetics in Sodium Hydride Nanocrystallites. *Phys. Rev. B* **2008**, *78* (224110), 1−6.

[9] Gnanasekaran, T. Thermochemistry of Binary Na−NaH and Ternary Na−O−H Systems and the Kinetics of Reaction of Hydrogen/Water With Liquid Sodium −A Review. *J. Nucl. Mater.* **1999**, *274*, 252−272.

[10] Shane, D. T.; Corey, R. L.; McIntosh, C.; Rayhel, L. H.; Bowman, R. C., Jr.; Vajo, J. J.; Gross, A. F.; Conradi, M. S. LiBH4 in Carbon Aerogel Nanoscaffolds: An NMR Study of Atomic Motions. *J. Phys. Chem. C* **2010**, *114*, 4008−4014.

[11] Sorte, E. G.; Bowman, R. C., Jr.; Majzoub, E. H.; Verkuijlen, M. H. W.; Udovic, T. J.; Conradi, M. S. Mobile Species in $NaAlH_4$. *J. Phys. Chem. C* **2013**, *117*, 8105−8113.

[12] Skripov, A. V.; Cherepanov, Yu. G.; Aleksashin, B. A.; Rychkova, S. V.; Stepanov, A. P. Nuclear Magnetic Resonance Study of Deuterium Diffusion in $ZrCr_2D_x$. *J. Alloys Compd*. **1995**, *227*, 28−31.

[13] Sorte, E. G.; Corey, R. L.; Bowman, R. C., Jr.; Birkmire, D.; Zidan, R.; Conradi, M. S. NMR Studies of NaH. *J. Phys. Chem. C* **2012**, *116*, 18649−18654.

[14] Brady, S. K.; Conradi, M. S.; Majer, G.; Barnes, R. G. Proton Magnetic Resonance Spectra of $YH_3$ and $LuH_3$. *Phys. Rev. B* **2005**, *72* (214111), 1−4.

[15] Kresse, G.; Hafner, J. Ab initio Molecular Dynamics for Liquid Metals. *Phys. Rev. B* **1993**, *47*, 558.

[16] Kresse, G.; Furthmuller, J. Efficient iterative schemes for ab initio total-energy calculations using a plane-wave basis set. *Phys. Rev. B* **1996**, *54*, 11169−11186.

[17] Perdew, J. P. In Electronic Structure of Solids; Ziesche, P., Eschrig, H., Eds.; Akademie Verlag: Berlin, **1991**; Vol. 11.

[18] Blochl, P. E. Projector Augmented-Wave Method. *Phys. Rev. B* **1994**, *50*, 17953−17979.

[19] Kresse, G.; Joubert, D. From Ultrasoft Pseudopotentials to the Projector Augmented-Wave Method. *Phys. Rev. B* **1999**, *59*, 1758−1775.

[20] Monkhorst, H. J.; Pack, J. D. Special Points for Brillouin-zone Integrations. *Phys. Rev. B* **1976**, *13*, 5188−5192.

[21] Akbarzadeh, A. R.; Ozolins, V.; Wolverton, C. First-Principles Determination of Multicomponent Hydride Phase Diagrams: Application to the Li-Mg-N-H System. *Adv. Mater.* **2007**, *19*, 3233−3239.

[22] Heitjans, P.; Wilkening, M. Ion Dynamics at Interfaces: Nuclear Magnetic Resonance Studies. *MRS Bull*. **2009**, *34*, 915−920.

[23] Anderson, P. W.; Weiss, P. R. Exchange Narrowing in Paramagnetic Resonance. *Rev. Mod. Phys.* **1953**, *25*, 269−276.

[24] Slichter, C. P. Principles of Magnetic Resonance; *Springer: New York*, **1980**.

[25] Abragam, A. The Principles of Nuclear Magnetism; *Oxford: London*, **1961**.

[26] Treptow, R. S. Phase Diagrams for Aqueous Systems. *J. Chem. Educ*. **1993**, *70*, 616−620.

[27] ORNL. Transphase cool storage test report. http://www.osti.gov/bridge/purl.cover.jsp?purl=/10112710/ (accessed Aug **2013**).

[28] JSIA. Safe handling of caustic soda. http://www.jsia.gr.jp/data/handling_01e.pdf [accessed Aug **2013**).

[29] Vajo, J. J.; Skeith, S. L.; Mertens, F.; Jorgensen, S. W. Hydrogen-Generating Solid-State Hydride/Hydroxide Reactions. *J. Alloys Compd*. **2005**, *390*, 55−61.

[30] Varin, R. A.; Czujko, T.; Wronski, Z. S. Nanomaterials for Solid State Hydrogen Storage; Springer: New York, **2008**.

[31] Barrett, W. T.; Wallace, W. E. Studies of NaCl-KCl Solid Solutions. I. Heats of Formation, Lattice Spacings, Densities, Schottky Defects and Mutual Solubilities. *J. Am. Chem. Soc.* **1954**, *76*, 366−369.

[32] Fineman, M. A.; Wallace, W. E. Heats of Formation and Some Derived Thermodynamic Properties of NaCl-NaBr Solid Solutions. *J. Am. Chem. Soc*. **1948**, *70*, 4165−4169.

[33] Wei, S.-H.; Ferreira, L. G.; Zunder, A. First-Principles Calculation of Temperature-Composition Phase Diagrams of Semiconductor Alloys. *Phys. Rev. B* **1989**, *41*, 8240−8269.

[34] Kuznetsov, V. G.; Shkrabkina, M. M. X-ray Diffraction Study of NaH and KH at Temperatures from 20 to 400 °C. *Zh. Struk. Khim*.**1962**, *3*, 553−558.

[35] Mikheeva, V. I.; Shkrabkina, M. M. Solid Solutions in the NaOH-NaH and KOH-KH Systems. *Russ. J. Inorg. Chem.* **1962**, *7*, 1251−1255.

[36] Bleif, H.-J.; Dachs, H. Crystalline Modifications and Structural Phase Transitions of NaOH and NaOD. *Acta. Cryst. A* **1982**, *38*, 470−476.

[37] Douglas, T. B.; Dever, J. L. Anhydrous Sodium Hydroxide: The Heat Content From 0° to 700° C, the Transition Temperature, and the Melting Point. *J. Res. Natl. Bur. Stand*. **1954**, *53*, 81−90.

[38] Sherwood, J. N. The Plastically Crystalline State; *Wiley & Sons: New York*, **1979**.

## III. DENSITY FUNCTIONAL THEORY OF MH–MOH SOLID SOLUBILITY (M = ALKALI) AND EXPERIMENTS IN NaH–NaO

Gang Wang,[†] C. L. Carr,[†] Dongxue Zhao,[†] E. G. Sorte, [‡,||] Tim Ellis-Caleo,[‡] M. S. Conradi,[‡] R. C. Bowman, Jr.,[§] and E. H. Majzoub [*,†]

[†]Center for Nanoscience and Department of Physics and Astronomy, University of Missouri St. Louis, One University Boulevard, St. Louis, Missouri 63121, United States

[‡]Department of Physics, Washington University, One Brookings Drive, Saint Louis, Missouri 63130, United States

[§]RCB Hydrides, LLC, 117 Miami Avenue, Franklin, Ohio 45005, United States

### ABSTRACT

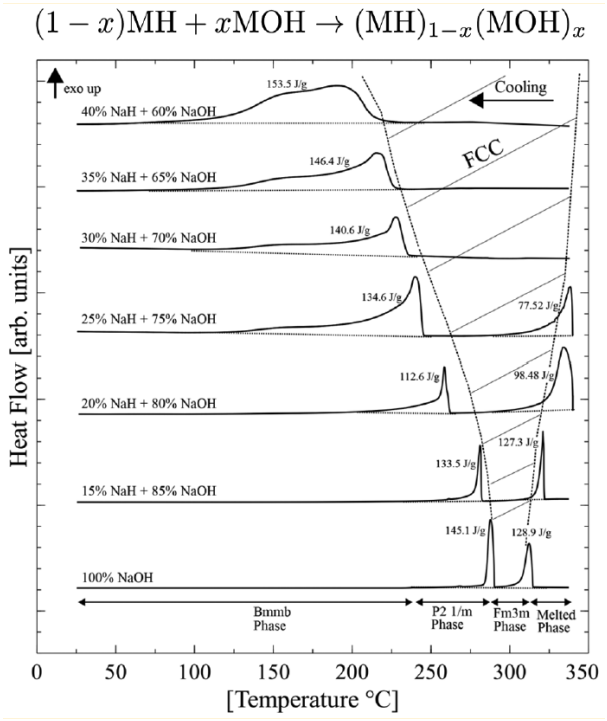


We present first-principles solubility calculations of $H^-/[OH]^-$ mixing in binary alkali metal hydrides MH and their corresponding hydroxides MOH, for M ={Li, Na, K, Rb, Cs}. Solid solubility in the MH−MOH system may play an important role in solid-phase reactions involving the MH system, including for example many aluminum-based

complex hydrides of the alkali metals, such as $NaAlH_4$ and $LiAlH_4$. Our results indicate that the available cell volume for $H^-$ and $OH^-$ groups correlates strongly with mixing, and MOH is soluble in MH for M ={Na, K, and Rb} where available volumes for $H^-$ and $OH^-$ anions differ by less than about 15%, very similar to a Hume−Rothery type rule for intermetallics. The predicted mixing temperatures for the K and Rb systems are lower than for the Na system, in part because of the similarity in MH and MOH primitive cell volumes. Critical temperature diagrams for the formation of solid solution MH−MOH mixtures as a function of MOH concentration are calculated using a free energy minimization in the grand canonical ensemble. Differential scanning calorimetry and in situ X-ray diffraction measurements of the $NaH_{1-x}(OH)_x$ system are presented for a range of compositions ($0.3 \leq x \leq 1.0$). As the temperature is raised, the polymorphic phase transitions present in NaOH occur concomitantly with $H^-/OH^-$ mixing, eventually forming a single-phase cubic structure; the behavior is fully reversible on cooling. Finally, the formation of solid solution MH/MOH reduces the decomposition temperature of $NaH_{1-x}(OH)_x$ to lower temperatures than pure NaH while increasing the stability in the KH and RbH systems.

## INTRODUCTION

Diffusion of hydrogen and the rapid mass transport of metal species are important for many complex anionic hydrogen storage materials. In particular, sodium aluminum hydride ($NaAlH_4$) decomposes in two steps, resulting in phase separated $Na_3AlH_6$ + Al, and NaH + Al, respectively. This system reversibly absorbs hydrogen with the addition of a few mol % of transition metal dopant.[1] While extensive theories of mass transport have been developed, [2,3] they do not consider the effect of impurities such as oxygen/hydroxide that are unavoidable in practical applications. The family of alkali metal alanates that are of interest in the hydrogen storage community also includes $LiAlH_4$, because of its large reversible hydrogen wt %, and $KAlH_4$, which is evidently reversible without the need for a catalyst.[4] Alanate reversibility could be influenced by residual oxygen contamination via faster diffusion and mass transport of M in an MH/MOH solid solution phase. Our results indicate that the similarity in cell volume

available to $H^-$ and $OH^-$ anions in the MH and MOH lattices, respectively, strongly influences the onset of mixing and may provide a partial explanation of this behavior.

The objective of this work is to more fully understand the solid solution formation in alkali metals and alkali metal hydroxides that may be relevant for solid state reactions, including but not limited to metal hydrides. In previous work, we investigated mixing in the NaH/NaOH system, with a focus on the NaH-rich side of the pseudobinary NaH/NaOH phase diagram [5] and demonstrated that thermal activation alone was unable to account for $^1$H NMR line narrowing with increasing temperature in a 10 mol % NaOH sample. Further, differential scanning calorimetry was indicative of a phase transition. This paper presents a comprehensive density functional theory (DFT) investigation of the enthalpy of mixing of MOH in MH where M ={Li, Na, K, Rb, and Cs}. We present these results via the calculation of critical temperatures for the onset of mixing of MH and MOH, at *fixed* MH/MOH *ratios*, i.e., we calculate the onset of mixing for the reaction $(1 - x)\mathrm{MH} + x\mathrm{MOH} \rightarrow \mathrm{MH}_{1-x}(\mathrm{OH})_x$. We make no attempt to calculate the full pseudobinary phase diagram because of the difficulty introduced by the many soft modes that appear in structures containing $OH^-$ groups, where the potential energy surface for $OH^-$ rotations is relatively flat. Because we calculate the enthalpy of mixing at fixed concentration and ignore partially segregated possibilities, e.g., $y\mathrm{MH} + \mathrm{MH}_{1-z}(\mathrm{OH})_z$, our critical temperatures represent lower bounds for the onset of mixing.

In this work, we also present an experimental study of the NaH/NaOH pseudobinary phase diagram over a limited composition range and compare our findings with predictions obtained from the computational study and previous work. In the early studies by Mikheeva et al.,[6] the hydroxide-rich sides of the pseudobinary NaH/NaOH and KH/KOH phase diagrams were experimentally investigated. Their work demonstrated restricted regions of solid solution formation in the NaH/NaOH system. The authors determined there exists two regions of solid solution phases: the $\alpha$ phase solid solution consisting of $H^-$ substitution on $OH^-$ sites in orthorhombic (Bmmb) NaOH and the $\beta$ phase solid solution consisting of $H^-$ substitution on $OH^-$ sites in fcc NaOH. The phase diagram shows the region of the α phase solution forms up to 27 and 32 mol % NaH at room temperature and 200 °C, respectively. The region of the $\beta$ phase solution is shown to exist up to 36 and 75 mol % NaH at 240 and 450 °C respectively. Between the $\alpha$ and $\beta$

regions there is a very small region that contains both $\alpha$ and $\beta$ phase solid solutions. Outside these regions mixtures of $\alpha$ + NaH and $\beta$ + NaH are present where the dividing line is at roughly 225 °C. There is no solubility shown for NaOH on the NaH-rich side of the phase diagram in the Mikheeva work.[6]

Because of its importance in hydrogen storage reactions, we study extensively the hydride-rich side of the phase diagrams, where our computational work shows that a solid solution can form for sample compositions containing less than 41 and 50 mol % hydroxide in the NaH/NaOH and KH/KOH systems, respectively. The extreme reactivity of KOH prevented us from collecting experimental data for this system, and we focused experimentally on the study of the NaH/NaOH system.

The manuscript is organized as follows. In the second section we introduce our computational methods and construction of the solid-solution supercells used in our DFT calculations. In the third section we discuss our experimental methods. The fourth section presents the main results obtained in this work.

## COMPUTATIONAL METHODS

All density functional theory (DFT) calculations were performed using the Vienna ab initio simulation package (VASP).[7,8] Standard projector augmented wave (PAW) pseudopotentials were used along with the PW91[9,10] generalized gradient approximation (GGA) for the exchange correlation. The cutoff energy was 600 eV for all calculations with an electronic convergence criterion of $10^{-6}$ eV. Atomic coordinate and cell parameter relaxations were completed until the forces on the ions were less than 0.005 eV/Å. Frozen phonon calculations were performed in the harmonic approximation using the linear response capability in VASP 5, and the phonon frequencies were used to calculate finite temperature free energies.

Gas-phase energy of hydrogen was calculated by placing one $H_2$ molecule in a 20 × 20 × 20 $Å^3$ cell, using only the Γ point ($k$ = 0). Cubic $Fm\bar{3}m$ 2 × 2 × 2 supercells of MH, M ={Li, Na, K, Rb, and Cs} were chosen to simulate the hydrides. Monkhorst−Pack grids were used for Brillouin zone integration. [11] Supercell sizes and the space groups of the crystal structures are listed in Table S1 (Supporting Information). K-point meshes are

listed in Table S2. To improve the physical accuracy of the calculations, successively larger supercells were chosen to reproduce the experimentally measured entropies.

**MH and MOH Crystal Structures and Construction of Supercells.** Our DFT calculations of the solubility focused on the MH-rich side of the phase diagram; therefore, supercells of mixed MH/MOH were constructed by starting from a 2 × 2 × 2 supercell of cubic MH and substituting oxygen atoms in one of six octahedral positions around the hydrogen atoms, along the coordinate axes, to obtain a composition of $[MH_{1-x}(OH)_x]$. The initial O−H bond length was placed at 0.88 Å. The oxygen atom positions were randomized using a simulated annealing algorithm (SA).[12] The energy functional (cost function) used was the total electrostatic energy:

$$E = \sum_{i \neq j} \frac{e_i e_j}{r_{ij}} \quad (1)$$

where $e_i$ and $e_j$ are the reference charges of elements $i$ and $j$. The idealized reference charges for M, H, and O were +1, +1, and −2, respectively, and $r_{ij}$ is the distance between the elements $i$ and $j$. For the purposes of this SA application, it is not important that the assigned atomic charges be correct. All randomized solid-solution structures were fully relaxed using the conjugate gradient algorithm in VASP. By use of periodic boundary conditions in the SA simulations, the Coulomb interaction was calculated within a radius of one unit cell dimension centered on every atom. Standard SA protocol compares the reference energies of an existing configuration ($E_1$) and a new configuration ($E_2$). All downhill moves are accepted, and uphill moves are accepted with a Boltzmann probability of $e^{-(E_2-E_1)/T}$ if $E_2 > E_1$, where T represents the annealing reference temperature.12 We used an exponential annealing schedule with $T_n = T_i e^{-[(1/N)\ln(T_i/T_f)]n}$ where $T_i = 100$ was the initial temperature parameter and $T_f = 1 \times 10^{-3}$ was the final parameter. We used $N = 30$ temperature steps, where $n$ refers to the $n$th step.

**Solid-Solubility Calculations.** The solubility of MOH in MH where M ={Li, Na, K, Rb, and Cs} can be studied by investigating the reaction

$$(1 - x)MH + xMOH \rightarrow MH_{(1-x)}(OH)_x \quad (2)$$

where $0< x < 1$. The compound $MH_{(1-x)}(OH)_x$ is favorable when the free energy, $F$, of the compound is less than the sum of the free energies of MOH and MH:

$$\Delta F = F\,[MH_{(1-x)}(OH)_x] - x\,F(MOH) - (1-x)\,F(MH) < 0 \quad (3)$$

The standard expression for the Helmholtz free energy of a solid as a function of temperature is given by

$$F = U_0 + \sum_r \left[\frac{1}{2}\hbar\omega_r + k_B T \ln\left(1 - e^{-\frac{\hbar\omega_r}{k_B T}}\right)\right] - TS_{conf.} \quad (4)$$

where $U_0$ is the electronic total energy of a crystal from the geometric optimization using DFT, $k_B$ is Boltzmann's constant, $\omega_r$ values are the (harmonic) phonon frequencies derived via the linear response method in VASP, and $\sum_r (1/2)\hbar\omega_r$ is the zero point energy (ZPE) representing the atomic vibrations at absolute zero. $S_{conf}$ denotes the configurational entropy. Random occupancy of a binary mixture was evaluated using the standard expression

$$S_{conf} = -Nk_B[x\ln(x) + (1-x)\ln(1-x)] \quad (5)$$

with $x = [OH^-]$ and $1 - x = [H^-]$, and $N$ is the number of formula units.

In the solid solubility calculations, the critical soluble temperature ($T_c$) is obtained when $\Delta F(T_c,x) = 0$. As discussed above, we calculate $T_c$ for the case of phase segregation into pure MH + MOH only. The enthalpy change at the critical temperature can be calculated from $dF = dH - TdS = 0$:

$$\Delta H = T\left[S\left(T, MH_{(1-x)}(OH)_x\right) - xS(T, MOH) - (1-x)S(T, MH)\right] \quad (6)$$

The formation of the solid solution is endothermic when $\Delta H > 0$.

We also include in our calculations the decomposition of the MH/MOH mixtures that results in the release of hydrogen gas. In these calculations, the Gibbs' free energy

minimizations were performed using the grand canonical linear programming method (GCLP),[13] assuming a $H_2$ reservoir, to account for decomposition and hydrogen release at $P$ = 1 bar $H_2$. The chemical potential of $H_2$ can be evaluated with the following expression.

$$\mu = U_0 + F_v(T) + F(T,p) \quad (7)$$

Here $U_0$ is the electronic energy of a hydrogen molecule evaluated by the first-principles calculations of a hydrogen molecule in a large volume-conserved cell. $F_v(T)$ is the vibrational free energy. $F(T,p)$ contains the translational and rotational motions, along with the interactions between hydrogen molecules. The last term was taken from the experimental entropy of hydrogen under standard conditions.[14]

**EXPERIMENTAL METHODS**

NaH (95 wt %) was purchased from Sigma-Aldrich and used as received. NaOH (97 wt %) was purchased from Fisher Chemical and was dried at 300 °C under dynamic vacuum for 12 h in order to remove any remaining water. No hydrates were visible in X-ray diffraction or nuclear magnetic resonance measurements after drying.[5] All samples were prepared and handled in an Ar atmosphere glovebox with oxygen and $H_2O$ levels below 1 ppm. All NaH/NaOH samples were hand mixed with mortar and pestle in our glovebox for approximately 5 min prior to calorimetry or X-ray diffraction measurements. All mixtures are given in molar percent.

Differential scanning calorimetry (DSC) was performed on a TA Instruments Q2000 series analyzer. About 6 mg of sample was loaded in an aluminum pan with a hermetically sealed lid in an Ar glovebox. The sample was heated from 25 °C to a maximum of 340 °C and then cooled to 25 °C at a rate of 5 °C/min using flowing nitrogen gas.

The in situ powder X-ray diffraction (XRD) was performed on a Rigaku Ultima IV diffractometer using the standard Bragg−Brentano scattering geometry and Cu $K_\alpha$ radiation. The NaH/NaOH samples were placed in a rectangular aluminum sample holder and sealed with thin adhesive Kapton tape during preparation in the glovebox. The

Kapton tape provides an airtight seal up to about 300 °C. Powder samples were compacted in the sample holder for better thermal transfer than a loose powder would provide. The aluminum XRD sample holder was heated with a Dale 20 W power resistor fastened to the bottom surface. The sample temperature was maintained using an Omega Autotune controller, and the holder temperature was measured with type-K thermocouples. The samples were heated from room temperature up to 260 °C, and the XRD spectra were recorded in roughly 30−50 °C temperature intervals from 22 to 260 °C and again on cooling. For a few of the compositions, the samples were heated a second time to a temperature of 325 °C and cooled. XRD spectra were recorded at 325 °C and again at room temperature. A range from 30° to 70° of $2\theta$ was used for all scans. The step size was 0.02° $2\theta$, with a scanning speed of 1.5°/min.

Attempts were made to investigate the KH/KOH system, but strong reactivity of these samples with our Kapton tape and aluminum sample holders for XRD and DSC prevented the collection of reliable data. Further, it is generally observed that as one goes down the alkali metal group, the more reactive is the metal. Given the high reactivity of our KH/KOH samples with our sample holder materials, we did not attempt experiments with RbH/RbOH.

## RESULTS AND DISCUSSION

Not surprisingly, crystal structures of the alkali hydrides and their hydroxides share many features. The structures of MH for M ={Li, Na, K, Rb, and Cs} all have the $Fm\bar{3}m$ space group.[15] The known structures of the hydroxides tend toward this cubic symmetry at high temperature presumably because of rapid rotation of the $OH^-$ units except for LiOH that remains in $P4/nmm$ up to 473 °C.[16] NaOH exhibits polymorphism starting with the low temperature structure in Bmmb until 241 °C. Between 241 and 295 °C, NaOH has the space group $P2_1/m$, and the structure above 295 °C is $Fm\bar{3}m$.[16] The low temperature structure of KOH is $P2_1/m$ until 244 °C at which point it transforms to $Fm\bar{3}m$.[16] The low temperature structure of RbOH is $Cmc2_1$ until −8 °C and is $P2_1/m$ from −8 to 235 °C. Above 235 °C, it is $Fm\bar{3}m$.[16] The structure of CsOH at temperatures below −39 °C is *Pmnb*, above which it becomes *Bmmb*, transforming to $Fm\bar{3}m$ above 225 °C.[16]

For the purpose of calculating the free energies and critical temperatures of mixing, we use the fully relaxed, ground-state structures obtained at $T$ = 0 K. As mentioned above, DFT relaxation of literature structures for the alkali metal hydroxides often results in symmetry breaking due to the presence of soft modes. In nature, anharmonic effects at finite temperature likely stabilize these modes; recall our calculations treat phonon modes in the harmonic approximation. For example, DFT relaxation of the LiOH supercell using the literature structure in symmetry *P*4/*nmm* will break this symmetry, resulting in a structure with no symmetry (*P*1). Phonon vibrational frequencies calculated for supercells of the remaining hydroxides (NaOH, KOH, RbOH, and CsOH) all contained imaginary modes. The method of mode following[17] was used to attain stable structures for all hydroxides. The resulting space groups are listed in Table S1. The differences in the DFT calculated total energies from these relaxations provide an estimated error of about ±80 °C for the calculated critical temperatures, $T_c$.

**LiH/LiOH System.** The LiH/LiOH system is uninteresting in that any mixture of LiH and LiOH is predicted via our GCLP calculations to decompose with the release of hydrogen gas before formation of a solid solution phase. The mixture of LiH and LiOH is predicted to release $H_2$ through the reaction

$$\mathrm{LiH + LiOH \rightarrow Li_2O + H_2} \tag{8}$$

with an enthalpy change of −18.28 kJ/mol $H_2$ at $T$ = 0 K. Forbidding the reaction in eq 8, the enthalpy of mixing was calculated for the composition $Li_{32}H_{31}OH$, even though the composite crystal is evidently unfavorable against $H_2$ formation. The solid solution would form at 708 °C with an enthalpy of 219 J/g (1.86 kJ/mol reaction), well above the predicted critical temperature for eq 8. Numerous experimental studies are consistent with these findings in that only the LiH, LiOH, $Li_2O$, and $LiOH{\cdot}H_2O$ have been observed for this system under various conditions.[18−23]

**NaH/NaOH System.** The calculated cell volume of cubic NaH is 28.02 Å$^3$/f.u., and the cell volume of stable modefollowed *Bmmb* NaOH (in space group *Cmc*2$_1$) is 30.48 Å$^3$/f.u. Figure 1 shows the DFT-relaxed unit cell volume ratio of $MH_{(1-x)}(OH)_x$ to MH for $0 \leq x \leq 1$. The black circles represent $NaH_{(1-x)}(OH)_x$. The volume increases with

the increase of NaOH concentration ($x$) from NaH to NaOH. This is expected as the crystal shifts from NaH-like to NaOH-like and is consistent with the larger cell volume of pure NaOH.

Figure 2 shows the hydride rich side of the calculated critical temperature diagram for the NaH/NaOH system, which was not explored in Mikheeva's work. Below the green curve is where NaOH and NaH are phase separated. The green curve represents the calculated critical temperatures above which the solid solution is favorable:

$$(1-x)\mathrm{NaH} + x\mathrm{NaOH} \rightarrow \mathrm{NaH}_{(1-x)}(\mathrm{OH})_x \quad (9)$$

Table S3 shows the critical temperature and enthalpy for eq 9 for different NaH/NaOH ratios. The data indicate that formation of the solution is endothermic above the critical temperature and also show that the critical temperature increases with the increase of hydroxide concentration x. The solution is predicted to be stable until x = 0.41, above which the two-phase mixture *decomposes before mixing* according to the following reaction.

$$\mathrm{NaH} + \mathrm{NaOH} \rightarrow \mathrm{Na_2O} + \mathrm{H_2} \quad (10)$$

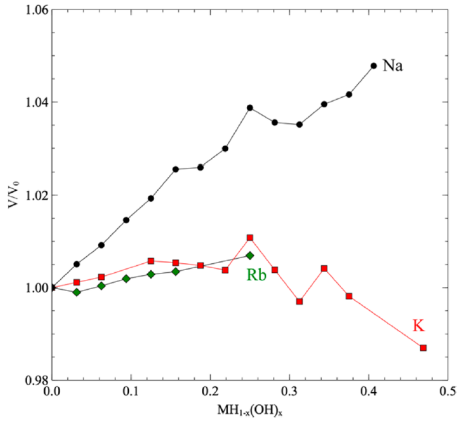


**Figure 1.** Relaxed crystal volume expansions as a function of MOH concentration; M = Na (black circle), K (red square), Rb (green diamond).

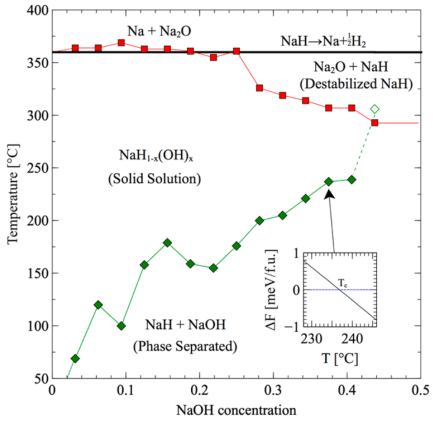


**Figure 2.** Critical temperatures for mixing and decompositions in the NaH/NaOH system: green, critical temperature; red, decomposition of solid solution; black, decomposition of NaH at $P$ = 1 bar of $H_2$. Inset illustrates critical temperature.

This reaction is predicted to occur around 293 °C with an enthalpy of about 59 kJ/mol $H_2$ when $x > 0.41$. In Figure 2, the region between the green and red curves is where only the solid solution exists. The red curve represents the decomposition of the solid solution. At concentrations below about $x = 0.25$, the solid solution decomposes at essentially the same temperature as that of pure NaH, represented by the black line. At concentrations larger than $x = 0.25$, the decomposition temperature of the solid solution decreases, forming a new region containing $Na_2O$ and NaH. This region extends above the red curve up to the black line that represents the decomposition of pure NaH. Solid solution decomposition occurs as

$$NaH_{(1-x)}(OH)_x \rightarrow (1\text{-}2x)NaH + xNa_2O + xH_2 \qquad (11)$$

Reactions such as the mixing and decomposition shown in Figure 2 represent the free energy only and ignore kinetics. The free energy critical temperatures are a lower bound; if the reaction had no kinetic barrier, it would proceed as soon as thermodynamically feasible. In addition, the physical accuracy of DFT reaction enthalpies provides only rough estimates of the critical solution temperatures. As the decomposition curve (red in Figure 2) and the solid-solution/phase-segregation curve (green in Figure 2) approach each other at large $OH^-$ concentrations, the actual physical

behavior will be strongly influenced by the kinetic barriers. Our experiments show that the solid solution is evidently stable to higher temperatures at compositions $x > 0.44$ in contrast to our DFT calculations which show decomposition above $x = 0.44$, before formation of the solid solution.

Perhaps most interestingly, for concentrations above about $x = 0.25$, the solid solution has a lower temperature of decomposition and hydrogen desorption than does pure NaH as shown in Table S3. The DFT-calculated decomposition of pure NaH is around 360 °C with an enthalpy of 91 kJ/mol $H_2$:

$$2\ NaH \rightarrow 2\ Na + H_2 \tag{12}$$

*NaOH-Rich Compositions.* The NaOH-rich side of the critical temperature figure was investigated using an 8 formula unit cell in space group $P2_1/m$ for NaOH, for compositions $Na_8(OH)_7H$, $Na_8(OH)_6H_2$, and $Na_8(OH)_5H_3$. These cells were constructed by removing 1, 2, and 3 oxygen atoms from the $P2_1/m$ NaOH structure, since the mixing takes place at higher temperatures where NaOH is in the $P2_1/m$ space group. The mixed structures were optimized keeping the $P2_1/m$ symmetry and cell volume fixed but allowing the atomic coordinates to relax. The results (not shown) indicate that our selected mixed compounds $Na_8(OH)_7H$ and $Na_8(OH)_6H_2$ are favorable at and above −246 and −31 °C, respectively, but find that $Na_8(OH)_5H_3$ is unfavorable. This means that NaOH and NaH prefer to phase-separate at low temperature at a NaH content between 25 and 38 mol %, in agreement with Mikheeva et al.[6]. The enthalpy changes calculated at the experimentally observed temperatures (see DSC data) were calculated as 81 J/g at 275 °C for $Na_8(OH)_7H$ (12.5 mol % NaH) which is considerably lower than our 15 mol % NaH experimental value of 133.5 J/g determined from DSC. This is due to the experimental value being a combination of the solution enthalpy and the phase transition of NaOH from $Fm\bar{3}m$ to $P2_1/m$. However, we find an enthalpy of 142 J/g at 230 °C for $Na_8(OH)_6H_2$ in excellent agreement with our present DSC experimental value of 134.6 J/g for 25 mol % NaH (see below).

**KH/KOH System.** The red squares in Figure 1 show the DFT-relaxed unit cell volume expansion for $KH_{(1-x)}(OH)_x$, $0 \leq x \leq 1$. The calculated volume of cubic KH is

45.97 Å$^3$/f.u., while the volume of our stable KOH structure is 42.59 Å$^3$/f.u. The calculated volume of KOH in the experimental structure, space group $P2_1/m$, is 47.10 Å$^3$/f.u., and the calculated volume of KOH in the experimental structure in space group $Fm\bar{3}m$ is 46.23 Å$^3$/f.u. The volumes are similar; however, the volume of the mode-followed stable KOH structure is 7.3% smaller than the volume of KH. The calculated cell volumes in the solid solution phase hold roughly steady for KOH concentrations up to about 25 mol % and then begin to decrease.

Mixing in the potassium system is more favorable than in the sodium system, as the predicted temperatures for solution formation and the magnitude of the endothermic enthalpy changes are lower, as shown in Figure 3. The green curve represents the calculated critical temperature of solution formation, with the reaction

$$(1\text{-}x)\mathrm{KH} + x\mathrm{KOH} \rightarrow \mathrm{KH}_{(1\text{-}x)}(\mathrm{OH})_x \quad (13)$$

Table S4 contains the critical temperature of solution formation and their corresponding enthalpy changes as well as the decomposition temperature of the solid solution. Similar to the sodium system, the critical temperature increases as the concentration of KOH is increased. The calculated critical temperatures are quite low, ranging from below 0 °C up to 70 °C. However, because of a lack of kinetic barriers in our calculations, experimentally observed mixing may take place at higher temperatures. The black line represents the DFTcalculated decomposition temperature for pure KH with an enthalpy of 91 kJ/mol $H_2$.

$$2\mathrm{KH} \rightarrow 2\mathrm{K} + \mathrm{H}_2 \quad (14)$$

In contrast to the sodium system, upon mixing of KH/KOH, the solution is stable above the decomposition temperature of pure KH. The red curve is the predicted decomposition of the solution:

$$\mathrm{KH}_{(1\text{-}x)}(\mathrm{OH})_x \rightarrow (1\text{-}x)\mathrm{K} + x\mathrm{KOH} + \frac{(1-x)}{2}\mathrm{H}_2 \quad (15)$$

Evidently, KOH stabilizes KH in the entire range we investigated, and the stabilization is strengthened as the concentration of KOH increases.

**RbH/RbOH System.** The green diamonds in Figure 1 indicate the volume expansion of $RbH_{1-x}(OH)_x$ supercells as a function of $OH^-$ concentration ($x$). The volume increases with the increase of RbOH concentration. Figure 4 shows the critical temperatures for mixing in the RbH/RbOH system, which is similar to KH/KOH system. The decomposition temperature of the solution is higher than the pure hydride decomposition temperature of 339 °C. Therefore, similar to the potassium system, formation of the solid solution phase stabilizes RbH to higher temperature.

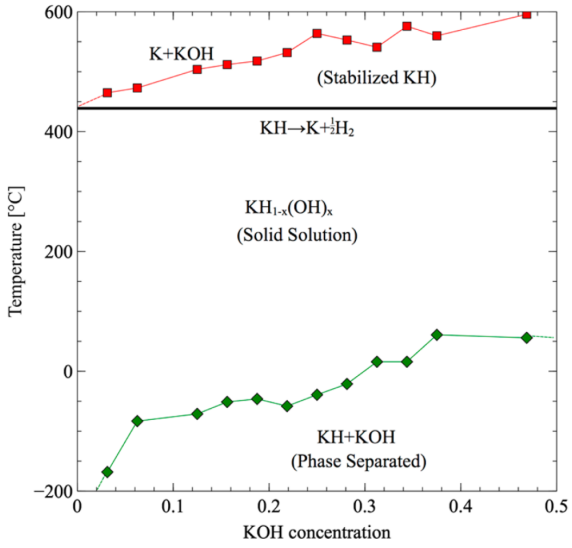


**Figure 3.** Critical temperatures for mixing and decompositions in the KH/KOH system: green, critical temperature; red, decomposition of solid solution; black, decomposition of KH at $P$ = 1 bar of $H_2$.

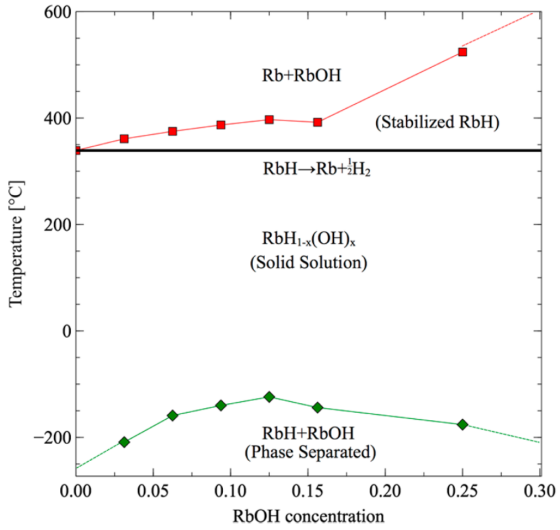


**Figure 4.** Critical temperatures for mixing and decompositions in the RbH/RbOH system: green, critical temperature; red, decomposition of solid solution; black, decomposition of RbH.

Table S5 contains the solid solution critical temperatures and the corresponding enthalpies as well as the decomposition of the solid solution. The critical temperature and enthalpy of mixing are very low, indicating that the solution is even more favorable than in the Na and K systems.

**CsH/CsOH System.** The cesium system, like lithium, does not indicate the formation of a solid solution phase. CsH decomposes before the mixture can form a solution:

$$2\mathrm{CsH} \rightarrow 2\ \mathrm{Cs} + \mathrm{H_2} \qquad (16)$$

The decomposition was predicted to occur at 423 °C, and it is an endothermic reaction, the enthalpy of which is 77 kJ/mol $H_2$.

**Cell Volumes in the MH/MOH System.** Table 1 shows the available anion volumes and cation radii for the alkali monohydrides or hydroxides. All the structures of hydrides are $Fm\bar{3}m$, and the structures of MOH ($V_{\mathrm{cal}}$) are taken from the mode-followed structures of Bmmb MOH, which are $P1$ for LiOH, KOH, and CsOH, $CmC2_1$ for NaOH, and $Pc$ for RbOH. The available anionic volumes were derived as $V_{\mathrm{cal}} = V_{\mathrm{unitcell}} - V_{\mathrm{cation}}$,

from our calculated volumes of the crystal minus the corresponding cation volume. Only a small portion of the resulting volume is physically available to the anion. However, it provides a reliable metric for the ability of the MH and MOH to form a solid solution phase. The table illustrates that the soluble systems (Na, K, and Rb) have similar $H^-$ and $OH^-$ available anionic volumes, while the insoluble systems (Li and Cs) have large differences in their respective available anionic volumes (see column $\Delta V_{cal}$). These findings are somewhat analogous to the Hume−Rothery rules where valence and relative size determine metal−metal solid solution mixing tendencies.

Table 1. Available anion volumes for $H^-$ and $OH^-$ determined from standard cation radii in MH and MOH systems[a].

| metal | *r*[cation] (Å) | $V_{cal}[H^-]$ (Å$^3$) | $V_{cal}[OH^-]$ (Å$^3$) | $DV_{cal}$ (%) |
|---|---|---|---|---|
| Li | 0.68 | 14.79 | 27.14 | 83.50 |
| Na | 0.98 | 24.19 | 26.66 | 10.21 |
| K | 1.33 | 36.12 | 32.74 | -9.36 |
| Rb | 1.48 | 35.92 | 35.53 | -1.09 |
| Cs | 1.67 | 46.75 | 38.66 | -17.30 |

[a]Cation radii were taken from Kittel.[24] $V_{cal}$ is the calculated volume for the anions and is described in the text.

**DSC and in Situ XRD Results for the NaH/NaOH System.** Differential scanning calorimetry (DSC) and in situ X-ray diffraction were used to investigate mixing in the NaH/NaOH system. Figure 5 shows DSC scans over a range of molar ratios of NaH/NaOH. These samples were first heated up to 340 °C, and the DSC data were collected during the cooling process. In agreement with Mikheeva's phase diagram, the melting point of the mixture moves to higher temperature with increasing NaH content. At the same time, the two phase transitions of NaOH move to lower temperature and merge together with the NaH/NaOH phase-separation process. For the 40 mol % NaH +

60 mol % NaOH composition, this process takes place over a wide temperature range from 240 to 60 °C. Calculated enthalpies on the NaOH-rich side of the phase diagram are in agreement with the DSC data as we indicated in the paragraph above on NaOH-rich compositions.

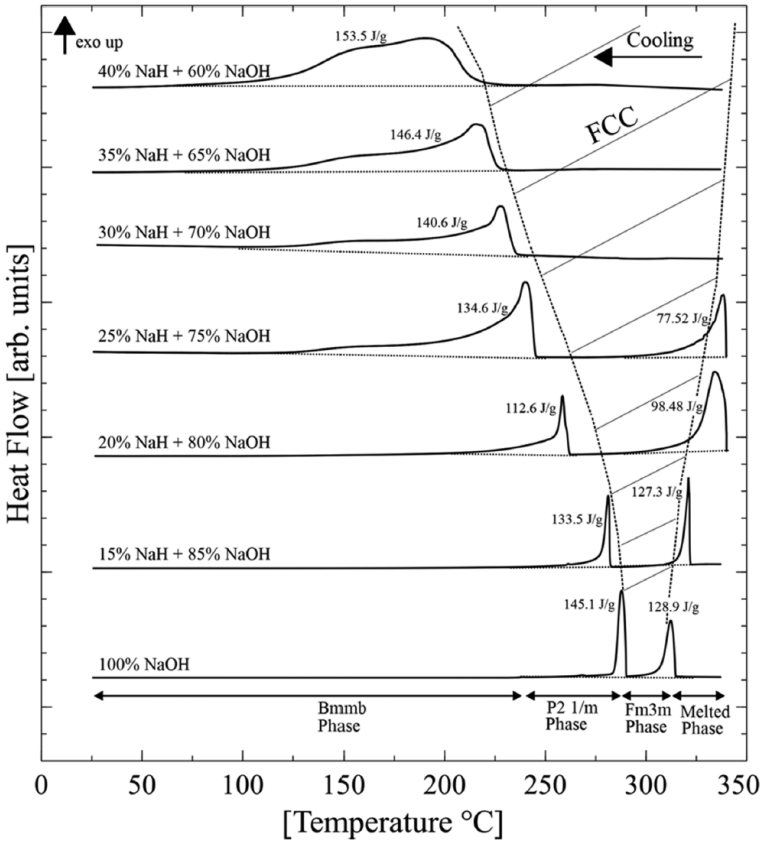


**Figure 5.** Differential Scanning Calorimetry (DSC) data of cooling scans. The horizontal dotted lines are guides for the eyes, serving as baselines. The hatched region indicates the approximate boundary of the cubic phase solid solution.

To investigate the dissolution and phase separation process, DSC was performed on a 70 mol % NaH + 30 mol % NaOH sample. The sample was first heated up to 330 °C in order to premelt the mixture. The data were recorded during sample heating up from 25 to 300 °C and then again upon cooling down to 25 °C at a ramp rate of 5 °C/min for multiple cycles. During the heating and cooling cycles, substantial, repeatable thermal activity occurred around 170 °C as presented in Figure 6. The heating (bottom) curves

show an endothermic peak, and the cooling (top) curves show an exothermic peak, which would be as expected for a reversible phase transition. The enthalpy of the reaction was calculated by integrating under the endothermic or exothermic peaks and was roughly 70 J/g at this composition.

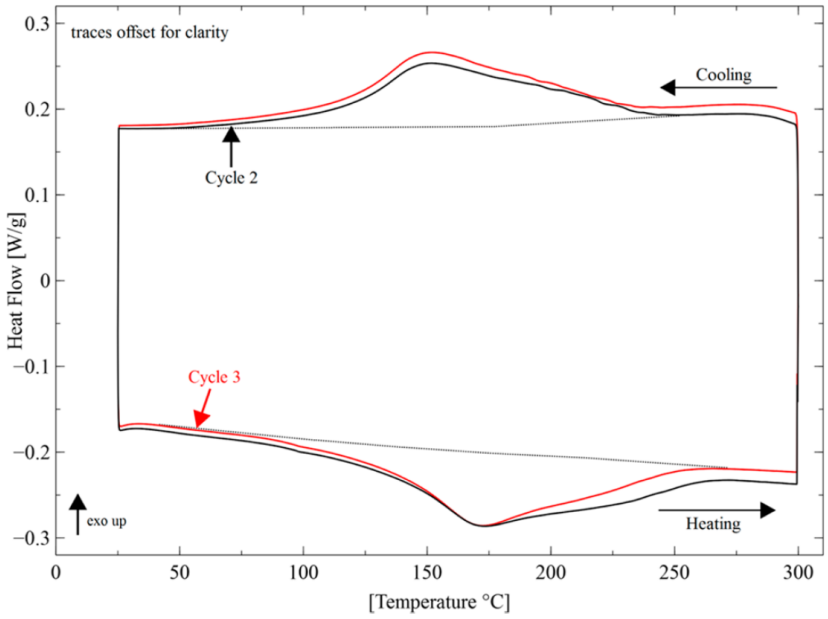


**Figure 6.** Differential Scanning Calorimetry (DSC) data for 70 mol % NaH + 30 mol % NaOH. The first cycle (not shown) was heated to 330 °C to premelt the mixture. The subsequent cycles below the melting temperature of NaOH show the reversible behavior. The dotted "baselines" are a guide for the eyes.

In situ X-ray diffraction was performed on multiple NaH/NaOH samples of differing compositions to experimentally investigate the mixing process in the NaH/NaOH system. Figure 7 shows the heating and cooling process of a 40 mol % NaH + 60 mol % NaOH sample heated up to 260 °C. At 260 °C the sample is almost completely mixed into a single fcc phase solid solution. As the sample cools, the fcc phase solid solution is still present at 180 °C (but shifted to higher angle), but some of the solid solution has now phase separated into *Bmmb* phase NaOH and NaH. As the sample reaches room temperature, NaH and NaOH are mostly phase separated.

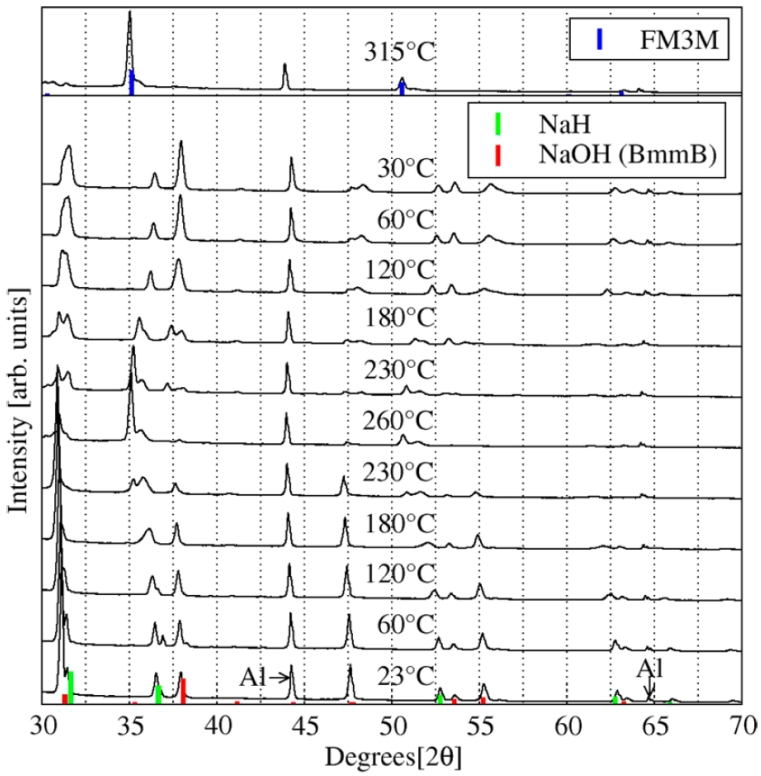


**Figure 7.** In situ X-ray diffraction data of the heating and cooling process for 40 mol % NaH + 60 mol % NaOH sample. The first scan is indicated at 23 °C, and the last scan is indicated at 30 °C. Vertical guidelines (dotted lines) are given to emphasize the peak shifts. The marked Al peaks were generated by the aluminum sample holder.

Heating and cooling the samples during subsequent cycles showed the same repeatable behavior noted in the DSC measurements. At 315 °C (top panel in Figure 7) the sample *completely mixed* into an fcc structure solid solution. Similar results were obtained for compositions of 90, 70, 50, and 25 mol % NaH, respectively. These results suggest necessary modifications to the phase diagram as presented in Mikheeva's work. The region of fcc $\beta$ solid solutions should be extended to higher NaH concentrations at temperatures of >260 °C to accommodate hydride rich compositions that continue to form solid solutions. Further, the region where $\alpha$ and $\beta$ solid solutions exist simultaneously shown in Mikheeva's phase diagram should possibly be extended to include higher NaH concentrations, as the X-ray diffraction data clearly show the existence of the two phases for concentrations outside the allowed region in Mikheeva's

diagram. However, sluggish kinetics at lower temperature may be responsible for incomplete phase separation.

The NaH lattice parameters were extracted from the in situ X-ray diffraction data by implementing full pattern Rietveld refinement from the general structure analysis system (GSAS).[25,26] The NaH lattice expansion and unit cell volume expansion of NaH in the 40 mol % NaH + 60 mol % NaOH sample are compared to that of pure NaH in Figure 8. The comparison shows that NaH in the 40 mol % NaH + 60 mol % NaOH sample has a much larger lattice expansion than pure NaH when heated using the same process. Also, the lattice expansion is not linear. The two-point coefficients of linear expansion, calculated using room temperature and the highest temperature point, for pure NaH and NaH in the 40 mol % NaH + 60 mol % NaOH sample are $37 \times 10^{-6}$/°C and $72 \times 10^{-6}$/°C, respectively. The massive volume expansion of the NaH in the 40 mol % NaH + 60 mol % NaOH sample is evidently due to the formation of solid solution on heating.

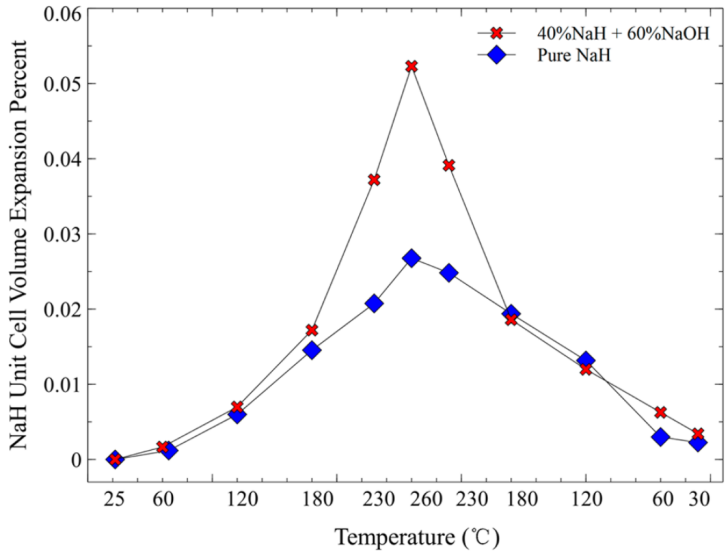


**Figure 8.** Cell volumes via XRD for pure NaH and 40 mol % NaH + 60 mol % NaOH mixture as a function of temperature during a heating and cooling cycle between 25 and 260 °C.

## CONCLUSIONS

The formation of a solid solution in MH/MOH mixtures is governed by the volume difference available for $H^-$ and $OH^-$ anions in their parent phases of MH and MOH, respectively. Mixing occurs when volume differences are less than about 15% with lower critical temperatures for smaller volume differences. Small additions of hydroxide ion in the KH and RbH systems stabilize these hydrides, and the mixtures decompose at temperatures above the pure hydride decomposition temperature. In contrast, small hydroxide addition to NaH tends to lower the decomposition temperature of the mixture. There is no predicted solid solution in the LiH/LiOH and CsH/CsOH systems due to decomposition before mixing. When solid solution formation occurs in the NaH/NaOH system, the phase transitions in NaOH are concomitant with mixing and the high temperature structure is a single phase fcc before melting. This combination of phase transitions and mixing is fully reversible on cooling.

## SUPPORTING INFORMATION

Table S1. Unit cell dimensions and space group symmetries for all structures used in this work.

| Material | *a* (Å) | *b* (Å) | *c* (Å) | *a* | *b* | *g* | *V* (Å$^3$) | Space Group Before Relaxation | Space Group After Relaxation | f.u. |
|---|---|---|---|---|---|---|---|---|---|---|
| $H_2$ | 20 | 20 | 20 | 90 | 90 | 90 | - | - | - | 1 |
| LiH | 8.02 | 8.02 | 8.02 | 90 | 90 | 90 | 515.35 | $Fm\bar{3}m$ | $Fm\bar{3}m$ | 32 |
| LiOH | 7.14 | 7.14 | 8.97 | 89.97 | 86.53 | 93.47 | 455.35 | *P*1 | *P*1 | 16 |
| $Li_2O$ | 4.63 | 4.63 | 4.63 | 90 | 90 | 90 | 99.4 | *P*4*mm* | *P*4*mm* | 4 |
| Na | 8.41 | 8.41 | 8.41 | 90 | 90 | 90 | 594.19 | $Im\bar{3}m$ | $Im\bar{3}m$ | 16 |
| NaH | 9.64 | 9.64 | 9.64 | 90 | 90 | 90 | 896.57 | $Fm\bar{3}m$ | $Fm\bar{3}m$ | 32 |
| NaOH | 6.98 | 6.78 | 20.63 | 90 | 90 | 90 | 975.43 | *Bmmb* | $Cmc2_1$ | 32 |
| $Na_2O$ | 5.56 | 5.56 | 5.56 | 90 | 90 | 90 | 172.09 | $Fm\bar{3}m$ | $Fm\bar{3}m$ | 4 |
| K | 10.55 | 10.55 | 10.55 | 90 | 90 | 90 | 1175.39 | $Im\bar{3}m$ | $Im\bar{3}m$ | 16 |
| KH | 11.37 | 11.37 | 11.37 | 90 | 90 | 90 | 1471.19 | $Fm\bar{3}m$ | $Fm\bar{3}m$ | 32 |
| KOH | 8.01 | 7.98 | 21.33 | 90 | 90 | 90 | 1362.97 | *Bmmb* | *P*1 | 32 |
| Rb | 11.33 | 11.33 | 11.33 | 90 | 90 | 90 | 1453.86 | $Im\bar{3}m$ | $Im\bar{3}m$ | 16 |
| RbH | 12.07 | 12.07 | 12.07 | 90 | 90 | 90 | 1759.35 | $Fm\bar{3}m$ | $Fm\bar{3}m$ | 32 |
| RbOH | 8.42 | 8.46 | 22.08 | 90 | 90.08 | 90 | 1571.43 | *Bmmb* | *Pc* | 32 |
| Cs | 12.28 | 12.28 | 12.28 | 90 | 90 | 90 | 1851.64 | $Im\bar{3}m$ | $Im\bar{3}m$ | 16 |

Table S1. Unit cell dimensions and space group symmetries for all structures used in this work (cont.)

| Material | *a* (Å) | *b* (Å) | *c* (Å) | *a* | *b* | *g* | *V* (Å$^3$) | Space Group Before Relaxation | Space Group After Relaxation | f.u. |
|---|---|---|---|---|---|---|---|---|---|---|
| CsH | 12.85 | 12.85 | 12.85 | 90 | 90 | 90 | 2120.39 | $Fm\bar{3}m$ | $Fm\bar{3}m$ | 32 |
| $Li_{32}H_{31}OH$ | 8.06 | 8.06 | 8.06 | 90.3 | 90.3 | 90.3 | 523.02 | *P*1 | *R*3*m* | 32 |
| $Na_{32}H_{31}OH$ | 9.66 | 9.66 | 9.66 | 90.3 | 90.3 | 90.3 | 901.11 | *P*1 | *P*1 | 1 |
| $Na_{32}H_{30}(OH)_2$ | 9.67 | 9.67 | 9.67 | 90.61 | 90.61 | 90.61 | 904.8 | *P*1 | *P*1 | 1 |
| $Na_{32}H_{29}(OH)_3$ | 9.72 | 9.68 | 9.68 | 91 | 91 | 91 | 909.67 | *P*1 | *P*1 | 1 |
| $Na_{32}H_{28}(OH)_4$ | 9.71 | 9.69 | 9.71 | 90.25 | 91.6 | 90.25 | 913.87 | *P*1 | *P*1 | 1 |
| $Na_{32}H_{27}(OH)_5$ | 9.72 | 9.72 | 9.72 | 91.54 | 91.54 | 91.54 | 919.5 | *P*1 | *P*1 | 1 |
| $Na_{32}H_{26}(OH)_6$ | 9.65 | 9.77 | 9.76 | 90.28 | 90.36 | 92.17 | 919.83 | *P*1 | *P*1 | 1 |
| $Na_{32}H_{25}(OH)_7$ | 9.69 | 9.76 | 9.78 | 90.43 | 91.25 | 92.02 | 923.4 | *P*1 | *P*1 | 1 |
| $Na_{32}H_{24}(OH)_8$ | 9.71 | 9.71 | 9.71 | 92.34 | 92.34 | 92.34 | 931.31 | *P*1 | *P*1 | 1 |
| $Na_{32}H_{23}(OH)_9$ | 9.72 | 9.75 | 9.82 | 91.27 | 91.49 | 92.84 | 928.46 | *P*1 | *P*1 | 1 |
| $Na_{32}H_{22}(OH)_{10}$ | 9.87 | 9.73 | 9.71 | 94.3 | 92.87 | 89.78 | 928.06 | *P*1 | *P*1 | 1 |
| $Na_{32}H_{21}(OH)_{11}$ | 9.77 | 9.76 | 9.81 | 91.9 | 92.41 | 92.71 | 932 | *P*1 | *P*1 | 1 |
| $Na_{32}H_{20}(OH)_{12}$ | 9.78 | 9.87 | 9.72 | 94.99 | 90.47 | 92.7 | 933.87 | *P*1 | *P*1 | 1 |
| $Na_{32}H_{19}(OH)_{13}$ | 9.76 | 9.83 | 9.84 | 92.77 | 91.89 | 93.53 | 939.43 | *P*1 | *P*1 | 1 |
| $K_{32}H_{31}OH$ | 11.38 | 11.38 | 11.38 | 90.27 | 90.27 | 90.27 | 1472.88 | *P*1 | *R*3*m* | 1 |
| $K_{32}H_{30}(OH)_2$ | 11.38 | 11.38 | 11.38 | 90.55 | 90.55 | 90.55 | 1474.56 | *P*1 | *R*3*m* | 1 |
| $K_{32}H_{28}(OH)_4$ | 11.41 | 11.37 | 11.41 | 90.21 | 91.44 | 90.21 | 1479.67 | *P*1 | *Cm* | 1 |
| $K_{32}H_{27}(OH)_5$ | 11.39 | 11.39 | 11.39 | 90.49 | 90.49 | 90.49 | 1479.11 | *P*1 | $C3_4$ | 1 |
| $K_{32}H_{26}(OH)_6$ | 11.33 | 11.43 | 11.42 | 91.79 | 90.37 | 90.29 | 1478.24 | *P*1 | *P*1 | 1 |
| $K_{32}H_{25}(OH)_7$ | 11.36 | 11.4 | 11.41 | 91.66 | 90.93 | 90.31 | 1476.77 | *P*1 | *P*1 | 1 |
| $K_{32}H_{24}(OH)_8$ | 11.42 | 11.42 | 11.42 | 92.09 | 92.09 | 92.09 | 1487.08 | *P*1 | *P*1 | 1 |
| $K_{32}H_{23}(OH)_9$ | 11.36 | 11.38 | 11.43 | 92.31 | 91.14 | 91.02 | 1476.85 | *P*1 | *P*1 | 1 |
| $K_{32}H_{22}(OH)_{10}$ | 11.42 | 11.36 | 11.35 | 89.74 | 92.51 | 93.86 | 1466.77 | *P*1 | *P*1 | 1 |
| $K_{32}H_{21}(OH)_{11}$ | 11.4 | 11.37 | 11.41 | 92.28 | 91.82 | 91.6 | 1477.31 | *P*1 | *P*1 | 1 |
| $K_{32}H_{20}(OH)_{12}$ | 11.36 | 11.45 | 11.35 | 93.02 | 89.73 | 94.55 | 1468.47 | *P*1 | *P*1 | 1 |
| $K_{32}H_{19}(OH)_{15}$ | 11.38 | 11.43 | 11.28 | 89.78 | 87.53 | 97.98 | 1452.06 | *P*1 | *P*1 | 1 |
| $Rb_{32}H_{31}OH$ | 12.07 | 12.07 | 12.07 | 90.24 | 90.24 | 90.24 | 1757.58 | *P*1 | *R*3*m* | 1 |
| $Rb_{32}H_{30}(OH)_2$ | 12.07 | 12.07 | 12.07 | 90.48 | 90.48 | 90.48 | 1760.02 | *P*1 | *R*3*m* | 1 |
| $Rb_{32}H_{29}(OH)_3$ | 12.14 | 12.05 | 12.05 | 90.38 | 90.79 | 90.79 | 1762.75 | *P*1 | *Cm* | 1 |
| $Rb_{32}H_{28}(OH)_4$ | 12.1 | 12.05 | 12.1 | 90.17 | 91.25 | 90.17 | 1764.42 | *P*1 | *Cm* | 1 |
| $Rb_{32}H_{27}(OH)_5$ | 12.09 | 12.09 | 12.09 | 90.4 | 90.4 | 90.4 | 1765.44 | *P*1 | *R*3 | 1 |
| $Rb_{32}H_{24}(OH)_8$ | 12.11 | 12.11 | 12.11 | 91.89 | 91.89 | 91.89 | 1771.55 | *P*1 | *P*1 | 1 |

Table S2. K-point meshes, total energies, vibrational energies and entropies for all structures.

| Material | k-point | $U_E$ (eV) | ZPE (eV) | $S_{conf}$ (eV/K) | $S_c$ (J/mol/K) | $S_e$ (J/mol/K) |
|---|---|---|---|---|---|---|
| $H_2$ | 2x2x2 | -6.80 | 0.27 | - | 130.70 | 130.70 |
| LiH | 2x2x2 | -197.66 | 7.16 | - | 17.78 | 24.70 |
| LiOH | 2x2x2 | -240.41 | 6.91 | - | 39.98 | 42.81 |
| $Li_2O$ | 4x4x4 | -57.75 | 0.89 | - | 33.88 | 37.90 |
| Na | 4x4x4 | -20.89 | 0.25 | - | 45.04 | 51.00 |
| NaH | 2x2x2 | -164.94 | 5.09 | - | 37.02 | 40.00 |
| NaOH | 2x2x2 | -441.13 | 12.56 | - | 58.00 | 64.46 |
| $Na_2O$ | 6x6x6 | -45.66 | 0.49 | - | 68.46 | 73.00 |
| K | 4x4x4 | -16.67 | 0.19 | - | 50.23 | 64.20 |
| KH | 2x2x2 | -156.25 | 4.04 | - | 47.61 | 66.90 |
| KOH | 2x2x2 | -431.45 | 11.98 | - | 70.86 | 79.00 |
| Rb | 2x2x2 | -14.87 | 0.11 | - | 63.35 | 69.50 |
| RbH | 2x2x2 | -150.16 | 3.49 | - | 61.02 | - |
| RbOH | 2x2x2 | -424.17 | 11.52 | - | 119.32 | 84.10 |
| Cs | 2x2x2 | -13.79 | 0.08 | - | 70.18 | 82.80 |
| CsH | 2x2x2 | -147.85 | 3.06 | - | 75.00 | - |
| $Li_{32}H_{31}OH$ | 2x2x2 | -205.86 | 7.28 | - | 20.18 | - |
| $Na_{32}H_{31}OH$ | 2x2x2 | -173.35 | 5.25 | 0.00038 | 39.18 | - |
| $Na_{32}H_{30}(OH)_2$ | 2x2x2 | -181.77 | 5.46 | 0.00064 | 41.13 | - |
| $Na_{32}H_{29}(OH)_3$ | 2x2x2 | -190.20 | 5.65 | 0.00086 | 43.41 | - |
| $Na_{32}H_{28}(OH)_4$ | 2x2x2 | -198.66 | 5.86 | 0.00104 | 44.45 | - |
| $Na_{32}H_{27}(OH)_5$ | 2x2x2 | -207.01 | 6.05 | 0.00120 | 46.68 | - |
| $Na_{32}H_{26}(OH)_6$ | 2x2x2 | -215.71 | 6.29 | 0.00133 | 47.14 | - |
| $Na_{32}H_{25}(OH)_7$ | 2x2x2 | -224.27 | 6.50 | 0.00145 | 48.22 | - |
| $Na_{32}H_{24}(OH)_8$ | 2x2x2 | -232.44 | 6.65 | 0.00155 | 51.33 | - |
| $Na_{32}H_{23}(OH)_9$ | 2x2x2 | -241.33 | 6.97 | 0.00164 | 50.23 | - |

Table S2. K-point meshes, total energies, vibrational energies and entropies for all structures (cont.).

| Material | k-point | $U_E$ (eV) | ZPE (eV) | $S_{conf}$ (eV/K) | $S_c$ (J/mol/K) | $S_e$ (J/mol/K) |
|---|---|---|---|---|---|---|
| $Na_{32}H_{22}(OH)_{10}$ | 2x2x2 | -249.98 | 7.22 | 0.00171 | 50.73 | - |
| $Na_{32}H_{21}(OH)_{11}$ | 2x2x2 | -258.43 | 7.47 | 0.00177 | 52.38 | - |
| $Na_{32}H_{20}(OH)_{12}$ | 2x2x2 | -266.99 | 7.70 | 0.00182 | 53.17 | - |
| $Na_{32}H_{19}(OH)_{13}$ | 2x2x2 | -275.55 | 7.89 | 0.00186 | 54.15 | - |
| $K_{32}H_{31}OH$ | 2x2x2 | -164.70 | 4.19 | 0.00038 | 1626.16 | - |
| $K_{32}H_{30}(OH)_2$ | 2x2x2 | -173.16 | 4.41 | 0.00064 | 1681.41 | - |
| $K_{32}H_{28}(OH)_4$ | 2x2x2 | -190.13 | 4.82 | 0.00104 | 1805.78 | - |
| $K_{32}H_{27}(OH)_5$ | 2x2x2 | -198.64 | 5.05 | 0.00120 | 1846.11 | - |
| $K_{32}H_{26}(OH)_6$ | 2x2x2 | -207.20 | 5.27 | 0.00133 | 1877.75 | - |
| $K_{32}H_{25}(OH)_7$ | 2x2x2 | -215.77 | 5.50 | 0.00145 | 1919.05 | - |
| $K_{32}H_{24}(OH)_8$ | 2x2x2 | -224.14 | 5.66 | 0.00155 | 1999.59 | - |
| $K_{32}H_{23}(OH)_9$ | 2x2x2 | -232.78 | 5.95 | 0.00164 | 1996.80 | - |
| $K_{32}H_{22}(OH)_{10}$ | 2x2x2 | -241.35 | 6.24 | 0.00171 | 2003.50 | - |
| $K_{32}H_{21}(OH)_{11}$ | 2x2x2 | -249.77 | 6.41 | 0.00177 | 2073.20 | - |
| $K_{32}H_{20}(OH)_{12}$ | 2x2x2 | -258.31 | 6.69 | 0.00182 | 2078.82 | - |
| $K_{32}H_{19}(OH)_{15}$ | 2x2x2 | -284.11 | 7.43 | 0.00191 | 2151.89 | - |
| $Rb_{32}H_{31}OH$ | 2x2x2 | -158.16 | 3.67 | 0.00038 | 2054.21 | - |
| $Rb_{32}H_{30}(OH)_2$ | 2x2x2 | -167.05 | 3.88 | 0.00064 | 2126.15 | - |
| $Rb_{32}H_{29}(OH)_3$ | 2x2x2 | -175.54 | 4.07 | 0.00086 | 2189.45 | - |
| $Rb_{32}H_{28}(OH)_4$ | 2x2x2 | -184.01 | 4.28 | 0.00104 | 2242.71 | - |
| $Rb_{32}H_{27}(OH)_5$ | 2x2x2 | -192.50 | 4.50 | 0.00120 | 2303.77 | - |
| $Rb_{32}H_{24}(OH)_8$ | 2x2x2 | -217.98 | 5.10 | 0.00155 | 2527.74 | - |

Table S3. The solution temperatures, decomposition temperatures and enthalpies for the NaH/NaOH system.

| Material | $T_c$ (°C) | D$H_1$ (J/g) | $T_d$ (°C) |
|---|---|---|---|
| $Na_{32}H_{31}OH$ | 69 | 22 | 364 |
| $Na_{32}H_{30}(OH)_2$ | 120 | 46 | 364 |
| $Na_{32}H_{29}(OH)_3$ | 100 | 67 | 369 |
| $Na_{32}H_{28}(OH)_4$ | 158 | 84 | 363 |
| $Na_{32}H_{27}(OH)_5$ | 179 | 114 | 363 |
| $Na_{32}H_{26}(OH)_6$ | 159 | 104 | 361 |
| $Na_{32}H_{25}(OH)_7$ | 155 | 108 | 355 |
| $Na_{32}H_{24}(OH)_8$ | 176 | 153 | 361 |
| $Na_{32}H_{23}(OH)_9$ | 200 | 128 | 326 |
| $Na_{32}H_{22}(OH)_{10}$ | 205 | 123 | 319 |
| $Na_{32}H_{21}(OH)_{11}$ | 221 | 143 | 314 |
| $Na_{32}H_{20}(OH)_{12}$ | 237 | 146 | 307 |
| $Na_{32}H_{19}(OH)_{13}$ | 239 | 152 | 307 |

Table S4. The solution temperatures, decomposition temperatures and enthalpies for the KH/KOH system.

| Material | $T_c$ (°C) | D$H_1$ (J/g) | $T_d$ (°C) |
|---|---|---|---|
| $K_{32}H_{31}OH$ | -168 | 5 | 465 |
| $K_{32}H_{30}(OH)_2$ | -83 | 15 | 473 |
| $K_{32}H_{28}(OH)_4$ | -71 | 26 | 504 |
| $K_{32}H_{27}(OH)_5$ | -51 | 32 | 512 |
| $K_{32}H_{26}(OH)_6$ | -46 | 33 | 518 |
| $K_{32}H_{25}(OH)_7$ | -58 | 33 | 532 |
| $K_{32}H_{24}(OH)_8$ | -39 | 46 | 564 |

Table S4. The solution temperatures, decomposition temperatures and enthalpies for the KH/KOH system (cont.).

| Material | $T_c$ (°C) | D$H_1$ (J/g) | $T_d$ (°C) |
|---|---|---|---|
| $K_{32}H_{23}(OH)_9$ | -21 | 45 | 553 |
| $K_{32}H_{22}(OH)_{10}$ | 16 | 49 | 541 |
| $K_{32}H_{21}(OH)_{11}$ | 16 | 58 | 576 |
| $K_{32}H_{20}(OH)_{12}$ | 61 | 64 | 560 |
| $K_{32}H_{19}(OH)_{15}$ | 56 | 62 | 596 |

Table S5. The solution temperatures, decomposition temperatures and enthalpies for the Rb/RbOH system.

| Material | $T_c$ (°C) | D$H_1$ (J/g) | $T_d$ (°C) |
|---|---|---|---|
| $Rb_{32}H_{31}OH$ | -209 | 1.4 | 361 |
| $Rb_{32}H_{30}(OH)_2$ | -158 | 4.5 | 375 |
| $Rb_{32}H_{29}(OH)_3$ | -140 | 7.1 | 387 |
| $Rb_{32}H_{28}(OH)_4$ | -124 | 9.4 | 397 |
| $Rb_{32}H_{27}(OH)_5$ | -144 | 9.1 | 418 |
| $Rb_{32}H_{24}(OH)_8$ | -176 | 10 | 524 |

**ACKNOWLEDGEMENTS**

The authors gratefully acknowledge support from the U.S. Department of Energy, Basic Energy Science, through Grant DE-FG02-ER46256. T.E.-C. acknowledges partial support from Washington University's Office of Undergraduate Research. We thank David Osborn in the Center for Nanoscience for assistance in collecting the in situ XRD and DSC data. We also thank Bruce Burkeen in the University of Missouri St. Louis Research and Development Tech Shop for his work fabricating experimental equipment.

## REFERENCES

[1] Bogdanović, B.; Schwickardi, M. Ti-doped $NaAlH_4$ as a Hydrogen-Storage Material Preparation by Ti-Catalyzed Hydrogenation of Aluminum Powder in Conjunction with Sodium Hydride. *Appl. Phys. A: Mater. Sci. Process*. **2000**, 72, 221−223.

[2] Michel, K.; Ozolins, V. Native Defect Concentrations in $NaAlH_4$ and $Na_3AlH_6$. *J. Phys. Chem. C* **2011**, *115*, 21443−21453.

[3] Michel, K.; Ozolins, V. Vacancy Diffusion in $NaAlH_4$ and $Na_3AlH_6$. *J. Phys. Chem. C* **2011**, *115*, 21465−21472.

[4] Morioka, H.; Kakizaki, K.; Chung, C.; Yamada, A. Reversible Hydrogen Decomposition of $KAlH_4$. *J. Alloys Compd*. **2003**, *353*, 310−314.

[5] Sorte, E. G.; Majzoub, E. H.; Ellis-Caleo, T.; Hammann, B. A.; Wang, G.; Zhao, D.; Bowman, R. C., Jr.; Conradi, M. S. Effects of NaOH in Solid NaH: Solution/Segregation Phase Transition and Diffusion Acceleration. *J. Phys. Chem. C* **2013**, *117*, 23575−23581.

[6] Mikheeva, V.; Shkrabkina, M. Solid Solutions in NaOH-NaH and KOH-KH Systems. *Russ. J. Inorg. Chem*. **1962**, 7, 1251−1255.

[7] Kresse, G.; Hafner, J. Ab Initio Molecular Dynamics for Liquid Metals. *Phys. Rev. B* **1993**, *47*, 558−561.

[8] Kresse, G.; Furthmüller, J. Efficient Iterative Schemes for ab Initio Total-Energy Calculations Using a Plane-Wave Basis Set. *Phys. Rev. B* **1996**, *54*, 11169−11186.

[9] Perdew, J.; Chevary, J.; Vosko, S.; Jackson, K.; Pederson, M.; Singh, D.; Fiolhais, C. Atoms, Molecules, Solids, and Surfaces: Applications of the Generalized Gradient Approximation for Exchange and Correlation. *Phys. Rev. B* **1992**, *46*, 6671−6687.

[10] Perdew, J.; Chevary, J.; Vosko, S.; Jackson, K.; Pederson, M.; Singh, D.; Fiolhais, C. Erratum: Atoms, Molecules, Solids, and Surfaces: Applications of the Generalized Gradient Approximation for Exchange and Correlation. *Phys. Rev. B* **1993**, *48*, 4978−4978.

[11] Monkhorst, H.; Pack, J. Special Points for Brillouin-Zone Integrations. *Phys. Rev. B* **1976**, *13*, 5188−5192.

[12] Kirkpatrick, S.; Gelatt, C., Jr.; Vecchi, M. Optimization by Simulated Annealing. *Science* **1983**, *220*, 671−680.

[13] Akbarzadeh, A.; Ozolin, V.; Wolverton, C. First-Principles Determination of Multicomponent Hydride Phase Diagrams: Application to the Li-Mg-N-H System. *Adv. Mater.* **2007**, *19*, 3233− 3239.

[14] Giauque, W. The Entropy of Hydrogen and the Third Law of Thermodynamics: The Free Energy and Dissociation of Hydrogen. *J. Am. Chem. Soc*. **1930**, *52*, 4816−4831.

[15] Grindy, S.; Meredig, B.; Kirklin, S.; Saal, J.; Wolverton, C. Approaching Chemical Accuracy with Density Functional Calculations: Diatomic Energy Corrections. *Phys. Rev. B* **2013**, *87*, 075150.

[16] Gurvich, L.; Bergman, G.; Gorokhov, L.; Iorish, V.; Leonidov, V.; Yungman, V. Thermodynamic Properties of Alkali Metal Hydroxides. Part 1. Lithium and Sodium Hydroxides. *J. Phys. Chem. Ref. Data* **1996**, *25*, 1211−1276.

[17] Jensen, F. Locating Transition Structures by Mode Following: A Comparison of Six Methods on the $Ar_8$ Lennard-Jones Potential. *J. Chem. Phys.* **1995**, *102*, 6706−6718.

[18] Kiat, J. M.; Boemare, G.; Rieu, B.; Aymes, D. Structural Evolution of LiOH: Evidence of a Solid−Solid Transformation toward $Li_2O$ Close to the Melting Temperature. *Solid State Commun.* **1998**, *108*, 241−245.

[19] Ren, R.; Ortiz, A. L.; Markmaitree, T.; Osborn, W.; Shaw, L. L. Stability of Lithium Hydride in Argon and Air. *J. Phys. Chem. B* **2006**, *110*, 10567−10575.

[20] Haertling, C.; Hanrahan, R. J., Jr.; Smith, R. A Literature Review of Reactions and Kinetics of Lithium Hydride Hydrolysis. *J. Nucl. Mater*. **2006**, *349*, 195−233.

[21] Haertling, C. L.; Hanrahan, R. J., Jr.; Tesmer, J. R. Hydrolysis Studies of Polycrystalline Lithium Hydride. *J. Phys. Chem. C* **2007**, *111*, 1716−1724.

[22] Sifuentes, A.; Stowe, A. C.; Smyrl, N. Determination of the Role of $Li_2O$ on the Corrosion of Lithium Hydride. *J. Alloys Compd.* **2013**, *580*, S271−S273.

[23] Yu, P.; Chua, Y. S.; Cao, H.; Xiong, Z.; Wu, G.; Chen, P. Hydrogen Storage over Alkali Metal Hydride and Alkali Metal Hydroxide Composites. *J. Energy Chem.* **2014**, *23*, 414−419.

[24] Kittel, C. *Introduction to Solid State Physics*, 5th ed.; John Wiley & Sons, Inc.: New York, **1976**.

[25] Toby, B. H. EXPGUI, a Graphical User Interface for GSAS. *J. Appl. Crystallogr*. **2001**, *34*, 210−213.

[26] Larson, A.; Von Dreele, R. *General Structure Analysis System (GSAS)*; Los Alamos National Laboratory Report LAUR; Los Alamos National Laboratory: Los Alamos, NM, **2004**; pp 86−748.

# SECTION

# 6 CONCLUSIONS

Sodium Alanate is a promising complex metal hydride for hydrogen storage applications. The thermodynamic functions were approximated by DFT. The decompositions of the hydride was then correctly predicted by GCLP. The theory also predicted the mixture of NaOH and $NaAlH_4$ in the high temperature and high pressure environment. A new S105 phase of sodium alanate found by heating sodium alanate under high pressure decomposes at a lower temperature than usual. This indicates that treating $NaAlH_4$ at high temperature and $H_2$ pressure may improve its ability for hydrogen storage, providing a new method of improving its behavior beside catalysts.

The mixture of alkali metal hydrides and metal hydroxides was also investigated theoretically. LiH/LiOH and CsH/CsOH do not mix. Whereas NaH/NaOH, KH/KOH and RbH/RbOH systems are favorable to form solid solutions. The solid solution forms in the case that the effective volume differences of $H^-$ and $OH^-$ are less than 15% in MH/MOH systems. The introduction of $OH^-$ ions destabilizes NaH but stabilizes KH and RbH. The mixture of NaH/NaOH was verified by the NMR narrowing around 150 °C and a reversible DSC thermal anomaly that illustrated that NaOH was mixed with NaH above 150 °C and expelled from NaH below the temperature. DSC results also indicated that there were reversible phase transitions concomitant with the mixing and the high temperature structure is a single face centered cubic phase before melting.

The favorable magnesium transition metal ternary borides were predicted theoretically by DFT. The favorable phases are $MgTMB_4$ for TM = {Mn and Fe} and $Mg_2TMB_6$ for TM = {Fe, Co and Ni} in *Pbam* structures. The structures of the corresponding borohydries were predicted by PEGS, the direct decompositions of which were studied to show appropriate decomposition enthalpy values. The theoretical study provides good prediction results such that the further experimental research should be performed in future to develop the theoretical predictions.

## REFERENCES

[1] Armaroli, N.; Balzani, V. The future of energy supply: challenges and opportunities. *Angewandte Chemie International Edition*. **2007**, *46*(*1-2*), 52-66.

[2] http://www.enercon.com (Accessed 2016 May 13).

[3] http://www.activepower.com (Accessed 2016 May 13).

[4] Investigation on storage technologies for intermittent renewable energies: evaluation and recommended R&D strategy, INVESTIRE-NETWORK (ENK5-CT- 2000-20336), Storage Technology Reports (http://www.itpower.co.uk).

[5] http://www.teslamotors.com (Accessed 2015 February 16).

[6] http://www.hystoretechnologies.com.

[7] Edwards, P. P.; Kuznetsov, V. L.; David, W. I.; Brandon, N. P. Hydrogen and fuel cells: towards a sustainable energy future. *Energy Policy*. **2008**, *36*(*12*), 4356-4362.

[8] http://www.toyota.com/FuelCell (Accessed 2015 February 18).

[9] Sakintuna, B.; Lamari-Darkrim, F.; Hirscher, M. Metal hydride materials for solid hydrogen storage: a review. *International Journal of Hydrogen Energy*. **2007**, *32*(*9*), 1121-1140.

[10] Schlapbach, L.; Züttel, A. Hydrogen-storage materials for mobile applications. *Nature*. **2001**, *414*(*6861*), 353-358.

[11] Momirlan, M.; Veziroglu, T. N. The properties of hydrogen as fuel tomorrow in sustainable energy system for a cleaner planet. *International Journal of Hydrogen Energy*. **2005**, *30*(*7*), 795-802.

[12] Christodoulou C.; Karagiorgis G.; Poullikkas A.; Karagiorgis N.; Hadjiargyriou N. Green electricity production by a grid-connected $H_2$/fuel cell in Cyprus. *Proceedings of the Renewable Energy Sources and Energy Efficiency*. 2007.

[13] Züttel, A.; Borgschulte, A.; Schlapbach, L. (Eds.). (2011). *Hydrogen as a future energy carrier*. John Wiley & Sons.

[14] Elam, C. C.; Padró, C. E. G.; Sandrock, G.; Luzzi, A.; Lindblad, P.; Hagen, E. F. Realizing the hydrogen future: the International Energy Agency's efforts to advance hydrogen energy technologies. *International Journal of Hydrogen Energy*. **2003**, *28*(*6*), 601-607.

[15] Stojić, D. L.; Marčeta, M. P.; Sovilj, S. P.; Miljanić, Š. S. Hydrogen generation from water electrolysis—possibilities of energy saving. *Journal of Powe Sources*. **2003**, *118*(*1*), 315-319.

[16] Zeng, K.; Zhang, D. Recent progress in alkaline water electrolysis for hydrogen production and applications. *Progress in Energy and Combustion Science*. **2010**, *36*(*3*), 307-326.

[17] Ni, M.; Leung, M. K.; Leung, D. Y.; Sumathy, K. A review and recent developments in photocatalytic water-splitting using $TiO_2$ for hydrogen production. *Renewable and Sustainable Energy Reviews*. **2007**, *11(3)*, 401-425.

[18] Fujishima, A.; Honda, K. Electrochemical photolysis of water at a semiconductor electrode. *Nature*. **1972**, *238*, 37-38.

[19] Puga, A. V.; Forneli, A.; García, H.; Corma, A. Hydrogen Production: Production of $H_2$ by Ethanol Photoreforming on $Au/TiO_2$. *Advanced Functional Materials*. **2014**, *24(2)*, 240-240.

[20] Kennedy, J.; Jones, W.; Morgan, D. J.; Bowker, M.; Lu, L.; Kiely, C. J.; Wells, P. P.; Dimitratos, N. Photocatalytic hydrogen production by reforming of methanol using $Au/TiO_2$, $Ag/TiO_2$ and $Au\text{-}Ag/TiO_2$ catalysts. *Catalysis, Structure & Reactivity*. **2015**, *1(1),* 35-43.

[21] Fuel Cell Technologies Office Multi-Year Research, Development and Demonstration Plan, Fuel Cell Technologies Office, Office of Energy Efficiency and Renewable Energy, *U.S. Dept. of Energy* **2012**.

[22] Fichtner, M.; Zhao-Karger, Z.; Hu, J.; Roth, A.; Weidler, P. The kinetic properties of $Mg(BH_4)_2$ infiltrated in activated carbon. *Nanotechnology*. **2009**, *20*(*20*), 204029.

[23] Li, H. W.; Miwa, K.; Ohba, N.; Fujita, T.; Sato, T.; Yan, Y.; Towata, S.; Chen, M. W.; Orimo, S. Formation of an intermediate compound with a $B_{12}H_{12}$ cluster: experimental and theoretical studies on magnesium borohydride $Mg(BH_4)_2$. *Nanotechnology*. **2009**, *20*(*20*), 204013.

[24] Sorte, E. G.; Majzoub, E. H.; Ellis-Caleo, T.; Hammann, B. A.; Wang, G.; Zhao, D.; Bowman, R. C. Jr.; Conradi, M. S. Effects of NaOH in solid NaH: solution/segregation phase transition and diffusion acceleration. *The Journal of Physical Chemistry C.* **2013**, *117(45),* 23575-23581.

[25] Wang, G.; Carr, C. L.; Zhao, D.; Sorte, E. G.; Ellis-Caleo, T.; Conradi, M. S.; Bowman, R. C. Jr.; Majzoub, E. H. Density functional theory of MH-MOH solid solubility (M= alkali) and experiments in NaH-NaOH. *The Journal of Physical Chemistry C.* **2015**, *119*(*15*), 8062-8069.

[26] Delmelle, R.; Gehrig, J. C.; Borgschulte, A.; Züttel, A. Reactivity enhancement of oxide skins in reversible Ti-doped $NaAlH_4$. *AIP Advances.* **2014**, *4(12),* 127130.

[27] Majzoub, E. H.; Herberg, J. L.; Stumpf, R.; Spangler, S.; Maxwell, R. S. XRD and NMR investigation of Ti-compound formation in solution-doping of sodium aluminum hydrides: solubility of Ti in $NaAlH_4$ crystals grown in THF. *Journal of alloys and compounds.* **2005**, *394(1),* 265-270.

[28] Soloveichik G. L. Metal borohydrides as hydrogen storage materials. *Material Matters*. **2007**, *2*(*2*), 11-15.

[29] Dai, B.; Sholl, D. S.; Johnson, J. K. First-principles study of experimental and hypothetical $Mg(BH_4)_2$ crystal structures. *The Journal of Physical Chemistry C*. **2008**, *112*(*11*), 4391-4395.

[30] Li, H. W.; Orimo, S. I.; Nakamori, Y.; Miwa, K.; Ohba, N.; Towata, S.; Züttel, A. Materials designing of metal borohydrides: Viewpoints from thermodynamical stabilities. *Journal of Alloys and Compounds*. **2007**, *446*, 315-318.

[31] Soloveichik, G. L.; Gao, Y.; Job Rijssenbeek, J.; Matthew Andrus, M.; Kniajanski, S.; Bowman, R. C., Jr.; Hwang, S.; Zhao, J. Magnesium borohydride as a hydrogen storage material: Properties and dehydrogenation pathway of unsolvated $Mg(BH_4)_2$. *International Journal of Hydrogen Energy*. **2009**, *34*(*2*), 916–928.

[32] Isobe, S.; Yao, H.; Wang, Y.; Kawasaki, H.; Hashimoto, N.; Ohnuki, S. Study on decomposition process of $NaAlH_4$ by in-situ TEM. *International Journal of Hydrogen Energy*. **2010**, *35*(*14*), 7563-7567.

[33] Majzoub, E. H.; V. Ozoliņs. Prototype electrostatic ground state approach to predicting crystal structures of ionic compounds: application to hydrogen storage materials. *Physical Review B*. **2008**, *77*(*10*), 104115.

[34] Roger L. DeKock; Harry B. Gray; Harry B. Gray (1989). Chemical structure and bonding. University Science Books. p. 199. ISBN 0-935702-61-X.

[35] Payne, M. C.; Teter, M. P.; Allan, D. C.; Arias, T. A.; Joannopoulos, J. D. Iterative minimization techniques for ab initio total-energy calculations: molecular dynamics and conjugate gradients. *Reviews of Modern Physics*. **1992**, *64*(*4*), 1045-1097.

[36] Hohenberg, P.; Kohn, W. Inhomogeneous electron gas. *Physical Review*, **1964**, *136*(*3B*), *B864*-B871.

[37] Kohn, W.; Sham, L. J. Self-consistent equations including exchange and correlation effects. *Physical Review*. **1965**, *140*(*4A*), A1133–A1138.

[38] Martin, R. M. Electronic structure: basic theory and practical methods. Press syndicate of the University of Cambridge, New York, NY, **2004**.

[39] Hamann, D. R. Generalized norm-conserving pseudopotentials. *Physical Review B*. **1989**, *40*(*5*), 2980–2988.

[40] Kresse, G.; Joubert, D. From ultrasoft pseudopotentials to the projector augmented-wave method. *Physical Review B*. **1999**, *59*(*3*), 1758.

[41] Blochl, P. E. Projector augmented-wave method. *Physical Review B*. **1994**, *50*(*24*), 17953–17979.

[42] Blochl, P. E.; Forst, C. J.; Schimpl, J. Projector augmented wave method: ab initio molecular dynamics with full wave functions. *Bulletin of Materials Science*. **2003**, *26*(*1*), 33–41.

[43] Baroni, S.; De Gironcoli, S.; Dal Corso, A.; Giannozzi, P. Phonons and related crystal properties from density-functional perturbation theory. *Reviews of Modern Physics*. **2001**, *73*(*2*), 515-562.

[44] Barreraa, G. D.; Colognesi, D.; Mitchell, P. C. H.; Ramirez-Cuesta, A. J. LDA or GGA? A combined experimental inelastic neutron scattering and ab initio lattice dynamics study of alkali metal hydrides. *Chemical Physics*. **2005**, *317*(*2-3*), 119-129.

[45] Chaudhuri, S.; Graetz, J.; Ignatov, A.; Reilly, J. J.; Muckerman, J. T. Understanding the role of Ti in reversible hydrogen storage as sodium alanate: A combined experimental and density functional theoretical approach. *Journal of The American Chemical Society*. **2006**, *128*(*35*), 11404-11415.

[46] Borgschulte, A.; Züttel, A.; Hug, P.; Barkhordarian, G.; Eigen, N.; Dornheim, M.; Bormann, R.; Ramirez-Cuestad, A. J. Hydrogen–deuterium exchange experiments to probe the decomposition reaction of sodium alanate. *Physical Chemistry Chemical Physics*. **2008**, *10*(*27*), 4045-4055.

[47] Ivancic, T. M.; Hwang, S. J.; Bowman, R. C. Jr.; Birkmire, D. S.; Jensen, C. M.; Udovic, T. J.; Conradi, M. S. Discovery of a new Al species in hydrogen reactions of $NaAlH_4$. *The Journal of Physical Chemistry Letters*. **2010**, *1*(*15*), 2412-2416.

[48] Sorte, E. G.; Bowman, R. C. Jr.; Majzoub, E. H.; Verkuijlen, M. H.; Udovic, T. J.; Conradi, M. S. Mobile species in $NaAlH_4$. *The Journal of Physical Chemistry C*. **2013**, *117*(*16*), 8105-8113.

[49] Kresse, G.; Hafner, J. Ab initio molecular dynamics for liquid metals. *Physcal Review B*. **1993**, *47*(*1*), 558−561.

[50] Kresse, G.; Furthmüller, J. Efficient iterative schemes for ab initio total-energy calculations using a plane-wave basis set. *Physcal Review B*. **1996**, *54*(*16*), 11169−11186.

[51] Perdew, J.; Chevary, J.; Vosko, S.; Jackson, K.; Pederson, M.; Singh, D.; Fiolhais, C. Atoms, molecules, solids, and surfaces: applications of the generalized gradient approximation for exchange and correlation. *Physical Review B*. **1992**, *46*(*11*), 6671−6687.

[52] Perdew, J.; Chevary, J.; Vosko, S.; Jackson, K.; Pederson, M.; Singh, D.; Fiolhais, C. Erratum: atoms, molecules, solids, and surfaces: applications of the generalized gradient approximation for exchange and correlation. *Physical Review B*. **1993**, *48*(*7*), 4978−4978.

[53] Monkhorst, H.; Pack, J. Special Points for Brillouin-Zone Integrations. *Physical Review B*. **1976**, *13*, 5188−5192.

[54] Bogdanović, B.; Brand, R. A.; Marjanović, A.; Schwickardi, M.; Tölle, J. Metal-doped sodium aluminium hydrides as potential new hydrogen storage materials. *Journal of alloys and compounds*. **2000**, *302*(*1*), 36-58.

[55] Ke, X.; Tanaka, I. Decomposition reactions for $NaAlH_4$, $Na_3AlH_6$, and NaH: first-principles study. *Physical Review B*. **2005**, *71*(*2*), 024117.

[56] Bogdanović, B.; Schwickardi, M. Ti-doped $NaAlH_4$ as a Hydrogen-storage material preparation by Ti-catalyzed hydrogenation of aluminum powder in conjunction with sodium hydride. *Applied Physics A*. **2001**, *72*(*2*), 221-223.

[57] Morioka, H.; Kakizaki, K.; Chung, C.; Yamada, A. Reversible hydrogen decomposition of $KAlH_4$. *Journal of alloys and compounds*. **2003**, *353*(*1*), 310-314.

[58] Grindy, S.; Meredig, B.; Kirklin, S.; Saal, J.; Wolverton, C. Approaching chemical accuracy with density functional calculations: diatomic energy corrections. *Physical Review B*. **2013**, *87*(*7*), 075150.

[59] Gurvich, L.; Bergman, G.; Gorokhov, L.; Iorish, V.; Leonidov, V.; Yungman, V. Thermodynamic properties of alkali metal hydroxides. Part 1. Lithium and sodium hydroxides. Journal of Physical and Chemical Reference Data. **1996**, 25(4), 1211−1276.

[60] Jensen, F. Locating transition structures by mode following: a comparison of xix methods on the $Ar_8$ Lennard-Jones potential. *The Journal of chemical physics*. **1995**, *102*(*17*), 6706-6718.

[61] Hanada, N.; Chłopek, K.; Frommen, C.; Lohstroh, W.; Fichtner, M. Thermal decomposition of $Mg(BH_4)_2$ under He flow and $H_2$ pressure. *Journal of Materials Chemistry*. **2008**, *18*(*22*), 2611-2614.

[62] Kumar, N.; Yang, Y.; Noh, W.; Girolami, G. S.; Abelson, J. R. Titanium diboride thin films by low-temperature chemical vapor deposition from the single source precursor $Ti(BH_4)_3$ (1,2-dimethoxyethane). *Chemistry of Materials*. **2007**, *19*(*15*), 3802-3807.

# VITA

Gang Wang was born in December 1983 in Zhengzhou, Henan Province, China. He got his Bachelor of Science degree in Physics in China West Normal University in 2007 in Sichuan Province, China. He took his graduate study in Optics in Fudan University in Shanghai, China and finished up with his Master of Science degree in 2010. Then he joined Dr. Majzoub's research group in 2011. While in the group, he was doing theoretical investigations of new energy source materials funded by Department of Energy (DOE) USA. He got his another Master's degree in Physics in 2013 in University of Missouri – St. Louis. He then continued his research in Dr. Eric Majzoub's group and received his Ph.D. in Physics from Missouri University of Science & Technology and University of Missouri-St. Louis in July 2016.